Spring 5-31-2005

Dynamics of filaments, flares and coronal mass ejections (CMEs)

Ju Jing
New Jersey Institute of Technology

ABSTRACT

DYNAMICS OF FILAMENTS, FLARES AND CORONAL MASS EJECTIONS (CMEs)

by
Ju Jing

The objective of this dissertation is to investigate the connection between the dynamics of solar surface phenomena such as filament eruptions, flares, the coronal mass ejections (CMEs), the core of so-called solar activity, and the properties of the associated magnetic field for the development of forecasts of solar activity and space weather. Both statistical and case studies have been carried out.

The topics covered in this dissertation are: the statistical relationship among phenomena of solar activity, in particular, filament eruptions, flares and coronal mass ejections (CMEs); the correlation between magnetic reconnection rate and flux rope acceleration of two-ribbon flares; the correlation between magnetic twist of linear-force-free active region and solar eruptions; a case analysis of a quiet-sun flare associated with an erupting filament and a fast CME; a case analysis of the periodic motion along a filament initiated by a subflare; and a case analysis of the evolution of the twist of an eruptive filament.

The findings and results confirm some of the theories and conjectures previously proposed and put forth some new insights into the physics of phenomena of solar activity, briefly summarized as follows: (1) a statistical relationship is found among filament eruptions, flares and CMEs; (2) the majority of filament eruptions is found to be associated with new magnetic flux emergence within or adjacent to the eruptive filament; (3) a rapid increase in pitch angle of the twisted structure of an eruptive filament appears to be a trigger of the solar eruption; (4) the hemispheric chirality preferences of quiescent filaments is confirmed; (5) the geoeffectiveness of halo CMEs is found to be associated with the orientation and the chirality of the magnetic fields associated with the eruptions; (6) the temporal correlation between the magnetic reconnection rate and the flare nonthermal

emission is verified; (7) the coronal magnetic reconnection is found to be inhomogeneous along the flare ribbons; (8) a positive and strong correlation is found between magnetic reconnection rate and the acceleration of eruptive filaments which represents the early stages of flux rope eruptions in the low corona; and (9) a special type of periodic mass motion in a filaments is reported that remains a challenge to the classical and recent filament models and may provide information on the existence of the filaments.

DYNAMICS OF FILAMENTS, FLARES AND CORONAL MASS EJECTIONS (CMEs)

by
Ju Jing

A Dissertation
Submitted to the Faculty of
New Jersey Institute of Technology and
Rutgers, the State University of New Jersey - Newark
in Partial Fulfillment of the Requirements for the Degree of
Doctor of Philosophy in Applied Physics

Federated Physics Department

May 2005

APPROVAL PAGE

DYNAMICS OF FILAMENTS, FLARES AND CORONAL MASS EJECTIONS (CMEs)

Ju Jing

Dr. Haimin Wang, Dissertation Advisor — Date
Distinguished Professor of Physics, Associate Director of the Center for Solar-Terrestrial Research and Big Bear Solar Observatory, NJIT

Dr. Phil Goode, Committee Member — Date
Distinguished Professor of Physics, Director of the Center for Solar-Terrestrial Research and Big Bear Solar Observatory, NJIT

Dr. Dale Gary, Committee Member — Date
Professor of Physics, Director of the Solar Array in Owens Valley Radio Observatory, NJIT

Dr. Carsten Denker, Committee Member — Date
Assistant Professor of Physics, NJIT

Dr. Zhen Wu, Committee Member — Date
Associate Professor of Physics, Rutgers University, Newark

BIOGRAPHICAL SKETCH

Author: Ju Jing

Degree: Doctor of Philosophy

Date: May 2005

Undergraduate and Graduate Education:

- Doctor of Philosophy in Applied Physics,
  New Jersey Institute of Technology, Newark, New Jersey, 2005
- Bachelor of Science in Applied Physics,
  Beijing University of Technology, Beijing, China, 1997

Major: Applied Physics

Publications in Refereed Journals:

Jing, Ju; Qiu, Jiong; Lin, Jun; Qu, Ming; Xu, Yan; and Wang, Haimin, 2004, *Magnetic Reconnection Rate and Flux-Rope Acceleration of Two-Ribbon Flares*, Astrophysical Journal, 204, 3903.

Jing, Ju; Vasyl, Yurchyshyn; Yang, Guo; Xu, Yan and Wang, Haimin, 2004, *On the Relation Between Filament Eruptions, Flares and Coronal Mass Ejections*, Astrophysical Journal, 614, 1054.

Jing, Ju; Lee, Jeongwoo; Spirock, Thomas J.; Xu, Yan and Wang, Haimin, 2003, *Periodic Motion Along a Solar Filament Initiated by a Subflare*, Astrophysical Journal, 584L., 103.

Jing, Ju; Lee, Jeongwoo and Wang, Haimin, 2005, *Evolution of Twist of a Eruptive Filament*, Astrophysical Journal, in preparation.

Jing, Ju; Vasyl, Yurchyshyn; Qiu, Jiong and Wang, Haimin, 2005, *On the Relation between Twist Parameter of Active Regions and Properties of Solar Eruptions*, Astrophysical Journal, in preparation.

Wang, Haimin; Qiu, Jiong; Jing, Ju; Spirock, Thomas J.; Yurchyshyn, Vasyl; Ji, Haisheng and Goode, Phil, 2004, *Evidence of Rapid Flux Emergence Associated with the M8.7 Flare on 2002 July 26*, Astrophysical Journal, 605, 931.

Wang, Haimin; Qiu, Jiong; Jing, Ju and Zhang, Hongqi, 2003, *Study of Ribbon Separation of a Flare Associated with a Quiescent Filament Eruption*, Astrophysical Journal, 593L, 564.

Xu, Yan; Cao, Wenda; Liu, Chang; Yang, Guo; Jing, Ju; Denker, Carsten and Wang, Haimin, 2004, *Near-Infrared Observations at 1.56 Microns of the 2003 October 29 X10 White-Light Flare*, Astrophysical Journal, 607L., 131.

Xu, Yan; Yang, Guo; Qiu, Jiong; Spirock, Thomas J.; Jing, Ju; Denker, Carsten and Wang, Haimin, 2004,*Visible and Near-Infrared Contrast of Faculae in Active Region NOAA 8518*, Chinese Journal of Astrophysics, 5, 481.

Qu, Ming; Shih, Frank; Jing, Ju and Wang, Haimin, 2004,*Automatic Solar Flare Tracking Using Image-Processing Techniques*, Solar Physics, 222, 137.

Qu, Ming; Shih, Frank; Jing, Ju and Wang, Haimin, 2003,*Automatic Solar Flare Detection Using MLP, RBF, and SVM*, Solar Physics, 217, 157.

Qu, Ming; Shih, Frank Y.; Jing, Ju; Denker, Carsten and Wang, Haimin, 2005, *Automatic Solar Filament Detection Using Image Processing Techniques*, Solar Physics, submitted.

To
My Family

ACKNOWLEDGMENT

I would like to thank both New Jersey Institute of Technology and Big Bear Solar Observatory for providing resources and financial support for my research assistantship throughout this PhD.

My deepest gratitude goes to my supervisor, Dr. Haimin Wang, who has always been extremely generous with his time, knowledge and ideas and giving me much valuable guidance throughout the PhD. He is an excellent role model both for my educational and personal endeavors. I would thank him for being such a wonderful mentor. It is an honor to have been a student of Dr. Wang.

I thank Dr. Philip R. Goode, Dr. Dale E. Gary, Dr. Carsten Denker and Dr. Wu for their ongoing encouragement, support and advice, for taking the time to read the draft and give feedback on the draft of this dissertation, and for having participated in my dissertation committee.

I am also grateful to many collaborators I've worked with and contributed to various parts of this research, particularly to Dr. Jeongwoo Lee, who encouraged and helped me to publish my first paper in an Astrophysical Journal and gave me many constructive ideas and advice. I am grateful to Dr. Jiong Qiu for all helpful discussions and appreciated guidance she provided in many aspects. Dr. Carsten Denker also gave me a lot of suggestions and help during writing of my second paper. He is always ready to help and is always patient with his students. His lecture about how to plot nice figures using IDL is so impressive. Thanks to Dr. Vasyl Yurchyshyn whose assistance made the extrapolation work much easier. Thanks to Tom Spirock for helping me polish several papers. I do really appreciate the help.

Thanks to all the group members. Also to all my friends and colleagues at NJIT. I thank you all for having made these years enjoyable.

Last, but certainly not the least, I thank my parents, Jing Yinglong and Xu Zhimei,

for being my permanent source of love and strength, and my husband, Qu Ming, for his constant loving support and encouragement, so that I could achieve this degree. Therefore, this work is dedicated to them.

This work is supported by NASA and NSF through a number of grants: NSF grant ATM-0076602, NSF grants ATM-0313591 and ATM-0233931, NASA grants NAG5-12733 and NAG5-13661.

TABLE OF CONTENTS

Chapter **Page**

TABLE OF CONTENTS
(Continued)

TABLE OF CONTENTS
(Continued)

Chapter **Page**

TABLE OF CONTENTS
(Continued)

LIST OF TABLES

LIST OF FIGURES

LIST OF FIGURES
(Continued)

Figure **Page**

LIST OF FIGURES
(Continued)

LIST OF FIGURES
(Continued)

Figure **Page**

LIST OF FIGURES
(Continued)

Figure **Page**

CHAPTER 1

INTRODUCTION

The Sun has been producing radiant and thermal energy for billions of years. The outputs of magnetized plasma and radiation from the Sun are the primary factors affecting the Earth and its nearby space environment. Because of its closeness to the Earth, the Sun serves as a unique laboratory to study the behavior of stars in general. The Sun may look like an unchanging object in the sky, yet with modern observing techniques the Sun reveals the amazing structure that changes dynamically in a rich variety of ways in its surface and atmosphere.

1.1 Overview of Phenomena of Solar Activities

1.1.1 Prominences/Filaments

Filaments and/or prominences are located in the corona but possess temperatures a hundred times lower and densities a hundred or a thousand times greater than coronal values (Priest 1981). Filaments and prominences are identical structures physically, while their dual name just reflects a different observed location (on the disk in absorption or above the limb in emission). They will not be distinguished throughout the dissertation except for a specific purpose. The "filament" is used throughout the rest of the dissertation. Filaments have been classified in two basic types according to their dynamic nature: quiescent filaments and eruptive filaments. Both types of filament are located at boundaries between opposite-polarity, line-of-sight magnetic fields (Babcock & Babcock 1955; Howard 1959; Avignon et al. 1964; Hermans & Martin 1986). Quiescent filaments are long-lived stable structures that can last for several months, while eruptive filaments are usually associated with flares and coronal mass ejections (CMEs). Another distinction is made regarding their locations: active-region filaments form in polarity reversal regions of active region com-

plexes; quiescent filaments are found in quiet sun areas along polarity inversion lines between large-scale areas of opposite polarity; border filaments form on the outside borders of active regions; and polar crown filaments form in the most poleward polarity reversal region. Some physical properties of filaments are given in Table 1.1.

Fine Structure within Filaments

A clear feature of high-resolution observations of quiescent filaments is the presence of fine-scale fibril structures. Because magnetic fields play a decisive role in defining the fine structure and its dynamics, the shape, orientation and possibly the strength of the magnetic field may be inferred from the observed structure (Engvold 2001).

Quiescent filaments often display a well-defined highest, horizontal axis which is called "spine". It is composed of resolvable threads. The "barbs" (legs) connect to the high spine and terminate in the chromosphere. These barbs typically curve downward to the chromosphere and hence have a large vertical component. The fine structure is strikingly dynamic. Doppler measurements in filaments show both upward and downward mass motions which appear to be oscillatory. Such motions, both in the spine and in the vertical bundles of threads in barbs, suggest that the plasma is flowing along the magnetic field lines.

Filament Channel

Observations show that filaments are always formed in so-called filament channels, regions where chromospheric fibrils are aligned with the polarity boundary. Because the fibrils are field-aligned, it is concluded that filaments channels represent the condition of maximum magnetic shear. The importance of the filament channel as a precondition for filament formation has recently been stressed (Gaizauskas 1998). Hα channels are clearest at polarity inversions embedded in strong magnetic fields. However, they are not so much visually in

weak fields. Observations sensitive to coronal emission, such as HeI λ1083 nm, EUV and radio (such as Nobeyama radio heligraph) remain a sensitive indicator of filament channels even when magnetic fields are weak.

Chirality Patterns of Filaments

A handedness property known as "chirality" has been discovered for filaments channels and filaments (Martin et al. 1994). If filaments are viewed from their positive polarity side, two types are found: those that have right-bearing barbs and those with left bearing-barbs. Right-bearing barbs extend from the filament spine to the chromosphere making an angle to the right relative to vertical while left-bearing barbs extend to the left of vertical. It is well established that the magnetic field direction along the axis of a filament with right-bearing barbs is always to the right, or "dextral". Similarly a filament with left bearing barbs has an axial magnetic field direction to the left and is called "sinistral" (Martin et al. 1994). Examples of a sinistral filament (top) and a dextral filament (bottom) are shown in Figure 1.1.

To understand the physical meaning of chirality, Mackay et al. (1997) adopt linear force-free field $\nabla \times \vec{B} = \alpha \vec{B}$ models to study development of a chromospheric filament channel. They showed that the field with positive α will form a channel with sinistral chirality, and field with $\alpha < 0$ will result in a dextral channel. Aulanier & D'emoulin (1998) employed a 2.5-D linear force-free field model to reproduce several important properties of filament observations. Their model also showed that dextral (sinistral) chirality corresponds to the magnetic field with negative (positive) α.

Martin, Bilimoria, & Tracadas (1994) were the first to establish the hemispheric chirality preferences of quiescent filaments. In their data set of 47 quiescent filaments, 72% of filaments in the southern hemisphere had sinistral barb patterns, while all filaments (100%) in the northern hemisphere had dextral barb patterns. Surprisingly, active-region filaments did not show any hemispheric preference in their chirality, despite active-region

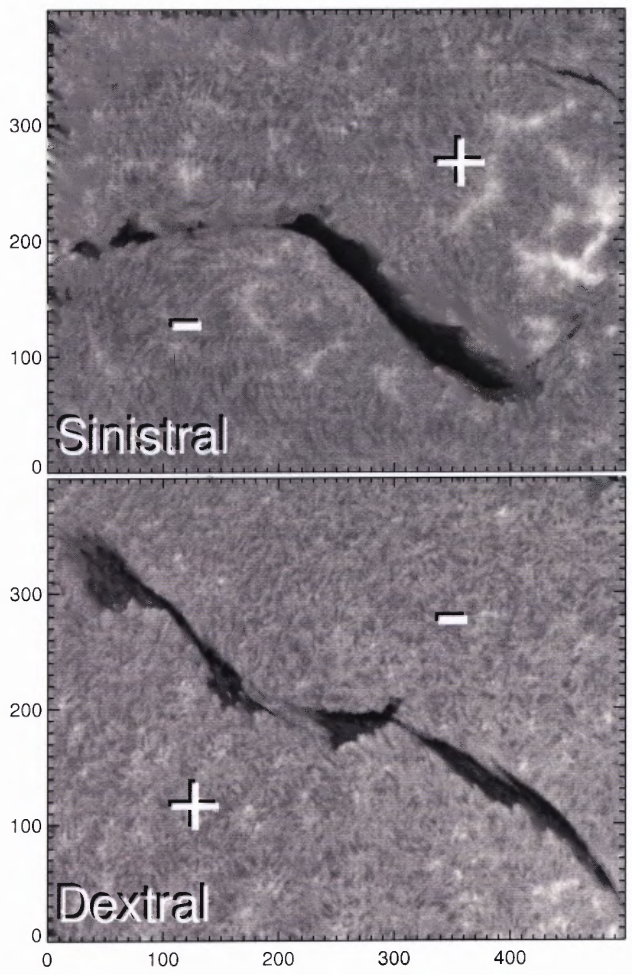

Figure 1.1 A sinistral filament (top) and a dextral filament (bottom). Images are recorded at the Big Bear Solar Observatory.

magnetic fields demonstrating the hemispheric helicity rule (Pevtsov, Canfield, & Metcalf 1995). Furthermore, there appears to be a one-to-one correlation between chirality of the sign of the magnetic helicity (Rust & Martin 1994), i.e., dextral filaments have negative magnetic helicity and sinistral filaments have positive helicity.

A number of models have been developed to explain the chirality of filaments, either based on emergence of subphotospheric twisted fluxtubes (Rust & Kumar 1994), continuous shearing and reconnection (Priest et al. 1996), or based on twisting by meridional flows and other surface motions (Van Ballegooijen et al. 1998). All models also consider the effect of the differential rotation, but none of the models can explain all observed patterns (see review by Zirker 2001).

Filament Oscillations

Solar filaments are continuously subject to oscillations in response to ambient atmosphere perturbations. These vibrations can be either of global nature (for example when a large-scale disturbance, carrying considerable energy, impinges on the broad side of the filament body and shakes its whole structure), or of local nature (when the filament material is perturbed by motions in the solar photosphere, chromosphere or corona; Oliver 2001).

Observations of filament oscillations are compiled in Table 1.2. There are three major groups (see Engvold 2001): short periods with $P \approx 3-5$ min, longer periods with $P \approx 12-20$ min, and very long periods with $P \approx 40-90$ min, which respectively reflect the photospheric p-mode driven domain, the fast magneto-acoustic domain, and the slow magneto-acoustic domain. In general, prominence oscillations have been observed in Doppler shifts (e.g., $v \approx 2-13$ km s^{-1}, Bocchialini et al. 2001) rather than in intensity, as expected for kink-type oscillations, which are non-compressional transverse displacements. However, there is some confusion in the interpretation of Doppler shift measurements, because there are also significant flows present along the filaments (Zirker et al. 1998) besides the kink-type displacement motion. The exciter of a large-scale prominence oscillation is

Table 1.1 Typical physical parameters of filaments inferred from SoHO measurements (Patsourakos & Vial 2002), Hα (Engvold 2001a), and other sources.

Physical parameter	Range of values
Electron density (at $T = 10^5$ K)	$n_e = 1.3 \times 10^9 - 3 \times 10^{11}$ cm^{-3}
Neutral hydrogen column density	$n_H = 10^{16} - 10^{19}$ cm^{-2}
Electron temperature	$T_e = 5000 - 15{,}000$ K
Gas pressure (at $T = 10^5$ K)	$p = 0.03 - 0.38$ dyne cm^{-2}
Length of prominence	$L \approx 60{,}000 - 600{,}000$ km
Height of prominence	$h \approx 10{,}000 - 100{,}000$ km
Width of prominence	$w \approx 4000 - 30{,}000$ km
Number of threads	$N_{thread} = 15 - 20$
Lengths of threads	$L_{thread} = 5000 - 35{,}000$ km
Widths of threads	$d_{thread} = 200 - 400$ km
Filling factor	$q_{fill} = 0.001 - 0.1$
Lifetime of threads	$\tau_{thread} = 1 - 10$ min
Oscillation frequencies	$T = 3 - 5, 6 - 12, > 40$ min
Vertical and horizontal flow velocity (at $T = 10^5$ K)	v$= 2 - 13$ km s^{-1}
Nonthermal velocity (at $T = 10^5$ K)	Δv$= 26$ km s^{-1}
Magnetic field density	$B = 4 - 40$ G

Table 1.2 Periods of prominence oscillations and size scale (adapted from Oliver & Ballester 2002)

Observer	Period $P[min]$	Size $l[Mm]$	Wavelength instrument
Ramsey & Smith (1966)	6–40	...	Hα; Lockheed
Harvey (1969)	1–17	...	Hα; HAO, Climax
Landman et al. (1977)	22	...	Hβ; He^3, Ca^+; Maui
Bashkirtsev et al. (1983)	77, 82	...	Hβ; Sayan
Bashkirtsev & Mashnich (1984)	42–82	...	Hβ; Sayan
Wiehr et al. (1984)	3–5, 50, 60, 64	...	Hα; Locarno
Tsubaki & Takeuchi (1986)	2.7, 3.5	20	Ca II; Hida
Balthasar et al. (1986)	3–6, 48	...	Hα; Locarno
Balthasar et al. (1988)	3–5, 60	...	Hα, Ca^+, Hε; Tenerife
Suematsu et al. (1990)	≈ 60	2.8	Ca II K, Hβ; Hida
Thompson & Schmieder (1991)	4.4	84	Hα; Meudon
Yi, Engvold, & Keil (1991)	5.3, 8.6, 15.8	21	He I; NSO, Sac Peak
	5.3, 7.9, 10.6	7	He I; NSO, Sac Peak
Balthasar et al. (1993)	0.5–20	1–37	Hβ, Ca^+, HeD_3; Tenerife
Balthasar & Wiehr (1994)	5.3–60	1–2	He 3889 A, H8, Ca^+; Tenerife
Sütterlin et al. (1997)	3.5–62	2.1–7.7	Ca^+ 8542; Locarno
Molowny–Horas et al. (1997)	4–12	1.4–7.3	Hβ; Tenerife
Blanco et al. (1999)	1–6	...	O IV, Si IV; SUMER
Régnier et al. (2001)	5, 6–20, 65	...	He I; SUMER
Bocchialini et al. (2001)	6–12	...	O IV, Si IV; SUMER
Terradas et al. (2002)	71	30	Hβ; NSO Sac Peak
Lin (2002)	5–23	...	Hα; NSO

generally a flare (Ramsey & Smith 1966). Spatial observations allow us to distinguish between large-amplitude oscillations, triggered by a wave front from a flare (*winking filaments*), and small-amplitude oscillations that affect only parts (threads) of a prominence. The longest periods seem to involve entire filaments, whereas periods shorter than 20 min appear to be tied to thread-like small-scale structures (Engvold 2001). Recent reviews on oscillations in prominences and filaments can be found in Oliver (2001), Engvold (2001), and Oliver & Ballester (2002).

Formation and Evolution

The observations show that filaments always form in so-called filament channels, i.e., regions where chromospheric fibrils (thread-like fine structures) are aligned with the neutral line. For the question of how prominences acquire their mass there are three different scenarios: (1) cooling and condensation of plasma from the surrounding corona (Pneuman 1972), (2) injection by chromospheric upflows (Pikel'ner 1971), and (3) footpoint heating triggering condensation (Antiochos et al. 2000). Although filaments and prominences appear to be static over longer time intervals, there is a lot of observational evidence that the formation is a continuous process, where mass is continuously entering and exiting the filament magnetic field throughout its lifetime. Moreover, the continuous process of mass transport in filament spines and barbs has been found to consist of bi-directional streams (Zirker et al. 1998).

Disappearance

At some stage a filament may become completely unstable and disappear. The lifetime of a prominence is determined by the balance between heating and cooling. There exist two categories of disappearance: dynamic and thermal (Mouradian et al.1995). The former process consists of an expansion and ejection of filament plasma into the corona due to changes

in underlying magnetic field structure. Generally, the process displays ascending velocities on the order of a few kilometers per second and, through continuous acceleration, reaches a velocity on the order of several hundred kilometers per second. This process ultimately leads to the complete and final disappearance of the filament. In contrast, in the thermal disappearance process the filament is seen to fade slowly while remaining stationary, with the general shape unchanged. The disappearance is due to heating and full ionization, causing it to fade on Hα. The filament will often reappear once it cools down. An excellent example of a flare-triggered thermal disappearance of a filament is recorded at the BBSO in the time interval between 17:59 UT to 19:47 UT on 2001 October 22 and analyzed by Ji et al. (2002). Although the heating mechanism that leads to thermal disappearances of quiescent filament is still not well understood, this simple event shows that the flare triggered some kind of heating mechanism which continued for several hours.

The following precursors of dynamic filament disappearance have been identified: gradual external reconnection (Gary & Moore 2004), a constant gradual acceleration of the filament in height for up to 1 hour before eruption (Kundu et al. 2004), blue-shifted upflows (DesJardins & Canfield 2003), and heating of the filament mass or ejection of heated plasma (Ding et al. 2003).

1.1.2 Flares

The solar flare is a remarkable and beautiful eruptive phenomenon. It varies from being a simple, localized brightening to a bewilderingly complex event. The flare process, driven by stored nonpotential magnetic energy and triggered by an instability of the magnetic configuration, is associated with a rapid energy release in the solar corona. The energy released in a flare varies from 10^{22} J in a subflare to 3×10^{25} J in the largest of events (Priest 1981). Such an energy release process results in acceleration of nonthermal particles and in heating of coronal/chromospheric plasma. These processes emit radiation in almost all wavelengths: radio, white light, EUV, soft X-rays, hard X-rays, and even γ-rays during

large flares.

Flares have been categorized in many different ways, but two particular types, the compact flare and the two-ribbon flare, may be particularly significant. The former is small and simply brightens and fades without moving or changing its shape. It may occur in a large-scale unipolar region or near a simple sunspot. The two-ribbon flare, characterized by two separating bright ribbons, tends to be larger, more energetic, and more likely to be associated with a eruption.

Figure 1.2 is from Xu et al. (2004). It shows the temporal evolution of an X10 white-light two-ribbon flare in solar NOAA Active Region 10486 obtained with the Dunn Solar Telescope (DST) at the National Solar Observatory/Sacramento Peak on 2003 October 29. This is the first report of a white-light flare observed at the opacity minimum.

Magnetic fields are monitored before, during and after the flares. The prelude to a flare, e.g., magnetic shearing and sudden emergence of magnetic flux (Wang et al. 2004b; Moon et al. 2004) have been observed. On the other side, permanent changes of the magnetic field, e.g., rapid penumbral decay (Wang et al 2004a) or the reversal of the magnetic sign (Qiu & Gary 2003), have been observed after a flare. Statistically, it is found that moving blueshifts events, which are indicators of upflows from chromospheric reconnection events, are 5 times more frequent before eruptive flares than in non-eruptive flares (DesJardins & Canfield 2003). After the flare, downflows of $800-1000\ kms^{-1}$ above flare arcades have been observed (Innes et al. 2003), probably direct witnesses of the relaxation of newly-reconnected magnetic field lines (Aschwanden 2004).

1.1.3 CMEs

Coronal mass ejections (CMEs) are huge bubbles of gas threaded with magnetic field lines that are ejected from the Sun over the course of several hours. The phenomenon of a CME occurs with a frequency of about one to three events per day, carrying a mass in the range of $m_{CME} \approx 10^{15} - 10^{16}$ g (Howard et al. 1985; Hundhausen 1999), which corresponds

to an average mass loss rate of $m_{CME}/(\Delta t \cdot 4\pi R_{\odot}^2) \approx 2 \times 10^{-14} - 2 \times 10^{-12}$ g cm^{-2} s^{-1} (Markus 2004). The transverse size of CMEs can cover from a fraction up to more than a solar radius, and the ejection speed is in the range of $v_{CME} \approx 10 - 10^3$ km s^{-1} (Gosling et al. 1976; Howard et al. 1985; St. Cyr et al. 1999, 2000).

The CME-Flare Connection

CMEs are often associated with solar flares and prominence eruptions but they can also occur in the absence of either of these processes. It is expected that the larger the stored energy in the relevant magnetic structure that drives the eruption the better the correlation between the eruptive phenomena and CMEs (Lin 2004). Actually, the fastest and most powerful CMEs are always associated with a particular kind of flare, the two-ribbon flare in Hα in the chormosphere (Zhang & Golub 2003), or the long-duration events of soft X-ray brightening in the corona (Hundhausen 1999). A temporal correlation has been also found between the reconnection rate and the directly observed acceleration of the accompanying CME (Qiu et al.2004). In addition, an empirical relationship has been found between the initial speed of a CME and the potential magnetic field energy of the associated active region, implying that the magnetic energy of the active region drives the CME (Vankatakrishnan & Ravindra 2003).

The Eruptive Filament-CME Connection

In most flare models the eruption of a filament is the first step in a chain reaction that culminates with a CME. However, filament eruptions that are not associated with CMEs are also found. It is known that a filament eruption in an active region is either ejective or confined (Machado et al., 1988; Moore, 1988). Ejective active-region eruptions produce CMEs; confined active-region eruptions do not produce CMEs (Canfield et al., 1999; Falconer et al., 2002). Choudhary and Moore (2003) examined 12 quiescent filament eruptions

(9 were associated with CMEs and 3 were not), and found that, even though the two kinds of eruption were indistinguishable in their magnetic setting and in the eruptive motion of the filament in the Hα movies. Each of the CME-associated eruptions produced a two-ribbon flare in Hα and a coronal arcade in Fe XII while each of the non-CME-associated eruptions did not. From these results, they conclude that quiescent filament eruptions are similar to active-region filament eruptions in having a similar dichotomy of confined and ejective eruptions. This similarity suggests that quiescent filament eruptions, confined or ejective, are unleashed in the same way as active-region filament eruptions.

Geometry of CMEs

Geometric characterizations of CMEs with large statistics have been obtained from *SMM Coronagraph/Polarimeter (C/P)* observations, which include some 1300 CME events in 1980 and during 1984−1989. There is a large range of angular widths, with an average of 47°, launched at an average latitude of 35° (Hundhausen 1993). A typical characteristic of most CMEs is the three-part structure, consisting of (1) a bright leading edge, (2) a dark void, and (3) a bright core (Illing & Hundhausen 1985). It was suggested that CMEs have a loop-like geometry in a 2D plane, based on close associations of CMEs with eruptive prominences and disappearing filaments (Trottet & MacQueen 1980). Alternatively, 3D geometric shpaes were suggested, such as a shape of a bubble, a helical flux rope (Amari et al. 2003; Cheng et al. 2003), a semi-shell (Ciaravella et al. 2003) or a "ice-cone" (Xie et al. 2004). The observations are often sufficiently ambiguous so that these geometries concepts cannot easily be discriminated in the data. While CMEs propagating close to the plane of the sky have a relatively simple projected shape, other CMEs propagating in a direction towards the observer have much more complex shapes, the so-called halo CMEs.

Geometric modelling of CMEs is still in its infancy. Based on the concept of magnetic flux ropes, which consist of helical field lines wound around a curved cylinder, the evolution of a CME is conceived as a steady expansion of this flux rope into interplane-

tary space, with the legs connected to the footpoints on the Sun (Chen 1997a). Figure 1.3 displays the detailed fine structure in a CME, which appears to be composed of numerous helical strands, revealed by edge-enhancing techniques (Wood et al. 1999).

Velocities and Acceleration of CMEs

The height, velocity, and acceleration of a well-defined CME feature, such as the bright leading edge, are observables that can be measured as a function of time relatively easy, in particular for limb events. The time phases of acceleration reveal the height range where accelerating forces operate, and thus might provide crucial insights into the drivers of CMEs. The coronagraphs of the Solar Maximum Mission (SMM) and the Solar and Heliospheric Observatory (SoHO) show that the median CME velocity is about 450 kms^{-1} (Low 2001). Considering the sound speeds $\sim 100 kms^{-1}$ at million-degree temperature and coronal Alfven speeds $\sim 10^3 kms^{-1}$, CMEs tend to be supersonic or sub-Alfvenic in the corona, with implications for the hydromagnetic shocks driven ahead of the CMEs (Sheeley et al. 1985; Hundhausen et al. 1987; De Sterck et al. 1998).

Based on the observed characteristics of CME velocity $v(t)$ and acceleration profiles $a(t)$ observed with *SoHO/LASCO* over the distance range of $r = 2 - 30\ R_\odot$ it was proposed that there exist two distinct classes of CMEs (Sheeley et al. 1999): (1)gradual CMEs, apparently formed when prominences rise up from below coronal streamers, typically attaining slow speeds ($v \approx 400 - 600$ km s^{-1}) with clear signs of gradual acceleration ($a = 3 - 40$ m s^{-2}) at distances $R < 30 R_\odot$; and (2)impulsive CMEs, often associated with flares on the visible disk, with speeds in excess of $v \geq 750 - 1000 kms^{-1}$, observed to have a constant velocity or deceleration at distances $R \geq 2 R_\odot$ when first seen in coronagraphs (Sheeley et al. 1999).

The observations suggest that the acceleration profile $a(t)$ can be approximated by

either an exponentially increasing or decreasing function, (e.g., Sheeley et al. 1999),

$$a(t) = a_0 \exp\left[-(t - t_0)/t_a\right]$$

The velocity profile $v(t)$ follows then from integrating the acceleration profile $a(t)$,

$$v(t) = v_0 + \int_{t_0}^{t} a(t)\, dt$$

and the height-time profile $h(t)$ from double integration of the acceleration profile $a(t)$,

$$h(t) = h_0 + v_0(t - t_0) + \int_{t_0}^{t} \int_{t_0}^{t} a(t)\, dt\, dt$$

The acceleration profile of CMEs cannot be observed at low heights ($R \leq 2R_{\odot}$) with coronagraphs.

Recently, an anti-correlation between the acceleration and velocity has been found: most of CMEs faster than 400 kms^{-1} decelerate (Vrsnak et al. 2004b) whereas slower ones generally accelerate (Vrsnak et al. 2004a). This acceleration-velocity relationship is interpreted as a consequence of the aerodynamic drag (Cargill 2004). Case studies also showed close temporal correlations between the acceleration of the CME and the time derivative of the soft X-ray flux, indicating that the CME acceleration is coupled to the flare particle acceleration (Zhang et al. 2004).

Reviews on CMEs can be found in MacQueen (1980), Howard et al. (1985), Low (1994, 1996, 2001), Hundhausen (1999), Forbes (2000).

1.2 Magnetic Fields

The solar magnetic field controls the dynamics and topology of all eruptive phenomena. The magnetic field on the solar surface is very inhomogeneous. The strongest magnetic field regions are in sunspots, reaching field strengths of $B = 2000 - 3000$ G. Active regions

and their plages comprise a larger area around sunspots, with average photospheric fields of $B \approx 100 - 300$ G, containing small-scale pores with typical fields of $B \approx 1100$ G. The background magnetic field in the quiet Sun and in coronal holes has a net field of $B \approx 0.1 - 0.5$ G. Our knowledge of the solar magnetic field is mainly based on measurements of Zeeman splitting in spectral lines, while the coronal magnetic field is often reconstructed by extrapolation from magnetograms at the lower boundary, using a potential or force-free field model. The extrapolation through the chromosphere and transition region is, however, uncertain due to unknown currents and non-force-free conditions. The fact that coronal loops exhibit generally much less expansion with height than potential-field models underscores the inadequacy of potential-field extrapolations. Direct measurements of the magnetic field in coronal heights are still not available.

1.2.1 Magnetic Flux Emergence

Sunspots and strong flares are believed to be associated with the emergence of magnetic flux through the photosphere. During emergence, magnetic dipoles grow in size and their rate of divergence is of order $v \approx 2.3$ km s^{-1}, while magnetic flux increases with a rate of $d\Phi/dt \approx 1.6 \times 10^{15}$ Mx s^{-1} (Hagenaar 2001). The emergence of growing new magnetic flux structures necessarily forces topological changes in the magnetic field of the overlying corona, which may involve magnetic reconnection processes. If the emerging field has the same orientation as the overlying coronal field, an approximately current-free field forms in the interaction region. If the emerging field is anti-parallel, however, a current sheet forms which could initiate magnetic reconnection (Shibata et al.1989). Feynman & Martin (1995) found statistically that two thirds of the quiescent-filament-associated CMEs occurred after substantial amounts of new magnetic flux emerged in the vicinity of the filament. In addition, 17 of the 22 filaments that were associated with new flux emergence erupted, and 26 of 31 filaments that were not associated with new flux did not erupt. Although it is not sure whether the magnetic flux emergence does necessarily trigger

flares or filament eruptions directly, it does increase the magnetic complexity locally, which ultimately may escalate into a eruptive event. An example of flux emergence associated with a eruptive filament is given in Figure 1.4.

1.2.2 Magnetic Flux Cancellation

The reverse process of magnetic flux emergence is magnetic flux cancellation, i.e., when opposite polarities of magnetic field converge and meet, the magnetic field of those magnetic flux patches begins to disappear (Matin et al. 1985). Magnetic cancellation is found along the polarity inversion of all filaments from the smallest to the largest (Martin 1990) and may be the most direct form of energy dissipation. There is considerable theoretical and observational evidence that chromospheric reconnection with magnetic flux cancellation is a likely mechanism to explain chromospheric variability, e.g, flares (Livi et al. 1989), Hα upflows (Chae et al.2003), spicules and short-lived brightenings observed in Hα (Qiu. et al. 2000), and soft X-ray (Harvey 1996).

1.2.3 Magnetic Helicity

Magnetic helicity is a measure of the topological structure of the magnetic field, particularly suited to characterize helically twisted, sheared, linked, and braided field lines. The concept of magnetic helicity became a focus recently for the following reasons:

1. Helicity conservation: A helicity conservation law has been derived by Woltjer (1958) under the assumptions of linear force-free field (with constant parameter α). A more formal derivation can be seen in Sturrock (1994) or in Bellan (2002). The conservation of helicity is an important invariant during the evolution of coronal structures, which can be applied to active region loops (e.g., Liu et al. 2002; Kusano et al. 2002), flare loops (e.g., Pevtsov et al. 1996; Moon et al. 2002b), filaments (e.g., Chae 2000; Pevtsov 2002), prominences (e.g., Shrivastava & Ambastha 1998; DeVore & Antio-

chos 2000), magnetic fluxropes and interplanetary magnetic clouds (e.g., Kumar & Rust 1996; Cid et al. 2001), etc.

2. Helicity and reconnection: Although helicity may be conserved on a global scale, it may be redistributed locally through magnetic reconnection. Such redistribution of helicity may play a significant role in the buildup of twist, and therefore the stability of magnetic fields, e.g., reconnection of a highly twisted small scale loop and a weakly twisted large loop may result in injection of twist into the larger structure. As a consequence, the larger loop may became unstable and erupt (Rust 1994; Pevtsov et al. 1996). It has been discovered that reconnection occurs preferentially between active regions with the same sign of helicity at the photosphere (Canfield et al. 1996).

3. Helicity continuity: The signature of magnetic helicity has been observed in the solar photosphere, chromosphere, corona, solar wind and interplanetary magnetic field (Seehafer 1990; Rust 1994; Bieber & Rust 1995). The same hemispheric sign rule has been found for all these different data. The origin of the helicity of coronal and interplanetary fields is important for space weather forecasting. The geo-effectiveness of magnetic clouds depends on the orientation of their magnetic field, including their magnetic helicity. Knowledge of the magnetic helicity of a potentially geo-effective event at the Sun may prove useful in predicting its impact on the magnetosphere. Moreover, establishing magnetic helicity continuity between photospheric fields and interplanetary magnetic fields will help in the prediction of such events days before their arrival to Earth.

1.3 Theories and Models of Solar Eruptions

1.3.1 The Standard 2D Models

The most widely accepted standard model for flares is the 2D magnetic reconnection model that developed by Kopp & Pneuman (1976). The initial driver of the flare process is a

rising filament above the neutral line. Flare loops and ribbons could be understood as an manifestation of the magnetic field lines stretched by the ejection of plasma. When the plasma at the top of the loop is ejected, the magnetic field lines become highly extended that was called "open", and then relax to form closed loops through a process known as magnetic reconnection. The X-type reconnection region is assumed to be the location of major magnetic energy dissipation, which heats the local coronal plasma and accelerates thermal and nonthermal particles.

A prediction of the Kopp−Pneuman (1976) model is that the X-point progressively rises with time, which implies that newly reconnected field lines should show a progressively larger apex height and an increasing footpoint separation with time. Many observations in Hα, EUV and soft X-rays show that the ribbons essentially lie at the footpoints of the loop system. Sakao et al. (1998) measured footpoint motion and found that about half of the flares show an increasing footpoint separation with a nonthermal hard X-ray spectrum, which he interpreted in terms of the Kopp−Pneuman scenario, while the other half exhibited a footpoint separation decrease as well as a hard X-ray spectrum with large photon index, which he interpreted in terms of the emerging flux model (Sakao et al. 1998). During the Bastille-Day flare 2000-Jul-14, a systematic increase of the separation of the flare ribbons was clearly observed in EUV as well as in hard X-rays (Fletcher & Hudson 2001). A somewhat more complicated motion was observed in Hα footpoint kernels, but with an overall trend of increasing footpoint separation (Qiu et al. 2002).

However, an important constraint, referred to as Aly-Sturrock constraint, was found by Aly (1991) and Sturrock (1991). They numerically studied a process during which a closed force-free arcade system transited to a completely open field and found that a completely open field could contain more magnetic energy than a completely closed field. Therefore, the transition from a closed configuration to an open field configuration would appear to be energetically impossible.

There are several ways to bypass the Aly-Sturrock constraint, for example, a non-

force-free initial state, or an ideal magnetohydrodynamic (MHD) eruption that only partially opens the closed magnetic field lines, or a non-ideal MHD process, especially magnetic reconnection might make a difference(see Lin 2002).

1.3.2 The Emerging Flux Model

One of the most commonly accepted solar eruption models now assume that the continual emergence of new flux from the convection zone and the footpoints of closed coronal field lines causes stresses to build up and accumulate energy in the coronal magnetic field (Heyvaerts et al. 1977). Eventually, the configuration may become unstable when the stress exceeds a threshold beyond which an equilibrium can no longer be maintained. As a result, the coronal magnetic field erupts and most of the stored energy is released via magnetic reconnection.

In this model, there are three phases: (1) a preflare heating phase where a new magnetic flux emerges beneath the flare filament and continuously reconnects and heats the current sheet between the old and new flux; (2) the impulsive phase starts when the heated current sheet loses equilibrium at a critical height and turbulent electrical resistivity causes the current sheet rapidly to expand, accelerating particles and triggering chromospheric evaporation; and (3) the main phase where the current sheet reaches a new steady state with reconnection. A requirement of this model is the pre-existence of a stable current sheet (with very low resistivity) for periods of the order of a day or more. However, numerical simulations indicate the current sheets reconnect almost as quickly as they are formed (Forbes & Priest 1984; Shibata et al. 1990). It is therefore believed that the this model can only apply to small flares (Priest & Forbes 2000).

1.3.3 Break-out Model

In this model, the magnetic field configuration has a spherically symmetric quadrupolar geometry rather than a dipolar geometry. A current is created by shearing the arcade straddling the equator and magnetic reconnection occur on top of the sheared arcade. Reconnection removes the unsheared field above the low-lying, sheared core flux near the neutral line, which then allows the field above the core flux to open up (Antiochos et al.1999). Thus, this model addresses the energy problem: How very low-lying magnetic field lines can open up (down to the photospheric level) into an open-field configuration during the eruption. Moreover, the eruption is solely driven by free magnetic energy stored in a closed, sheared arcade. It circumvents the Aly−Sturrock energy limit by allowing external, disconnected magnetic flux from a neighboring sheared arcade (which is not accounted for in the "closed-topology" model of Aly and Sturrock) to assist in the opening-up process. Thus, a key point of the magnetic breakout model is the interaction of a multi-flux system (e.g., in a quadrupolar double arcade).

1.3.4 Flux-rope Catastrophic Model

This model demonstrates how the (force-free) evolution passes a critical point where the system becomes unstable and triggers the rise of a filament, and has been developed by Forbes & Priest (1995) in 2D. In this model, to support the filament and drive its eruption, the flux-rope must carry a current. The background field is similar to that produced by a biopolar arcade embedded in the photosphere. The mass flow in the photoshphere brings the magnetic field from a distance to the origin, forces the magnetic field lines in opposite direction to reconnect at the origin. The initial situation of the magnetic field is shown in Fig. 1.5 (b). The two footpoints of the field lines that envelop the flux rope are then driven closer together, while the system evolves through a series of equilibrium solutions. The height h of the flux rope as a function of the separation half-distance λ is shown in

Fig. 1.5(a). Once the source separation passes the critical point at $\lambda = 1$, the flux rope enters a loss of equilibrium and jumps in height (from $h = 1$ to $h \approx 5$), while forming a current sheet beneath [Fig. 1.5(d)]. In ideal MHD, the rising flux rope would stop at a higher equilibrium position, because the tension force associated with the current sheet is always strong enough to prevent the fluxrope from escaping (Lin & Forbes 2000). If there is some resistivity, magnetic reconnection is enabled, and even a fairly small reconnection rate is sufficient to allow the flux rope to escape (Lin & Forbes 2000). This model is formulated fully analytically and yields reasonable amounts of released energies, suitable to explain flares and CMEs. Although this analytical model is restricted to 2D (with a fluxrope that is not anchored at both ends), it demonstrates quantitatively how a loss of magnetic equilibrium leads to a rapid energy release, which probably also takes place in more complex 3D configurations.

1.4 Space Weather Forecasting

Solar activity is closely related to the near earth environment - summarized descriptively as space weather. The solar wind carries the magnetic field of the Sun. This magnetic field or the IMF (interplanetary magnetic field) has a particular orientation - southward or northward. It has been found in numerous studies that changes in the strength and direction of the IMF near the Earth's orbit are important factors in causing the geomagnetic activity that can greatly perturb the magnetosphere and ionosphere. The coupled solar wind – magnetosphere – ionosphere system is most highly energized when the IMF turns south, i.e., anti-parallel to the direction of the Earth's magnetic field. In other words, southward IMF causes magnetic reconnection, rapidly injecting magnetic and particle energy into the Earth's magnetosphere and modifying the large-scale ring current systems, and therefore, geomagnetic storms can be expected.

Geomagnetic storms can cause a variety of undesirable consequences, for example, electrical current surges in power lines, interference in the broadcast of radio, television,

and telephone signals, and problems with defense communications. One of the most dramatic effects on ground systems during geomagnetic storms is the disruption of power systems. The enhanced particle density within the Earth magnetic fields during a geomagnetic storm can also cause damage to satellites. Under some conditions, solar eruptions can also accelerate charged particles to very high energies (protons and heavier particles, such as helium). These highly energetic particles can penetrate into electronic components, causing bit-flips in a chain of electronic signals that may result in spurious commands. In addition one can experience erroneous data from the onboard instruments. These spurious commands have caused major failures to satellite systems, even causing the craft to point away from the earth direction. Energetic solar protons are also a radiation health hazard for astronauts on manned space flights, in particular for long space missions outside the Earth protective magnetosphere.

Therefore forecasting of major activity and geo-magnetic is vitally important. The presence of two satellites, *Solar and Heliospheric Observatory*(SOHO) and *Advanced Composition Explorer*(ACE), has definitely improved the accuracy of space weather forecasts. Two instruments on board SOHO have proved to be especially valuable for continuous real-time monitoring of solar storms that affect space weather. One is the *Large Angle Spectrometric Coronagraph* (LASCO) that takes images of the solar corona by blocking the light coming directly from the Sun itself with an occult disk, creating an artificial eclipse within the instrument. The other is the *Extreme ultraviolet Imaging Telescope* (EIT), providing images of the solar atmosphere at four wavelengths. It reveals flares and other stormy events in the atmosphere, and can usually determine whether CMEs seen by LASCO originated on the near or far side of the Sun, based on the presence or absence of corresponding events on the near side.

Real-time, high-quality data and data processing would be a key element to forecast space weather promptly and accurately. A innovative computation and information technologies (ITR) for real time space weather monitoring and forecasting is being established

at BBSO.

There are three goals in the ITR project.

1. Combine state-of-art parallel computing techniques with phase diversity speckle imaging techniques, to yield near real-time diffraction limited images with a cadence of approximately 10 seconds.

2. Use the technologies of image processing and pattern recognition, such as Support Vector Machines (SVMs), Neural Networks (NNs) and Image Segmentation to detect and characterize three important solar activities in real-time: filament eruptions, flares, and CMEs.

3. Develop web based software tools to post processed data, events and forecasting in real time, and to be integrated with current solar activity and space weather prediction web pages at Big Bear Solar Observatory (BBSO).

1.5 The Scientific Goals and the Structure of the Dissertation

As mentioned, filament eruptions, flares and coronal mass ejections (CMEs) are the most important solar events as far as space weather effects are concerned. Because the solar magnetic field are the ultimate causes of these solar activities, a deep understanding of the properties and behavior of the solar magnetic field is also required. Therefore, comprehensive study of the solar activities and the solar magnetic field is essential to space weather program. Our goal is to explore the connection between solar surface phenomena such as filament eruptions, two-ribbon flares, the CMEs' occurrence, and the properties of the associated magnetic field, e.g., magnetic reconnection rate, magnetic twist and helicity. Both statistical and case studies have been carried out.

As a way of providing the context of the work, the dissertation is organized according to the individual specific topic. Accordingly, the dissertation has seven Chapters as follows:

Chapter 1: *Introduction.*

It is a introductory chapter involving overview of phenomena of solar activities(section 1.1), magnetic field(section 1.2), theories and models of solar eruptions(section 1.3),and space weather forecasting(section 1.4). Most of these topics are relevant to the detailed studies presented in following chapters.

Chapter 2: *Relationship Among Phenomena of Solar Activity.*

In this chapter, a statistical study is presented on the relationship between filament eruptions, flares and CMEs using 5 yr data. The main results have been published in *Astrophysical Journal, 2004, v. 614, p. 1054.*

Chapter 3: *Magnetic Reconnection Rate and Flux-Rope Acceleration.*

In this chapter, a positive and strong correlation is found between the magnetic reconnection rate and the acceleration of erupting filaments that represents the early stages of flux-rope eruptions in the low corona. The main results have been published in *Astrophysical Journal, 2004, v. 620, p. 1085.*

Chapter 4: *Magnetic Reconnection Rate of a Two-ribbon Flare.*

In this chapter, a detailed case study of a two-ribbon flare and its associated filament eruption and CME observed on 2000 September 12 is presented. The main results have been published in *Astrophysical Journal, 2004, v. 593, p. 564.*

Chapter 5: *Periodic Motion Along a Solar Filament.*

In this chapter, a periodic mass motion in solar filaments, not previously reported, is studied with high cadence Hα observations made at the Big Bear Solar Observatory (BBSO). Various possibilities for explaining this mass motion are discussed to find a remarkable similarity between the observations and the theories. The main results have been

published in *Astrophysical Journal Letter, 2003, v. 584L., p. 103.*

Chapter 6: *Evolution of the Twist of a Eruptive Filament.*

In this chapter a case study of the evolution the twist in a eruptive filament is reported. The primary observations are from Kanzelhohe Solar Observatory (KSO). Hα images of the filament reveal apparent twisted structure which correlates well with the twisted flux rope model (Chen 1996).

Chapter 7: *Twist Parameter of Active Regions and Solar Eruptions.*

This chapter is targeted at investigating the statistical correlation between the magnetic twist and some properties of solar eruptions (e.g., acceleration of eruptive filament, magnetic reconnection rate of corresponding two-ribbon flares).

Chapter 7: *Summary.*

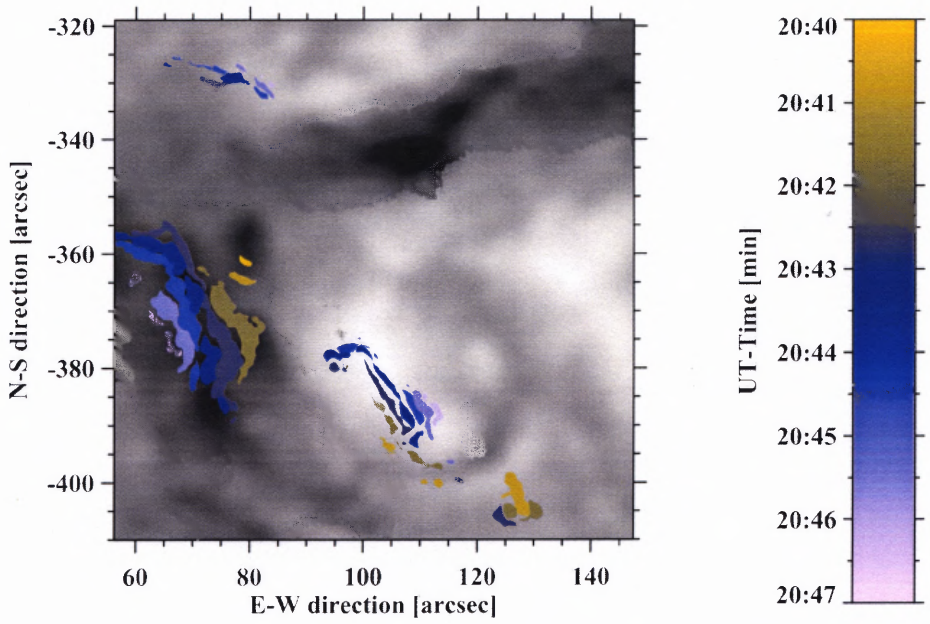

Figure 1.2 Color-encoded near-infrared (NIR) difference images showing the temporal evolution of the flare ribbons from 20:40 to 20:47 UT. The background is an MDI line-of-sight magnetogram. Figure is from Xu et al. 2004.

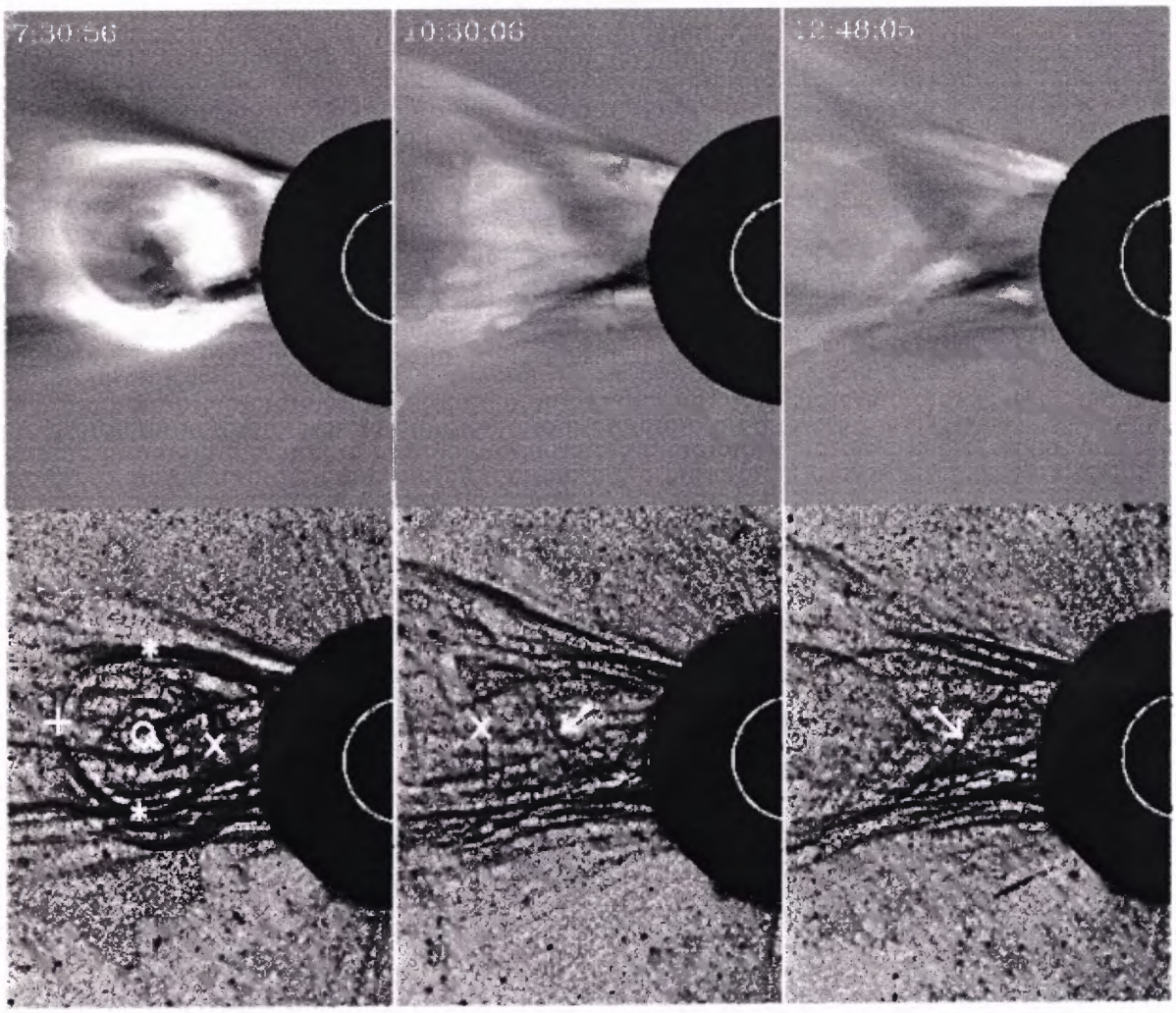

Figure 1.3 LASCO C2 images of the CME of 1997-Apr-30, processed by average difference (top row) and edge-enhancing (bottom row). The leading edge is marked +, the trailing edge X, the sides *, and the centroid O. Helical lines (marked with arrows) are seen below the rim that possibly trace the magnetic field (Figure from Wood et al. 1999).

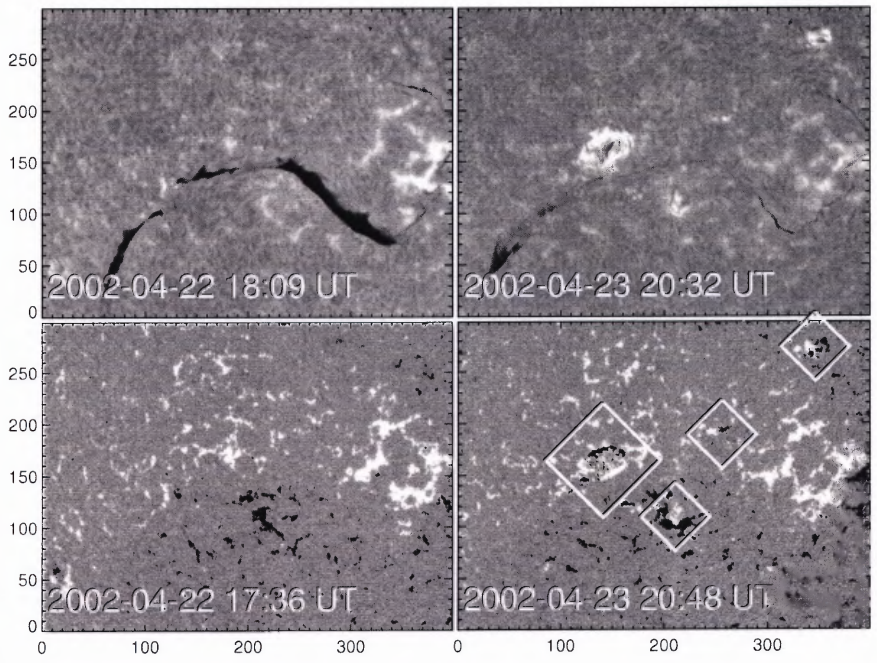

Figure 1.4 The new magnetic flux, as indicated by the square boxes, emerge on 2002 April 23 alongside an eruptive filament. The top two panels are Hα images obtained at BBSO. The bottom two panels are MDI magnetograms.

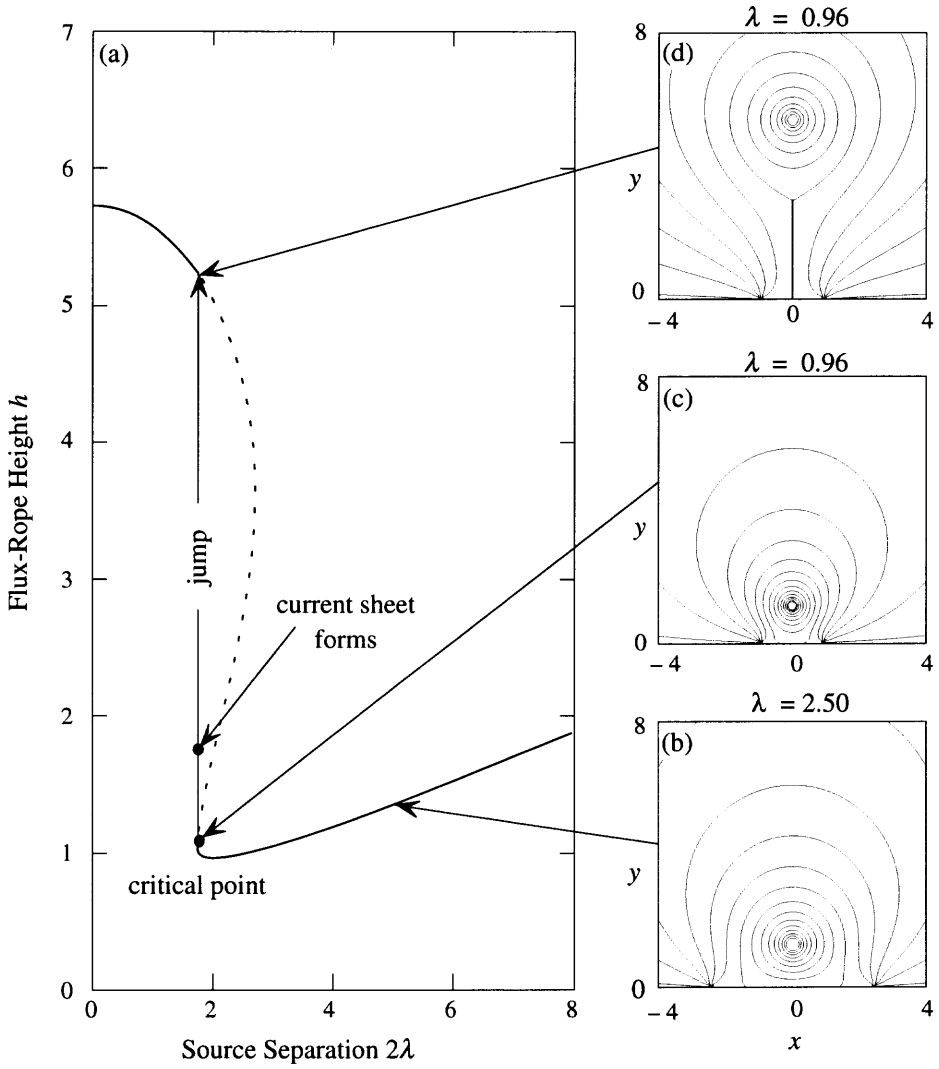

Figure 1.5 Flare dynamics in the model of Forbes & Priest (1995), inferred from the ideal MHD evolution of a 2D arcade containing an unshielded fluxrope (a)–(c). The fluxrope arcade jumps upwards when the two photospheric field sources are pushed too close to one another. (d) The vertical current sheet is subject to magnetic reconnection if enhanced or anomalous resistivity occurs (Figure from Forbes & Priest 1995).

CHAPTER 2

RELATIONSHIP AMONG PHENOMENA OF SOLAR ACTIVITY

2.1 Introduction

Filament eruptions, flares, and CMEs are the most important solar events as far as space weather effects are concerned linking solar eruptions, major interplanetary disturbances and geomagnetic storms (Gosling et al. 1991). A halo CME, which is usually associated with activity near solar disk center, has great influence on space weather because an Earthward halo CME is indicative of coronal mass and magnetic fields are moving out toward the Earth and therefore, is likely to cause geoeffective disturbances (Cane et al. 2000; Webb et al. 2000). The sign of magnetic helicity in active regions can be used to predict the orientation of the magnetic field associated with a CME and furthermore, the probability of a geomagnetic storm (Yurchyshyn et al. 2000).

In order to gain a better understanding of CMEs and to improve the reliability of geomagnetic storm predictions and warnings, it is essential to observe early manifestations of CMEs in the solar atmosphere. Thus, our goal is to find possible relationships between solar surface phenomena such as filament eruptions and flares, the CMEs occurrence, and the properties of the associated magnetic field. Once a relationship is found, it can serve as an indicator for the occurrence of geomagnetic storms.

Filaments and prominences refer to the same physical structures on the Sun, either projected onto the disk or extending above the limb. The majority of previous statistical studies regarding the connection between filament (or prominence) eruptions and CMEs have focused on prominences because they could easily be detected, observed, and measured against the dark sky background. Moreover, CMEs, associated with the prominences, are not difficult to detect. Many prominence classifications have been proposed in the past. For example, Gilbert et al. (2000) developed definitions of active prominences (APs) and

eruptive prominences (EPs) and studied the relationship between APs, EPs, and CMEs for 54 events. They found that 94% of the EPs had an associated CME compared to only 46% for APs. (Gopalswamy et al. 2003) defined a prominence as a radial or a transverse event. Authors showed that the radial events have a strong correlation to the CMEs: 83% of the radial events were associated with CMEs compared to 24% for transverse events. However, (Yang & Wang 2002) showed that the connection between filament disappearances observed in Hα spectral line and CMEs is weak ranging from 10% to 30%.

Filament disappearance does not always imply filament eruptions. Depending on their physical nature, disappearing filaments can reappear. Two processes have been proposed by Mouradian et al. (1995): dynamic sudden disappearance (DSD) and thermal disappearance (THD). DSD is due to restructuring of the magnetic field and it ultimately leads to the disappearance of the filament through an eruption process, whereas THD is due to heating of the plasma in the filament, which will reappear once it cools down. Since THD is not related to magnetic field reorganization, it is excluded from this study.

A "filament eruption" is defined as a solar activity event with significant upward motion and with at least 50% of the material vanishing during the course of a day. In this sense, filament eruptions and the aforementioned DSDs, EPs, and radial events are really all the same manifestations, but with slightly different definitions. It should also note that this study includes both filament eruptions observed close to the solar limb with a normalized distance from solar disk center larger than $0.6R_{\odot}$ and earth-directed filament eruptions observed on the disk. Since the THD events have been eliminated from the study, terms "disappearance" and "eruption" are used synonymously throughout the rest of the chapter. Two BBSO Hα full disk images, about 24 hours apart, allows us to identify filament disappearance on the disk. Then high cadence data of Hα and the Extra-Ultraviolet Imaging Telescope (EIT) onboard the Solar and Heliospheric Observatory (SoHO) is used to confirm these events are indeed erupting, even though their signatures in EIT images are more difficult to identify. A filament was considered as erupting, if it displays ascending

motion, in contrast to filaments that fade away as a whole, while their general shape remains the same. The latter type of disappearing filaments has been discarded from our study. Usually, ascending motion of filaments is determined by the line-of-sight velocity derived from Doppler measurements. Unfortunately, such data are not available. The evolution of the geometrical shape of the filament, for example whether it shows a loop like eruption, provides us the clue to determine whether it is actually erupting.

In this chapter, a comprehensive five-year study of filament eruptions from 1999 January 1 to 2003 December 31 is presented. The study includes both close-to-limb events ($R > 0.6R_{\odot}$) and earth directed disk events. The data sets are described in Section 2, the methods are outlined in Section 3, the statistical results are listed in Section 4, and finally, the observational results are discussed and summarized in Section 5 and 6.

2.2 Data Sets

BBSO Hα full disk images are used as the primary data set to detect the filament eruptions. During the last few years, BBSO has developed a new generation of well calibrated, photometric Hα full disk observations (Denker et al. 1999; Steinegger et al. 2000), which include limb darkening correction to enhance features on the disk as well as above the limb. The Hα full disk data were acquired with a large-format, 2k $\times$ 2k pixels, 14-bit Apogee KX4 CCD camera. The time cadence is one image frame per minute during the entire observing day and the image scale is approximately $1''$ pixel^{-1}.

In addition to the Hα observations, MDI magnetograms (Scherrer et al. 1995), EIT images (Delaboudiniere et al. 1995), LASCO C2 coronagraphs (Brueckner et al. 1995), GOES soft X-ray light-curves, and SGD solar event reports were examined to identify the related phenomena of solar activity such as new flux emergence, flares, and CMEs.

2.3 Methods

Unlike in some previous studies, which used CMEs as the starting point and traced them back to their origin on the solar surface (Webb et al. 1987; Webb et al. 2000), this study started from identifying a filament disappearance, eliminating those events that are not indeed erupting, and then evaluated GOES soft X-ray light-curves, SGD solar event reports, MDI magnetograms, and LASCO data to establish a relationship between the filament eruption and other phenomena of solar activity.

2.3.1 Data Selection

A total of 3,620 filament disappearance events were detected by an automatic detection program from 1999 January 1 to 2003 December 31, which uses IDL code in Linux system and generated a "filament disappearance report"every day (Gao et al. 2002). The program selects one Hα snapshot each day and compares it with another image from the previous day in order to detect disappearing filaments. To simplify the data selection, I first selected 243 filament disappearances, with a surface area of at least 2,000 arc sec^2. In order to be included in our study list, observations, with the cadence of one image frame per minute, have to be available during the entire progress of the filament disappearance. In the case there was a data gap in the BBSO Hα full disk image sequence, Hα full disk images obtained at the Kanzelhöhe Solar Observatory (KSO) in Austria and EIT images which have a relatively lower temporal cadence, 12 minute, are resorted. During this process of selection, it was able to exclude some misidentifications made by the program, events which had not been satisfactorily observed as well as some filament disappearances which could not unambiguously be classified as filament eruptions. Since active region filaments appear to be thinner in depth and width compared to quiescent filaments, 22 small events ($< 2,000$ arc sec^2), most of them were in active regions, were included in our study as supplementary of filament eruptions in active regions. The final sample of filament eruptions included in

this study was 106: 43 of them with complete Hα coverage, while the rest of events were observed from the beginning to the end in EIT images.

2.3.2 Event Classification

1. *Flares:* Flares (optical and X-ray flares) were identified first as sudden brightenings in Hα (flare ribbons) or EIT (flare loops) observations. In other words, flare association is determined directly from the observation. Then GOES soft X-ray flux profiles and SGD solar event reports, within a time period of 1 hour around the observed onset time of flares, are examined for X-ray class, onset time and location.

2. *New Flux Emergence:* new flux emergences is determined from a time sequences of MDI magnetograms with $790'' \times 590''$ field-of-view (FOV) obtained at least 12 hours prior to the eruption. The FOV was centered on the eruptive filament to located the magnetic field in the "vicinity of the filament" (see Feynman & Martin 1995, for the definition of the "vicinity of the filament").

3. *CME:* I used LASCO C2 coronagraph images and the CME catalogue (Gopalswamy et al. 2003) to determine, whether there was a CME associated with the filament eruption. I require that the latitude of the CME is within $\pm 30^{\circ}$ of the latitude of the eruptive filament and that the CME appears in LASCO C2 coronagraph images within two hours after the eruption of the filament. I chose this particular time delay, because it takes approximately two hours for a CME travelling at a relatively low plane-of-sky speed of 200 km/s to cover a distance of two solar radii, i.e., to reach the LASCO C2 FOV. Taking into account the projection effect and the acceleration time of a CME, this two-hour time window seemed reasonable. For events, which originate near disk center and are likely to result in halo or partial halo CMEs, the above requirements have to be relaxed.

2.4 Results of Filament Eruption Associations

Table 2.1 presents a list of 106 filament eruptions and summarizes their relation to emerging flux regions, flares, and CMEs. The 1st and 2nd column of the table contain date and time of the filament eruptions. Subsequent columns provide observed properties of the filament eruptions (position, size, chirality) and relate them to occurrences of EFRs, flares, and CMEs. In the following enumeration, I explain some of the terms used in Table 2.1.

Table 2.1 Properties of Filament Eruptions and their Associated Solar Activity

	Filaments					EFRs	Flares			CMEs		
Date	Eruption Time [UT]	Position	Size [arc sec^2]	Type	Chirality	EFR[a]	Class	Time[b] [UT]	Location	Time[c] [UT]	Central PA[d] [deg]	AW[e] [deg]
1999/01/17	17:32 – 20:21	N38E16	2612	AR8440	···	no data	C2.5	18:29	N18E19	···	···	···
1999/03/10	02:00 – 03:00	S40W16	12080	QS	dextral	yes	···	···	···	03:26	176	76
1999/03/20	21:12 – 23:24	N23W07	4260	QS	···	no	···	···	···	···	···	···
1999/03/23	03:00 – 06:00	S17E11	1984	QS	sinistral	yes	···	···	···	04:54	152	48
1999/03/23	03:00 – 06:00	S36E24	1180	QS	sinistral	no	···	···	···	04:54	152	48
1999/04/18	07:13 – 07:48	N39E07	3768	QS	dextral	yes	B3.8	08:40	···	08:30	59	> 112
1999/05/22	06:12 – 11:12	S12E11	3708	QS	sinistral	yes	···	···	···	···	···	···
1999/06/08	10:02 – 11:48	S35E21	2088	QS	sinistral	yes	···	···	···	···	···	···
1999/06/24	12:48 – 13:36	N39W08	2808	AR8595	dextral	yes	C4.1	12:04	N29W13	13:31	partial halo	···
1999/07/01	02:24 – 04:00	S31W18	2404	QS	sinistral	yes	C5.4	01:41	S15W16	···	···	···
1999/08/20	13:13 – 16:36	N59W74	6888	QS	···	Limb[f]	···	···	···	18:06	346	88
1999/09/09	18:45 – 21:36	N34W41	6800	QS	dextral	yes	···	···	···	19:52	304	73
1999/09/12	00:24 – 01:25	S16W52	4176	QS	sinistral	Limb	···	···	···	00:54	271	121
1999/09/16	15:48 – 16:36	N49W44	13744	QS	dextral	Limb	···	···	···	16:54	partial halo 6	147
1999/09/20	04:00 – 05:00	S21E01	5672	QS	sinistral	no	C2.8	05:46	···	06:06	very faint halo	360
1999/10/13	08:12 – 09:36	N49E12	12992	QS	dextral	no	optical	···	···	09:50	4	109
1999/10/25	13:36 – 14:12	S36W19	4368	QS	sinistral	no	C1.2	14:40	···	14:26	partial halo 186	146
1999/11/09	14:35 – 15:31	N49E21	3280	QS	dextral	yes	···	···	···	no data	···	···

Table 2.1—Continued

Date	Filaments					EFRs	Flares			CMEs		
	Eruption Time [UT]	Position	Size [arc sec^2]	Type	Chirality	EFR[a]	Class	Time[b] [UT]	Location	Time[c] [UT]	Central PA[d] [deg]	AW[e] [deg]
1999/11/26	17:08 – 19:13	S46W04	3596	QS	sinistral	yes	C2.3	17:40	S11W08	17:30	partial halo	228
1999/12/28	22:00 – 23:48	S04E17	2368	QS	sinistral	yes	...	...	...	23:54	170	96
2000/01/08	03:06 –	S12E02	2004	QS	sinistral	yes	...	...	...	no data	...	...
2000/01/15	17:48 – 18:36	S43W58	6502	QS	sinistral	Limb	...	...	...	19:31	228	75
2000/04/11	19:48 – 20:12	S32W44	2304	QS	sinistral	Limb	...	...	...	20:30	210	45
2000/04/21	20:24 – 21:36	S05W03	2684	QS	sinistral	yes	...	...	...	...	...	...
2000/04/29	12:00 – 12:48	N04E07	2204	QS	dextral	yes	C3.0	11:23	S11W06	...	...	...
2000/07/07	07:13 – 13:13[dp]	N06W02	2340	QS	sinistral	yes	C5.6	08:42	N17E10	10:26	halo	360
2000/07/23	04:24 – 05:12	S12W06	2408	AR9091	sinistral	yes	optical	...	...	05:30	partial halo	161 > 181
2000/07/30	13:24 – 14:13	N18W17	2516	QS	dextral	no	...	...	...	...	...	
2000/09/05	18:00 – 20:36	S29E17	3136	QS	sinistral	yes	C1.6	21:21	S19W04	...	...	...
2000/09/12	11:10 – 11:40	S27W06	5236	AR9160	sinistral	yes	M1.0	11:31	S12W18	11:54	halo	360
2000/09/18	11:24 – 12:00	N19W46	6404	QS	dextral	yes	...	...	...	12:26	282	35
2000/09/27	14:48 – 15:36	S02E45	2706	QS	sinistral	no	...	...	...	...	...	...
2000/09/27	19:35 – 19:50	S31E17	2936	QS	sinistral	yes	optical	...	...	20:50	192	115
2000/09/28	06:12 – 07:13	N12E05	1320	QS	dextral	yes	...	...	...	...	...	...
2000/10/07	21:13 – 22:00	N47E27	4384	QS	dextral	yes	...	...	...	...	...	...
2000/10/15	15:12 – 17:12	N19W39	3124	QS	dextral	no	...	...	...	18:26	273	44

Table 2.1—Continued

	Filaments					EFRs	Flares			CMEs		
Date	Eruption Time [UT]	Position	Size [arc sec^2]	Type	Chirality	EFR[a]	Class	Time[b] [UT]	Location	Time[c] [UT]	Central PA[d] [deg]	AW[e] [deg]
2000/10/28	19:17 – 19:54	N18W62	2500	QS	dextral	yes	...	...	...	no data	...	...
2000/11/23	05:36 – 06:12	S15W49	3276	QS	dextral	yes	C5.4	05:34	S26W40	06:06	halo	360
2000/11/25	06:00 – 07:13	N31W62	3520	QS	dextral	Limb	...	...	...	07:31	305	44
2001/01/24	11:12 – 12:00	N27W07	2448	QS	dextral	no	...	...	...	...	...	...
2001/03/14	10:23 – 11:09	S28W34	2236	QS	sinistral	no	...	...	...	12:26	213	26
2001/04/02	10:48 – 13:13	S22W48	2608	QS	sinistral	Limb	...	...	...	11:26	270	80
2001/04/10	11:12 – 12:36	N19W29	2048	QS	dextral	yes	...	...	...	...	...	...
2001/04/22	23:52 – 00:30[n]	N37W34	4208	QS	dextral	yes	...	...	...	00:42/23	325	69
2001/04/23	12:03 – 12:26	S09W28	564	AR9431	sinistral	yes	C2.8	12:06	S14W17	12:39	228	91
2001/04/23	13:27 – 14:10	S32W63	2256	QS	...	Limb	...	...	...	...	...	...
2001/07/20	03:36 – 04:12	N35W27	2076	AR9538	dextral	yes	B7.6	03:15	...	05:06	357	26
2001/07/26	08:48 – 10:14	N23W81	3044	QS	sinistral	Limb	...	...	...	...	...	...
2001/08/01	20:28 – 20:56	S29W14	1176	AR9557	sinistral	no	...	...	...	no data	...	...
2001/08/02	19:49 – 23:48	N40E28	2144	QS	dextral	yes	C2.1	18:53	N24E31	00:06/03	...	...
2001/08/06	22:36 – 23:48	N28W94	2836	QS	dextral	Limb	...	...	...	...	...	...
2001/09/15	09:48 – 10:28	N24W69	4718	QS	dextral	Limb	...	...	...	...	...	...
2001/10/09	10:48 – 12:24	S26E03	1424	AR9653	dextral	no	M1.4 1h	10:46	S28E08	11:30	halo	360
2001/10/16	07:13 – 07:36	N05W74	3644	QS	sinistral	Limb	...	...	...	...	...	...

Table 2.1—Continued

	Filaments					EFRs	Flares			CMEs		
Date	Eruption Time [UT]	Position	Size [arc sec^2]	Type	Chirality	EFR[a]	Class	Time[b] [UT]	Location	Time[c] [UT]	Central PA[d] [deg]	AW[e] [deg]
2001/10/19	16:15 – 16:25	N18W40	1276	AR9661	sinistral	yes	X1.6	16:13	N15W29	16:50	halo	360
2001/12/05	15:48 – 16:24	N47W54	2060	QS	dextral	Limb	...	...	...	...	...	...
2002/01/06	10:36 – 11:52	S42W16	2036	QS	...	Limb	...	...	...	...	...	...
2002/01/14	22:14 – ^{dp}	S21W01	2572	QS	sinistral	no	...	...	...	no data	...	...
2002/01/23	16:27 – 17:13	N35E18	2092	QS	...	no	...	...	...	...	...	...
2002/01/28	10:00 – 11:00	S32E15	2458	QS	sinistral	yes	C4.6	11:05	...	10:54	143	62
2002/02/19	23:00 – ^{dp}	N53E15	5276	QS	...	Limb	...	...	...	02:54/20	36	41
2002/03/05	18:30 – 19:15	S11W26	5824	QS	sinistral	no	...	...	...	21:30	215	65
2002/04/22	22:37 – 23:24	S10W03	5380	QS	sinistral	yes	...	...	...	00:38/23	213	57
2002/05/21	20:16 – 20:26	N20E40	737	AR9960	dextral	yes	M1.5	21:20	N17E38	21:50	59	117
2002/05/22	03:00 – 03:36	S12W60	2140	QS	dextral	yes	C5.0 2h	04:00	S22W53	03:50	halo	360
2002/05/24	20:26 – 20:36	N18E14	218	AR9962	dextral	no	optical	20:40	N16E11	...	...	...
2002/06/04	17:47 – 17:57	N14W23	159	AR9974	dextral	yes	C1.0	18:06	N22W17	no data	...	...
2002/06/10	19:06 – 20:31	N33W19	3612	QS	dextral	no	...	...	...	...	...	...
2002/06/16	21:13 – 21:47	S25W45	262	AR9991	...	yes	C1.2	21:12	...	...	...	...
2002/06/17	22:53 – 23:13	N20E40	475	AR10001	dextral	no	optical	22:40	N14E22	...	...	...
2002/06/19	20:05 – 20:20	N20W15	225	AR10000	...	yes	optical	...	...	...	...	...
2002/07/01	20:32 – ^{dp}	S18W09	320	AR10016	sinistral	yes	C1.0	21:08	...	...	...	...

Table 2.1—Continued

	Filaments					EFRs	Flares			CMEs		
Date	Eruption Time [UT]	Position	Size [arc sec^2]	Type	Chirality	EFR[a]	Class	Time[b] [UT]	Location	Time[c] [UT]	Central PA[d] [deg]	AW[e] [deg]
2002/07/04	16:09 – 16:19	S18E06	393	AR10019	···	yes	C3.4	16:21	S19E06	18:54	180	45
2002/07/07	17:00 – 17:26	N08W49	4560	QS	dextral	yes	optical	···	···	18:06	293	65
2002/07/13	10:28 – 11:12	S24E28	2488	QS	sinistral	yes	···	···	···	11:30	147	40
2002/07/21	16:11 – 16:31	S16E02	472	QS	sinistral	yes	optical	15:47	S09W16	···	···	···
2002/07/23	14:30 – 18:20	N53W54	8148	QS	dextral	Limb	···	···	···	18:06	342	56
2002/07/26	15:37 – 15:48	N10W24	1184	AR10046	sinistral	yes	optical	···	···	···	···	···
2002/07/29	07:13 – 10:29	N32W40	4108	QS	dextral	yes	···	···	···	11:06	360	150
2002/08/06	16:59 – 17:19	S31W35	9900	QS	sinistral	no	···	···	···	18:25	218	134
2002/08/14	19:34 – 20:28	N10E17	408	AR10067	dextral	yes	M1.4	18:04	N10E23	···	···	···
2002/08/18	18:18 – 18:37	S09W17	596	QS	···	yes	C8.7	20:18	S07W20	21:54	203	140
2002/08/20	23:42 – 00:04[n]	N55W10	3692	QS	dextral	Limb	···	···	···	···	···	···
2002/09/15	19:52 – 20:17	N33E45	2140	QS	dextral	yes	···	···	···	21:30	59	41
2002/09/18	23:04 – 23:29	S22E03	2152	AR10119	sinistral	no	C1.0	21:48	···	···	···	···
2002/09/21	20:11 – 20:36	S11W22	408	AR10123	sinistral	yes	C2.6	20:34	S16W19	···	···	···
2002/09/22	10:28 – 11:48	N26W54	6700	QS	dextral	Limb	···	···	···	11:30	287	43
2002/09/29	22:20 – 01:25[n]	S26W00	2416	QS	sinistral	no	···	···	···	···	···	···
2002/09/29	22:20 – 01:25[n]	S13E21	2400	QS	sinistral	yes	···	···	···	23:54	146	22
2002/09/30	06:36 – 08:24	S12W87	1824	QS	sinistral	Limb	···	···	···	···	···	···

1. *Type:* Active region filaments form in polarity reversal regions of active region complexes, whereas quiescent filaments are usually found in quiet sun areas along polarity inversion lines between large-scale areas of opposite polarity(Feynman & Martin 1995).

2. *Chirality:* Chirality describes the handedness of filaments and it contains important information of the surrounding magnetic field. When viewed from the positive polarity side, the axial field of a dextral (sinistral) filament points to the right (left), respectively. Dextral and sinistral filaments can be recognized even without knowing the polarity on either side of filaments. Martin et al. (1993) discovered a no-exception correlation between chirality of filament channels, filaments, and their overlying coronal arcades: all dextral filaments are right-bearing and lying under left-skewed arcades, while all sinistral filaments are left-bearing and lying under right-skewed arcades (for a review, see Martin 1998). The chirality is determined by examining high resolution BBSO Hα images. If the filament barbs bear off to the right (left) of the filament's main axis then the filament is dextral (sinistral), respectively. In some cases the chirality of a filament could not be determined due to an obscure or complex Hα structure, which is indicated by the $(\cdots)$ in the 6th column of Table 2.1.

3. *Emerging Flux Regions (EFRs):* Since the sensitivity of longitudinal magnetograms decreases near the limb, "Limb" is used when the normalized distance from solar disk center is larger than $0.6R_{\odot}$ and new flux emergence could not clearly be established.

4. *Flares:* As mentioned in Section 3, Hα and EIT full disk observations, GOES soft X-ray flux profiles, and SGD solar event reports are used to identify flares associated with filament eruptions. Term "optical" refers to a flare visible in Hαfull disk images, which is either inconspicuous in soft X-rays flux profiles or it is of an insufficient magnitude to be officially classified as a flare.

Table 2.1—Continued

	Filaments					EFRs	Flares			CMEs		
Date	Eruption Time [UT]	Position	Size [arc sec^2]	Type	Chirality	EFR[a]	Class	Time[b] [UT]	Location	Time[c] [UT]	Central PA[d] [deg]	AW[e] [deg]
2002/10/10	19:03 – 20:08	N29W01	812	QS	dextral	no	···	···	···	no data	···	···
2002/10/29	23:28 – 01:13[n]	S14W40	3584	QS	···	yes	···	···	···	···	···	···
2002/11/19	21:00 – 00:00	S03W57	2800	QS	sinistral	Limb	···	···	···	···	···	···
2002/11/19	23:00 – 00:00	S47W63	2196	QS	sinistral	Limb	···	···	···	···	···	···
2002/12/29	01:13 – 02:36	S31W12	2584	QS	sinistral	yes	···	···	···	···	···	···
2003/01/20	15:12 – 18:24	N40W30	5000	QS	dextral	Limb	optical	···	···	18:30	315	105
2003/01/20	12:48 – 13:13	S02W36	3656	QS	sinistral	no	···	···	···	···	···	···
2003/01/20	20:24 – 21:12	N25E55	6250	QS	dextral	yes	optical	···	···	21:30	58	166
2003/01/30	08:12 – 09:33	N18W00	2480	QS	dextral	no	optical	···	···	10:06	partial halo 238	149
2003/03/25	17:15 – [dp]	N37W13	4076	QS	···	Limb	···	···	···	19:31	0	65
2003/04/26	20:33 – 21:18	N00E48	4160	QS	dextral	Limb	···	···	···	21:50	48	166
2003/06/11	17:56 – 18:56	S42E08	5088	QS	sinistral	no	M1.8	17:27	S16E23	no data	···	···
2003/06/14	03:24 – 04:12	N24W36	4328	QS	dextral	yes	optical	···	···	···	···	···
2003/08/05	17:54 – 18:34	N15W21	6084	QS	dextral	yes	···	···	···	19:31	336	57
2003/09/24	06:00 – 07:13	S20W27	5952	QS	sinistral	no	···	···	···	···	···	···
2003/10/26	00:36 – 01:13	S22W66	2188	QS	sinistral	Limb	C3.2	00:45	···	01:31	256	75

[a]EFR: Emerging Flux Region

[b]Time: Flare Onset Time (UT)

[c]Time: First C2 Appearance Time (UT)

[d]Central PA: central position angle measured from Solar North in degrees (counter clockwise), provided by LASCO CME catalogue

[e]AW: angular width, provided by LASCO CME catalogue

[f]Limb: Near Limb

[dp]dp: data gap

[n]n: next day

5. *CMEs:* The first time of appearance in the LASCO C2 FOV, the central position angle (PA), and angular width are provided in the LASCO CME catalog. In the 11th column of Table 2.1, $(\cdots)$ is used to indicate that a CME associated with the filament eruption could not be found and "no data" refers to the few occasions, where no LASCO data were available.

2.5 Discussion

2.5.1 Chirality

Our statistics of filament chirality shows that filaments in the northern hemisphere are predominantly dextral, while filaments in the southern hemisphere are sinistral. This agrees with the observations of Martin et al. (1993) who reports that both solar hemispheres have a distinct chirality. This hemispheric pattern seems to suggest that differential rotation and/or Coriolis force participate in twisting the magnetic structures (Priest et al. 1996).

A one-to-one correspondence between filament chirality and the sign of magnetic helicity in interplanetary CMEs (ICME) has been reported in a number of studies: dextral (sinistral) filaments contain left-handed (right-handed), negative (positive) magnetic helicity (Bothmer & Schwenn 1994; Rust & Martin 1994; McAllister & Martin 2000; Yurchyshyn et al. 2001), respectively. Also, Leamon et al. (2002) reported a 95 % correspondence between the helicity of the magnetic clouds associated with eruption of filaments and the heliosphere where those filaments were located. The sign of magnetic helicity in an active region can be used to predict the orientation of the magnetic field associated with a CME and, furthermore, the likelihood of a geomagnetic storm (Yurchyshyn et al. 2001).

2.5.2 New Flux Emergence

EFRs often occur in active regions and play a significant role in filament eruptions and flare production (Liggett & Zirin 1985; Feynman & Martin 1995). The relation between

filament eruptions and new flux emergence is shown in the 7th column of Table 2.1.

After excluding events located far away from disk center, where the detection of new flux emergence was difficult, a sample of 80 eruptive filaments suitable to study the magnetic field evolution is obtained. 54(68%) events were accompanied by new flux emergence. The new flux usually appeared in the vicinity of an eruptive filament and within 15 hours prior to the filament eruption, suggesting that new flux emergence plays an important role in destabilizing filaments.

2.5.3 Flares and CMEs

Eight events without the corresponding LASCO data were listed in Table 2.1 but excluded from Figure 2.1. The top panel of Figure 2.1 shows the heliographic latitude of flares and CMEs that were associated with eruptive filaments. Asterisks are used to indicate filament eruptions associated with neither flares nor CMEs. Diamonds denote the occurrence of a flare and triangles show the occurrence of CMEs. Squares were used in cases, where both flares and CMEs were detected. Out of 98 events, 55(56%) of the filament eruptions were accompanied by CMEs.

The above number is considerably weaker than the 94% association reported for EPs reported by Gilbert et al. (2000) and the 83% for radial events by Gopalswamy et al. (2003), but much higher than the 10% to 30% range given by Yang and Wang (2002). This apparent difference can be explained as follows: Gilbert et al. (2000) and Gopalswamy et al. (2003) considered only prominence eruptions, i.e., limb events. In contrast to these studies, the events listed in Table 2.1 are mainly disk events. It is likely for some disk events that the associated CMEs are very faint and could not be detected by LASCO. The low CME association reported by Yang & Wang (2002) was most probably due to the fact that they did not distinguish between filament disappearances and eruptions, while disappearances are explicitly excluded in this study. Moreover, the size criteria that they employed were different from ours. They included all disappearance events, while this

study mainly considered filaments with a size of at least 2,000 arc sec^2. Thus, the results of Yang & Wang (2002) provide a lower estimate, since smaller eruptive events might be associated with fainter CMEs and therefore, are more likely to be missed in LASCO data.

The bottom panel of Figure 2.1 shows the distribution of eruptive filaments as a function of distance from the solar disk center. The light gray bars represent the number of filament events, while the dark bars are the number of associated CMEs. The fraction of CMEs to filament eruptions is given in percent for each bar in the histogram. The highest fraction of 70% occurs in the range of $R = 0.4$ to $0.6R_{\odot}$.

Table 2.2 distinguishes between active region and quiescent filament eruptions and relates them to flares and CMEs. Here, the term "flare" refers to both optical Hα and GOES X-ray flares. Active region filament eruptions are more likely to be associated with flares (95%) than quiescent filament eruptions (28%), since large-scale magnetic shear and strong magnetic field in an active region can store plenty of magnetic energy to be released in flares (Hagyard et al. 1984). Out of a total of 85 quiescent filament eruptions, 46 or 54% are accompanied by CMEs, while only 23 or 27% events produce flares. This eminent relation between filament eruptions and CMEs suggests that filament eruptions in a quiescent region or at the periphery of an active region will more likely be associated with a CME that is not itself associated with a flare. The above flare association could, quite possibly, be higher if we consider the fact that some flares during the eruption may be too weak to be observed in either GOES soft X-rays or Hα.

Table 2.2 Active Region and Quiescent Filaments and Their Relation to Flares and CMEs

Filament Type	Total	with Flare		w/o Flare		with CME		w/o CME		No LASCO Data	
Active Region Filaments	21	20	95%	1	5%	9	43%	10	48%	2	9%
Quiescent Filaments	85	23	27%	62	73%	46	54%	33	39%	6	7%
Total	106	43	41%	63	59%	55	52%	43	40%	8	8%

2.5.4 Halo CMEs

Halo CMEs have received considerable attention, since they are responsible for major interplanetary disturbances and geomagnetic storms (Burlaga et al. 1981; Wilson & Hildner 1984). Because the southwardly component B_z of the interplanetary magnetic field (IMF) is responsible for magnetic reconnection between the IMF and Earth's magnetic field, it plays an important role in determining the amount of particle energy that is injected into the magnetosphere (Arnold 1971; Akasofu 1981). Usually, the presence of a strong and prolonged southward directed IMF is associated with enhanced geomagnetic activity. For ICMEs with their axial magnetic field oriented along the north-south line, the magnitude of the southward component is largely determined by this axial field and the sign of magnetic helicity plays a minor role. At the same time, for CMEs with east-west oriented axial fields, both sign and magnitude of its southward component is largely determined by the magnetic helicity of the CME (Yurchyshyn et al. 2001).

Table 2.3 summarizes results for seven eruptive filaments, taken from Table 2.1, associated with halo CMEs and geomagnetic storms. The first four columns are the same as in Table 2.1, while 5th column shows the orientation of CMEs, which is assumed to be the same as the orientation of the axial magnetic field of the corresponding filaments. The linear fit speed of the CMEs, which was taken from the SoHO/LASCO CME Catalog, is listed in the 6th column. The last three columns present the transit time of the ICME and the peak values of the Dst and Kp indices during the subsequent geomagnetic storms. Five out of seven halo CMEs were associated with geomagnetic storms with the peak Dst values ranging between -45 and -187 nT. The peak Kp values were found to be between 5 and 8 nT. All but one geomagnetic event could be predicted based on the chirality of the CME's magnetic field. The exception is the CME on 2001 October 19. Considering its west-east directed axial magnetic field and sinistral chirality of the associated filament, the leading edge of the magnetic cloud should have had a northward directed component and thus this event should be not associated with a significant geomagnetic activity. However, a strong

storm occurred two days after the CME launched. Examination of Advanced Composition Explorer (ACE) magnetometer data revealed that the magnetic field at the leading edge was indeed northward and the storm was caused by a strong southward component in the shock region preceding the interplanetary ejecta.

2.6 Summary

In summary, phenomena of solar activity associated with filament eruptions were studied. A total of 106 major filament eruption events, identified from 1999 January 1 to 2003 December 31, were included in the sample for this study.

1. Excluding eight events without corresponding LASCO data, 55 (56%) out of 98 events were associated with CMEs. This CME association is lower than the 94% fraction reported by Gilbert et al. (2000) and the 84% fraction by Gopalswamy et al. (2003), but it is considerably higher than the 10% to 30% value association found by Yang & Wang (2002).

2. Active region filament eruptions have a considerably higher flare association (95%) compared to quiescent filament eruptions with only 27% association. On the other hand, quiescent filament eruptions (85 events) are more likely to be accompanied by CMEs than flares.

3. Out of 80 disk events, 54 or 68% events were associated with new flux emergence. This suggests that new flux emergence plays an important role in destabilizing filaments.

4. The chirality and the orientation of magnetic fields associated with seven halo CMEs and their relationship to geomagnetic storms are determined. Our results seem to support earlier reports that the geoeffectiveness of a halo CME can be predicted from its orientation and the sign of magnetic helicity (Yurchyshyn et al. 2000).

Table 2.3 Filament Eruptions Associated with Halo CMEs, and their Geo-Effectiveness

	Filaments			Halo CMEs		Geomagnetic Storms		
Date	Type	Position	Chirality	Orientation	Speed[a] [km/s]	Transit Time[b] [days]	Peak Dst[c] [nT]	Peak Kp[d] [nT]
1999/09/20	QS	S21E01	sinistral	east-west	604	2.8	−173	8
2000/07/07	QS	N06W02	sinistral	south-north	453	...	...	...
2000/09/12	AR	S27W06	sinistral	east- west	1550	1.4	−45	3
2000/11/23	QS	S15W49	dextral	east-west	492	...	...	...
2001/10/09	AR	S26E03	dextral	west-east	973	2.4	−70	5
2001/10/19	AR	N18W40	sinistral	west-east	901	2.3	−187	7
2002/05/22	QS	S12W60	dextral	north-south	1494	1.6	−109	8

[a]Linear fit speed from SoHO/LASCO CME Catalog

[b]Transit time from solar onset to storm peak

[c]Dst = −30: weak storm, Dst = −50: moderate storm and Dst = −100: intense storm

[d]Kp = 5: moderate storm and Kp = 6: intense storm

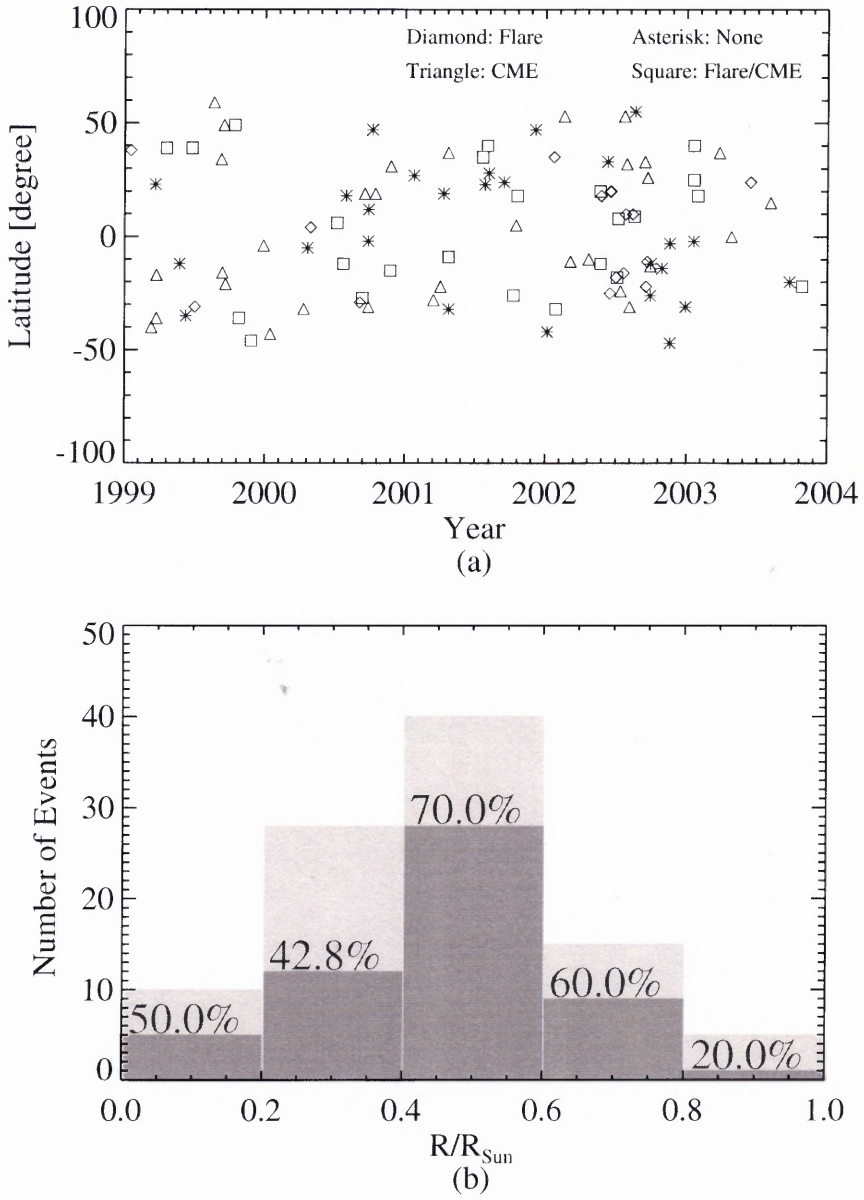

Figure 2.1 *Top panel:* Latitudinal distribution of eruptive filaments and their overall relation to flares and CMEs. Asterisks denote filament eruptions, which were associated with neither flares nor CMEs. Diamonds refer to flares, triangles to CMEs, and squares to both flares and CMEs, which were related to filament eruptions. *Bottom panel:* Frequency distribution of filament eruptions and associated CMEs as function of their distance from disk center. The histogram in light gray corresponds to filament eruptions and the histogram in dark gray represents the associated CMEs, where the fraction of CMEs to filament eruptions is given for each interval.

CHAPTER 3

MAGNETIC RECONNECTION RATE AND FLUX-ROPE ACCELERATION

3.1 Introduction

Filament eruptions, coronal mass eruptions and solar flares are spectacular manifestations of solar eruptions. It is generally believed that they are initiated by the sudden release of energy stored in the coronal magnetic field.

Numerous theoretical models for solar eruptions and the evolution of the reconnecting current sheet (RCS) have been developed (e.g., Van Tend & Kuperus 1978; Kaastra 1985; Martens & Kuin 1989; Forbes & Priest 1995; Amari et al. 1996; Forbes & Lin 2000; and see Lin 2003 for review). These models can be arranged into four categories: (1) non-force-free models, (2) ideal MHD models, (3) resistive MHD models and (4) ideal-resistive hybrid models. Some of the most used eruption models are: the sheared arcade model (Mikić et al. 1988; Linker & Mikić 1994), the break-out model (Antiochos et al. 1999) and the flux-rope catastrophic model (Van Tend & Kuperus 1978; Forbes & Isenberg 1991; Forbes & Priest 1995). The first two eruption models are of the resistive MHD model type and, on the basis of numerical simulation, require magnetic reconnection to trigger the eruption. The third eruption model, constructed via analytic solution of the ideal-resistive hybrid model, indicates quantitatively that magnetic reconnection does not necessarily play an essential role in triggering a catastrophe eruption. However, magnetic reconnection does help a catastrophe develop into a plausible CME-like eruption, as well as giving rise to intense heating that accounts for the associated flares (Lin 2001; Lin, Forbes & Isenberg 2001).

Observationally, solar eruptions can be manifested in the form of ejected X-ray plasmas, erupting filaments or coronal mass ejections (CMEs) (Cheng et al. 2003). The morphological evolution of two-ribbon flares, characterized by two bright separating rib-

bons in the chromospheric, usually occurs during the solar eruptive phenomena (eruptive filaments or CMEs) and is believed to be the lower-atmosphere manifestation of magnetic reconnection at progressively higher levels and the subsequent energy release in the corona (Choudhary & Gary 1999).

There is increasing observational evidence of a temporal correlation between flares and eruptive phenomena (Gosling et al. 1976; MacQueen & Fisher 1983; Zhang et al 2001; Qiu et al. 2002, 2004; Wang et al. 2003). This correlation leads us to believe that flares, eruptive filaments, and CMEs are different manifestations of the same physical process involving magnetic reconnection.

Because eruptive filaments and CMEs are both considered to be erupting flux ropes in many theoretical models, I will not distinguish them except for a specific purpose. Instead, the term "flux-rope" is used throughout the rest of the chapter. However, we must keep in mind that the occulting disk of coronagraphs block part of the lower corona. Consequently, the initial stage of a flux-rope eruption usually cannot be observed by coronagraphs such as the Large Angle Solar Coronagraph (LASCO; Brueckner et al. 1995).

The central interest in this work is to find statistical correlation between the magnetic reconnection rate and the acceleration of flux-ropes. From a sample of thirteen well-observed two-ribbon flares that are associated with rising flux-ropes, there appears to be a tendency that increasing reconnection rates are usually associated with increasing flux-rope accelerations at the early stage. The temporal correlation between the magnetic reconnection rate and the flux-rope acceleration has also been verified.

In the next section formulas to determine the reconnection rate from observations are introduced. The data sets and methods of analysis are described in sections 2 and 3, respectively. In section 4, on the basis of a sample of 13 two-ribbon flares which are associated with eruptive flux-ropes, the correlation between magnetic reconnection rates and flux-rope accelerations are quantified. Finally, our observational results are summarized and briefly discussed in section 5.

3.2 How to Determine the Reconnection Rate from Observations

As mentioned previously, the expansion of flare ribbons is the chromospheric signature of the progressive magnetic reconnection in the corona in which new field lines reconnect at higher and higher altitudes. Since the magnetic reconnection in the corona is hardly observed directly, chromospheric observations provide indirect means to probe the physics of the coronal magnetic reconnection (Schmieder et al. 1987; Falchi, Qiu & Cauzzi 1997).

In a simplified two-dimensional model, the release of energy during a flare occurs in a RCS formed at an X-type neutral line (Forbes & Priest 1984, 1986). The rate at which the magnetic flux is converted into the diffusion region, in terms of the electric field E_{rec} in the RCS, can be inferred by measuring the flare ribbon expansion speed V_r and the normal component of the magnetic field B_n swept by the flare ribbons: $E_{rec} = V_r B_n$ (Forbes & Priest 1984, 1986). It should be emphasized that this equation is derived based on a few assumptions: First, the length of the current sheet is equal to the length of the ribbons. Second, neither the length of the ribbons nor the normal magnetic changes with time significantly. Finally, there is a translational symmetry along the ribbon, i.e., a two-dimensional configuration.

More generally, Forbes and Lin (2000) considered the rate of photospheric magnetic flux change φ_{rec} instead of the electric field in the region of newly closed field lines. The flux change rate can be evaluated by the following equation (Forbes & Lin 2000):

$$\varphi_{rec} = \int E_{rec}\, dl = \frac{\partial}{\partial t} \int B_n\, da \quad , \tag{3.1}$$

where dl is the length along the RCS and da is the newly brightened area swept by the flare ribbons.

E_{rec} and φ_{rec} provide a measure of the reconnection rate inside the current sheet, and the measurement itself is not dependent on specific models. In this manner, we are particularly interested in the observational signatures of two-ribbon flares that are associated

with flux-rope eruptions. The reconnection rate can be inferred and compared with the rising motion of flux-ropes. Essentially, the reconnection rate and the flux-rope acceleration focus on important features of the flare- "flux-rope" models, therefore, provide a stringent test of the scenarios in which the ejection of solar material and magnetic reconnection are physically linked. Progress in this research area has been made recently by Lin & Forbes (2000) and Qiu et al.(2004).

The central interest in this work is to find statistical correlation between the magnetic reconnection rate and the acceleration of flux-ropes. From a sample of thirteen well-observed two-ribbon flares that are associated with rising flux-ropes, there appears to be a tendency that increasing reconnection rates are usually associated with increasing flux-rope accelerations at the early stage. The temporal correlation between the magnetic reconnection rate and the flux-rope acceleration has also been verified in this chapter.

3.3 The Data Sets

Big Bear Solar Observatory (BBSO) Hα full-disk images are used as the primary data source to trace the flare ribbon expansion and the filament rising motion. BBSO Hα observations are suitable because of their high-cadence (one or more image frames per minute), high-resolution (approximately $1''$ pixel^{-1}) and superior detail and contrast (Martin 1989). In the cases where there were data gaps in the BBSO observations, we resorted to Hα full-disk images obtained at Kanzelhöhe Solar Observatory (KSO) in Austria, which is a station in our global Hα network. In addition, an X10.0 white-light flare which occured on 2003 October 29, obtained at the National Solar Observatory/Sacramento Peak, was also added into our study list. Running difference images from Extra-Ultraviolet Imaging Telescope (EIT), on board the *Solar and Heliospheric Observatory* (*SOHO*), were used to supplement Hα data in identifying the height of the rising filament in the cases where the filaments motion can not be determined unambiguously from Hα observations.

The CME height-time data is provided by the LASCO web site that has been com-

piled by Seiji Yashiro and Grzegorz Michalek under the guidance of Nat Gopalswamy (*http* : *//cdaw.gsfc.nasa.gov/CME_list*). Michelson Doppler Imager (MDI) magnetograms were used to measure the longitudinal component of the magnetic fields, which approximate the normal component of the magnetic field B_n because all of the flares in our study occur near the disk center. Additionally, light-curves from the *Geostationary Operational Environmental Satellite* (*GOES*) soft X-ray, Yohkoh and *Reuven Ramaty High Energy Solar Spectroscopic Imager* (*RHESSI*) hard X-ray and Owens Valley Solar Array (OVSA) microwave data were also collected to study the evolution of flare emissions. If no hard X-ray and microwave observations were found, which was the case for some of the events that are under discussion, the time derivative of GOES soft X-ray light-curve are used to indicate the evolution of flare nonthermal emission (Neupert 1968).

3.4 Data Analysis

3.4.1 Methods

As discussed in the introduction, the magnetic reconnection rate can be deduced by measuring the expansion of flare ribbons across the magnetic field. I recently developed an image segmentation technique, which applies "region growing" and "adaptive boundary-base" methods (Jahne 1997, Gonzalez & Woods 2002), to derive the expansion speed of two-ribbon flares V_r and the newly brightened areas swept by flare ribbons da, automatically (for more details, see Qu et al. 2003 and 2004). An example (July 26, 2002) is shown in Figure 1.1. This M8.7 flare, starting at 20:51 UT and lasting until 21:29 UT, occurred in the active region NOAA 9960 and was associated with a CME. Figure 3.1 shows the selected Hα images at BBSO from 21:00 to 21:21 (left column) and corresponding sketches to illustrate the morphological evolution of flare region (middle column) and newly brightened area (right coumn), which are obtained by our automatic program. A full description of our methods has been given by Qu et al. (2004). Compared to the earlier studies, our

recent method has the advantage of avoiding the difficulty in determining the velocities of the ribbons, and therefore, being applicable to well-defined two-ribbon flares as well as flares with irregular shape as well.

From V_r and da, one may derive two forms of the magnetic reconnection rate: the electric field inside RCS, $E_{rec} = V_r B_n$, and the rate of magnetic flux participating in the reconnection, $\varphi_{rec} = \frac{\partial}{\partial t} \int B_n da$. Uncertainties in E_{rec} and φ_{rec} caused by the influence of background noise were estimated to be less than 40% at the time of the peak value (Qu et al. 2004). Methods and uncertainties of these measurements are discussed in detailed by Qiu et al (in preparation).

The velocity and acceleration of the filaments and CMEs are derived numerically as the first and second derivative of corresponding height with respect to time. The uncertainty of measuring the filament height is estimated to be less than 4 pixels in each image, depending on the sharpness of the rising front. The typical rise phase of a filament lasts tens of minutes, and our Hα observations have a regular cadence from 20 seconds to 1 minute. With the sufficient number of Hα images and observational evidence (Wang 2004), filament trajectories can straightforwardly be assumed to follow a linear growth during this period. In this case, the uncertainty in the values of filament velocity and filament acceleration arise both from the uncertainty and the time interval in measuring the filament height; the larger the uncertainty in the height and the shorter the time interval, the larger the uncertainty of the estimated values. The uncertainty in CME heights and speeds are estimated to be less than 5% and 10%, respectively. However, the cadence of LASCO observations (around 30 minutes) limits our estimation of the propagation of the uncertainty to some extent. In other word, a few of the measurements of CME heights, as well as a lack of evidence that CMEs display a constant acceleration at the initial stage of eruption, yields a very large uncertainty in the CME acceleration.

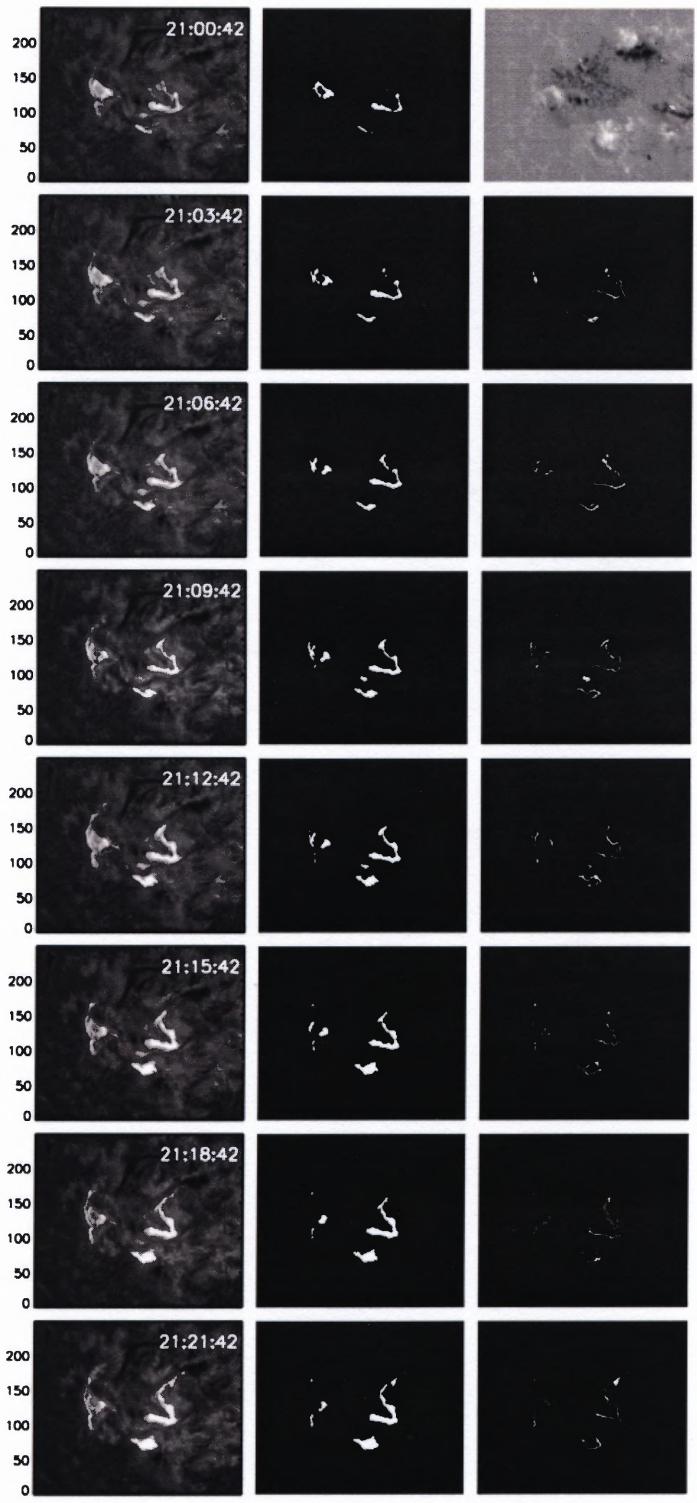

Figure 3.1 The selected Hα images (left column) at BBSO from 21:00 to 21:21 UT and corresponding sketches of morphological evolution of flare region (middle column) and newly brightened area (right column). Top right panel: aligned MDI magnetogram.

3.4.2 The Correlation Coefficient

The correlation between two variables is the degree to which there is a "linear relationship" between them. Correlation is usually expressed as a "coefficient" (C.C.) which quantifies the strength of that linear relationship between the variables. C.C. ranges from -1 to +1. Positive values of C.C. indicate that as one variable increases, the other increases. Negative values of r indicate that as one variable increases, the other decreases. A value of +1 or -1 indicates that the data fall on a straight line. In this study, the C.C. is calculated using IDL CORRELATE function that computes the linear Pearson correlation coefficient of two vectors.

The following general categories indicate a quick way of interpreting a calculated C.C. value:

1. 0.0 to 0.2, Very weak to negligible correlation
2. 0.2 to 0.4, Weak,low correlation (not very significant)
3. 0.4 to 0.7, Moderate correlation
4. 0.7 to 0.9, Strong, high correlation
5. 0.9 to 1.0, Very strong correlation

3.5 Results

The events under study were selected on the basis of the following criteria: (1) disk events; (2) continuous and complete observation of the flares and the associated flux-rope rising motions; (3) exhibiting clear flare expansion and, if present, filament rising motion. Criterion (1) follows from the fact that, for disk events, B_n can be easily measured as the longitudinal component provided in MDI magnetograms. Criteria (2) and (3) are required because we need track the outer edge of flare ribbons and the rising fronts of eruptive filaments to infer the magnetic reconnection rate and acceleration of the filaments.

It is found thirteen two-ribbon flare events that satisfy all three criteria. They are listed in Table 3.1. All but one event are well-observed by BBSO or KSO Hα images. The exception is the X10.0 flare in NOAA Active Region 10486, which was observed in the near-infrared (NIR) continuum at 1.56 μm (Xu et al. 2004). These events are classified into three groups (2nd column) by their associated eruptive phenomena: Group A consists of two-ribbon flares with both eruptive filaments and CMEs; Group B consists of two-ribbon flares with rising, not eruptive, filaments and without CMEs; and Group C is composed of two-ribbon flares with CMEs, but without apparent filament motion. Column (3) lists the date of the events. The subsequent columns provide instances of flares (columns (4)−(9)), filaments (column (10)) and CMEs (columns (11)−(12)).

Table 3.2 summarizes the results deduced from the observations, including the maximum ribbon expansion speed (V_r, column (3)), the maximum photospheric magnetic field strength (B_n, column (4)), the maximum electric field in RCS (E_{rec}, column (5)), the maximum magnetic flux change rate (φ_{rec}, column (6)), the maximum filament acceleration ($Accel_{fila.}$, column (7)) and the maximum CME acceleration ($Accel_{CME}$, column (8)). The last three columns of Table 2 list the time intervals of the E_{rec}, $Accel_{filament}$ and $Accel_{CME}$ after the hard X-ray spike. If they peak after the time of the hard X-ray spike, the value is positive. Otherwise, the value is negative.

Our observational findings on the basis of sample events are described in detail below:

Acceleration of erupting filaments is mainly in the range of $0.05 - 0.4 kms^{-2}$, up to $3 kms^{-2}$. The maximum E_{rec} and φ_{rec} mostly occur in the range of $0.2 - 5 Vcm^{-1}$ and $0.5 - 6 \times 10^{18} Mxs^{-1}$, respectively. In the case of the extremely dramatic flare on October 29, 2003, E_{rec} reaches a magnitude of about $38 Vcm^{-1}$. The electric field is found to be generally comparable with most observational results (Poletto & Kopp 1986; Wang et al. 2003, 2004; Qiu et al., 2004) and simulation results (Martens & Kuin 1989; Lin 2002; Cheng et al. 2003). The electric field strength found above implies strong heating and

Table 3.1 List of Events in this Study

Event	Group*	Date	Flare						Filament	CME	
		yy/mm/dd	Class	NOAA*	Begin	Peak	End	Location	Rising Time	Time*	Comment
1	A	00/09/12	M1.0	QS*	11:31	12:13	13:13	S12W18	10:30 – 12:00	11:54	Halo
2	A	00/09/27	optical*	QS	...	...	...	S31E17	19:30 – 19:50	20:50	Loop with loop-like core
3	A	01/04/23	C2.8	9431	12:06	12:23	12:36	S14W17	12:02 – 12:18	12:40	Loop front with cavity and core
4	A	01/10/19	X1.6	9661	16:13	16:30	16:43	N15W29	16:15 – 16:25	16:50	Halo
5	A	02/05/21	M1.5	9960	21:20	21:39	22:00	N17E38	20:16 – 20:26	21:50	Loop front with cavity and trailing material
6	A	03/05/27	X1.3	0365	22:56	23:07	23:13	S07W17	22:58 – 23:04	23:26	Halo
7	A	04/03/04	optical	QS	...	...	...	N20W10	19:50 – 21:00	22:30	Loop front
8	A	04/03/30	C2.0	0581	22:53	23:08	23:45	S05E02	22:30 – 22:46	no data*	...
9	B	00/02/17	M2.5	8869	18:41	18:52	19:05	S25W16	18:56 – 19:28	...	...
10	B	02/08/26	optical	0087	...	...	...	S07E20	21:00 – 21:40	...	...
11	C	01/08/25	X5.3	9591	16:23	16:45	17:04	S17E34	...	16:50	Halo
12	C	02/07/26	M8.7	0044	20:51	21:12	21:29	S19E26	...	22:06	Halo, cavity and core follow
13	C	03/10/29	X10.0	0486	20:37	20:49	21:01	S15W02	...	20:54	Halo

* Group A: two-ribbon flare with rising filament and eruption, and CME; Group B: two-ribbon flare with rising filament but no eruption, and without CME; Group C: two-ribbon flare with CME, but without apparent filament motion.

*NOAA: Active Region Number

*Time: First C2 Appearance Time (UT)

*optical: a flare visible in Hα observations but is either inconspicuous in soft X-ray flux profiles or is of an insufficient magnitude to be officially classified as a flare.

*QS: quiescent area

*no data: no LASCO data

Table 3.2 Data Taken and Deduced for Events Listed in Table 1

Event	Date yy/mm/dd	Max. V_r $[kms^{-1}]$	Max. B_n [Gauss]	Max. E_{rec} $[Vcm^{-1}]$	Max. φ_{rec} $[10^{18}Mxs^{-1}]$	Max. $Accel_{fila.}$ $[kms^{-2}]$	Max. $Accel_{CME}$ $[kms^{-2}]$	$\triangle T_1$* [min]	$\triangle T_2$* [min]	$\triangle T_3$* [min]
1	00/09/12[1,2]	25	200	1.0	2.0	0.3	0.4	-5	5	10
2	00/09/27	11.4	46.4	0.24	0.5	0.14	0.2	...	...	...
3	01/04/23	6.4	396.5	0.74	0.8	0.33	0.02	10	3	95
4	01/10/19[1]	74.7	308.0	21.0	14.7	3.0	0	-1	-5	
5	02/05/21	17.9	297.5	4.9	6.0	0.16	0.8	6	6	20
6	03/05/27	65.3	387.5	14.4	8.7	1.8	0.02	-3	-5	40
7	04/03/04	8.1	121.0	0.9	1.4	0.14	unavailable*	...	...	...
8	04/03/30	30	200.0	2.5	0.7	0.12	no data*	8	-15	...
9	00/02/17	13.0	195.1	1.4	2.3	0.3	...	25	24	...
10	02/08/26	16	195.0	1.6	0.7	0.06	...	...	...	...
11	01/08/25	25.8	461.5	8.9	4.9	...	0.4	-10	...	20
12	02/07/26[2]	19.0	334.5	2.8	6.0	...	-0.2	0	...	80
13	03/10/29[3]	63.8	919.6	37.8	10.8	...	0.06	-1	...	12

*$\triangle T_1$: $\triangle T_1$ = Time of max. E_{rec} - Time of HXR at maximum. If no Hard X-ray observation was found, the time derivative of GOES soft X-ray light curve is used.

*$\triangle T_2$: $\triangle T_2$ = Time of max. $Accel_{filament}$ - Time of HXR at maximum

*$\triangle T_3$: $\triangle T_3$ = Time of max. $Accel_{CME}$ - Time of HXR at maximum

[1]1: see Qiu et al. 2004 for detailed case study

[2]2: see Wang et al. 2004 for detailed case study

[3]3: see Xu et al. 2004 for detailed case study

*unavailable: CME height-time data of this event is not readily released at the SOHO LASCO web site.

*no data: no LASCO data

particle acceleration which are responsible for the high energy emissions (Cheng et al. 2003; Qiu et al. 2002, 2004). A graphical description of the derived maximum E_{rec} versus the observed magnitude of flares is shown in Figure 3.2. As expected, the magnitude of the flares increase as E_{rec} increases with a high correlation coefficient (C.C.), 0.85.

In this study, erupting filaments are treated as proxies for the initial stages of rising flux-ropes. The temporal correlation of the evolution of flare nonthermal emission, the magnetic reconnection rate and the filament acceleration is examined and illustrated by one example in which an X1.3 flare occurred in active region NOAA 10365 on May 27, 2003 and was accompanied by a filament eruption and a halo CME. In Hα, the filament has a maximum acceleration of 1.8 km s^{-2} at 23:02 UT, and the bright flare ribbons appeared at 22:40 UT and lasted until 23:30 UT. In the LASCO observations, the CME was first apparent at 23:50 UT. Figure 3.3 displays the temporal evolution of the inferred E_{rec}, φ_{rec}, accelerations of corresponding erupting filament and CME, and the light-curves of *GOES* soft X-rays and *RHESSI* hard X-rays. The maximum E_{rec}, 14.4 V cm^{-1}, and the maximum φ_{rec}, $8.7 \times 10^{18} Mxsec^{-1}$, occur at 23:04 UT and 23:02 UT, respectively. The impulsive hard X-ray emission in the $50-100keV$ energy band spikes at 23:03 and 23:07 UT. Apparently, E_{rec}, φ_{rec}, filament acceleration and flare nonthermal emission reach their maximum values at almost the same time. It is necessary to point out that good temporal correlation generally exists for all events listed in Table 3.1, which confirms the findings of Qiu et al. (2004).

The above observations, which were in good quantitative agreement with some theoretical simulation results (Martin & Kuin 1989; Cheng et al 2003), also indicate that the inferred macroscopic electric field in the RCS plays an important role in accelerating nonthermal particles to emit hard X-rays and microwaves (Qiu et al. 2004).

As mentioned in the introduction, the primary purpose of this work is to investigate the correlation between the magnetic reconnection rate and the flux-rope acceleration. To better illustrate our deduced results in Table 3.2, Figure 3.4 displays scatter diagrams of the reconnection rate (namely, E_{rec} and φ_{rec}) versus the acceleration of filaments in a loga-

rithmic scale. Figure 3.5, for the purpose of comparison, plots the reconnection rate versus the acceleration of the CMEs. Those events without the corresponding filament motion or the CME are excluded from Figure 3.4 and Figure 3.5. All values refer to their maxima that were found on each events. The Error bars that are attached to each sign indicate the uncertainty of the measurement. Figure 3.4 shows that the increasing reconnection rate is usually associated with an increasing filament acceleration. More specifically, the linear C.C. between E_{rec} and $Accel_{filament}$ is about 0.97 and that between φ_{rec} and $Accel_{filament}$ is about 0.94. Such high values distinctly indicate a very strong correlation and a dependable relationship. The solid lines fit the paired data to linear models. The best-fit linear models are as follows: $E_{rec} = -0.46 + 6.8 \times Accel_{filament}$, and $\varphi_{rec} = 0.26 + 4.6 \times Accel_{filament}$. By contrast, Figure 3.5 shows a loose and irregular distribution of data points. Low C.C.s, -0.14 between φ_{rec} and $Accel_{CME}$ and -0.18 between E_{rec} and $Accel_{CME}$, signify little, if any, correlation. This may stem from the fact that the CME acceleration was measured in LASCO C2 and C3 fields of view ($2 - 30R_{\odot}$, 1 $R_{\odot}$ = one solar radius) and hence did not sample the heights in the low corona. The insufficient number of measurements also implies a very large uncertainty in CME acceleration. As a result, the error bars for the values of CME acceleration are not shown in Figure 3.5.

It is suggested by Gopalswamy and Thompson (2000) that the acceleration of CMEs is strongly dependent on the altitudes at which the CMEs are observed. Specifically, Zhang et al.(2001) investigated the kinematic evolution of four CMEs in the lower corona and found that the acceleration of CMEs takes place from 1.3 to $4.6R_{\odot}$. Similar results were also obtained by Shanmugaraju et al. (2003) who claimed that the peak in the acceleration mostly occurs below $3R_{\odot}$. In this sense, the acceleration of most CMEs might decrease, or even stop, before they appear in LASCO C2 coronagraph images. By which time the velocity of the CMEs have obtained a nealy constant, or slightly decreasing, value. That is, the maximum acceleration of CMEs derived from LASCO C2/C3 data is usually not really informative.

The velocity of CMEs at C2 might be useful because it is the cumulation of the CME acceleration at its early stage ($Vel_{CME} = \int Accel_{CME} dt$) and, therefore, in some way conveys information about the acceleration during that stage. Thus, the velocity of CMEs is an alternate way for examining the correlation between the magnetic reconnection rate and the evolution of CMEs. A graphical display of the CME velocity versus the reconnection rate is presented in Figure 3.6. Inspection of this display immediately reveals that the correlation improved markedly: the paired data Vel_{CME} and E_{rec} has a moderate C.C., 0.64, while the C.C. for Vel_{CME} and φ_{rec}, 0.32, implys a low degree of correlation.

3.6 Summary and Discussion

Measurements of E_{rec} and φ_{rec}, which both indicate the magnetic reconnection rate inside the current sheet, together with the observational flux-rope acceleration, provide an interesting approach to study the magnetic reconnection rate during the eruptive process. Thirteen well-observed two-ribbon flares, with corresponding eruptive flux-ropes, were studied to investigate and quantify the correlation between the magnetic reconnection rate and flux-rope acceleration. The main results obtained from the sample are summarized as follows:

1. The deduced electric field E_{rec} and the flux change rate φ_{rec} mostly occur in the range of $0.2 - 3 V cm^{-1}$ and $0.5 - 2 \times 10^{18} Mxs^{-1}$, respectively. The magnitude of the *GOES* X-ray flare (expressed in units of watts m^{-2}) increases with E_{rec} as shown in Figure 1.1. The electric field strength found above is enough to accelerate electrons to very high energies which may account for the strong hard X-ray emissions (Cheng et al. 2003).

2. The magnetic reconnection rate is temporally correlated with the evolution of flare hard X-ray emission and the acceleration of the accompanying erupting filaments. Our results confirm the earlier finding of a good temporal correlation, which is indicative a physical link, between mass acceleration and the magnetic reconnection rate in flares/CMEs (Qiu et al., 2004).

3. The C.C. between E_{rec} and $Accel_{filament}$ is about 0.97 and that between φ_{rec} and $Accel_{filament}$ is about 0.94. Such high values indicate a very strong correlation and a dependable relationship between the magnetic reconnection rate and the acceleration of erupting filaments. The paired data are best fitted to the following linear models: $E_{rec} = -0.46 + 6.8 \times Accel_{filament}$, and $\varphi_{rec} = 0.26 + 4.6 \times Accel_{filament}$.

4. It appears, from our results, that there is no correlation between the magnetic reconnection rate and the CME acceleration (C.C. is less than 0.2). This may be caused by the temporal-spatial gap between the disk observations of the flares and filaments and LASCO (C2-C3) observations of CME fronts. CMEs may cease, or even stop accelerating, before they appear in LASCO C2 coronagraph images. Hence, in general, it is less meaningful to compare the magnetic reconnection rate and the CME acceleration.

5. The velocity of CMEs might be an alternate way to investigate the relationship between CMEs and flares that involve magnetic reconnection. The correlation between the velocity of CMEs and the magnetic reconnection rate improves somewhat (C.C. $\sim$ $0.32-0.64$), but not enough to make me confident in the relationship between the velocity of CMEs and the magnetic reconnection rate. The reason is that CME velocity in C2 somewhat conveys the information of the acceleration. The exact acceleration progress below C2 still remains unknown. Another complementary way of looking at this is, in a flare/CME loop/giant arch system, the separatrix bubble that surrounds the flux rope is the product of magnetic reconnection. During the eruptive progress, the bubble swells much faster than the flux ropes. Therefore, the "flux rope" observed by coronagraphs might actually be the rapidly expanding separatrix bubble (Lin 2004).

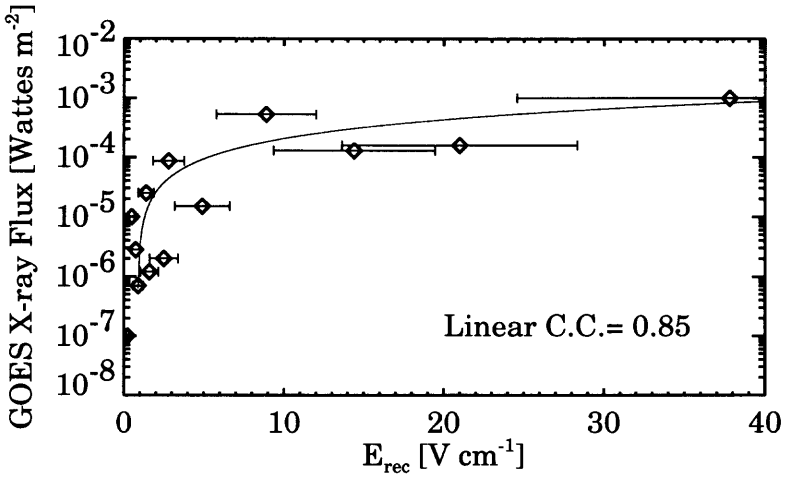

Figure 3.2 Scatter diagram of derived maximum E_{rec} with estimated error bars versus observed flare magnitude. The solid line is a fit of the data points in the form of $Flux = -2.0 \times 10^{-5} + 2.3 \times 10^{-5} \times E_{rec}$ with the correlation coefficient of 0.85.

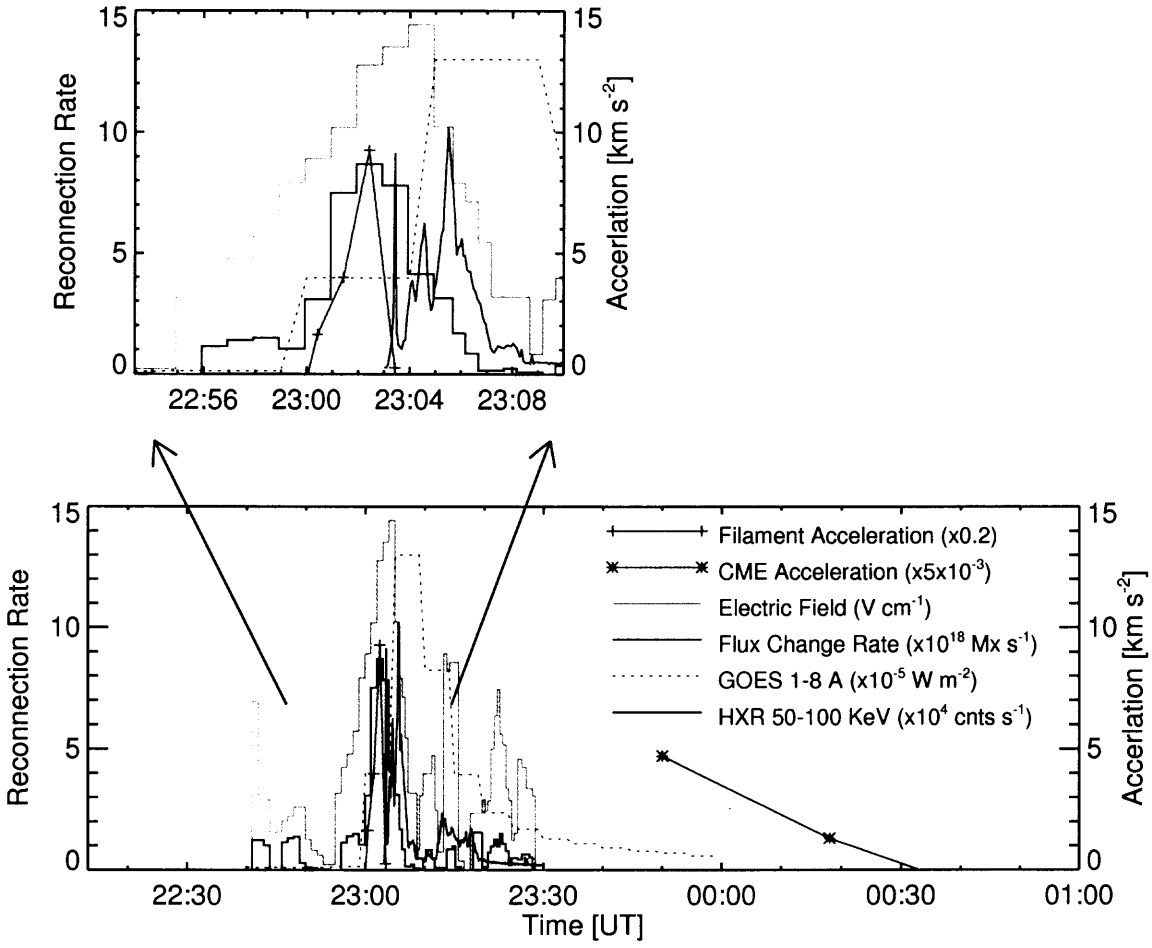

Figure 3.3 Temporal evolution of E_{rec} and φ_{rec} derived for the X1.3 flare on 2003 May 27, compared with the evolution of the acceleration of corresponding erupting filament and CME, soft X-ray and hard X-ray light curves. The top panel is the same as the bottom panel, but is magnified for a selected time period.

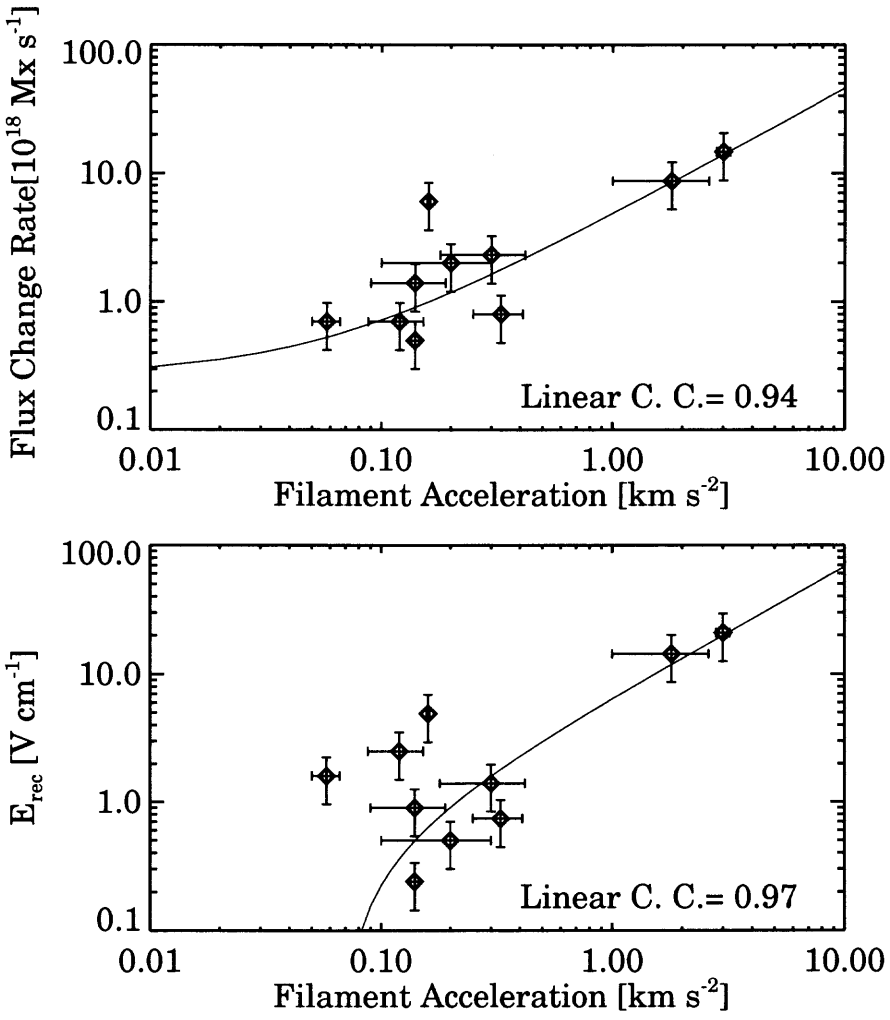

Figure 3.4 Top: Scatter diagram of maximum φ_{rec} versus maximum filament acceleration in a logarithmic scale. The solid line is a fit of data points of φ_{rec} and $Accel_{filament}$ in the form of $\varphi_{rec} = 0.26 + 4.6 \times Accel_{filament}$ with the correlation coefficient of 0.94; Bottom: Scatter diagram of maximum E_{rec} versus maximum filament acceleration in a logarithmic scale. The solid line is a fit of data points of E_{rec} and $Accel_{filament}$ in the form of $E_{rec} = -0.46 + 6.8 \times Accel_{filament}$ with the correlation coefficient of 0.97; Error bars attached to each sign indicate the uncertainty of the measurement.

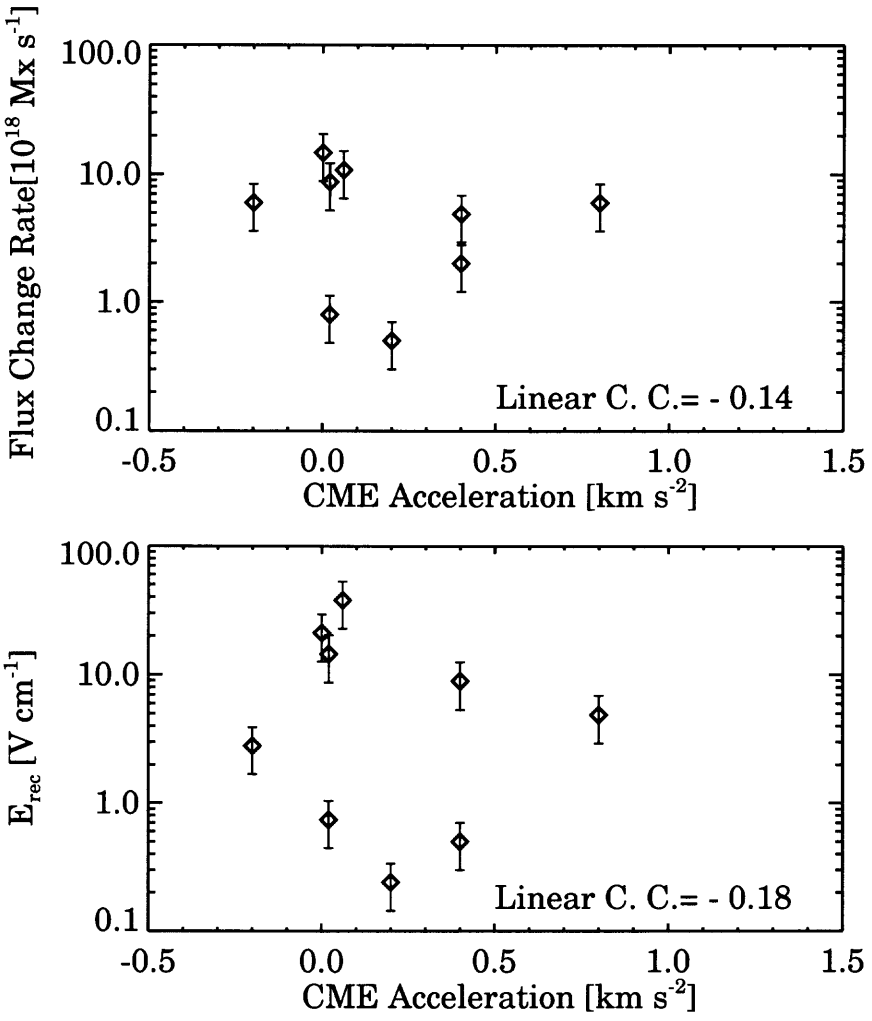

Figure 3.5 Scatter diagram of maximum φ_{rec} with error bars versus maximum CME acceleration in a logarithmic scale; Bottom: Scatter diagram of maximum E_{rec} with error bars versus maximum CME acceleration in a logarithmic scale. The correlation coefficients are -0.14 and -0.18, respectively. The error bars for the values of CME acceleration are not shown because they might be very large as a result of an insufficient number of measurements during the acceleration phase of the CMEs.

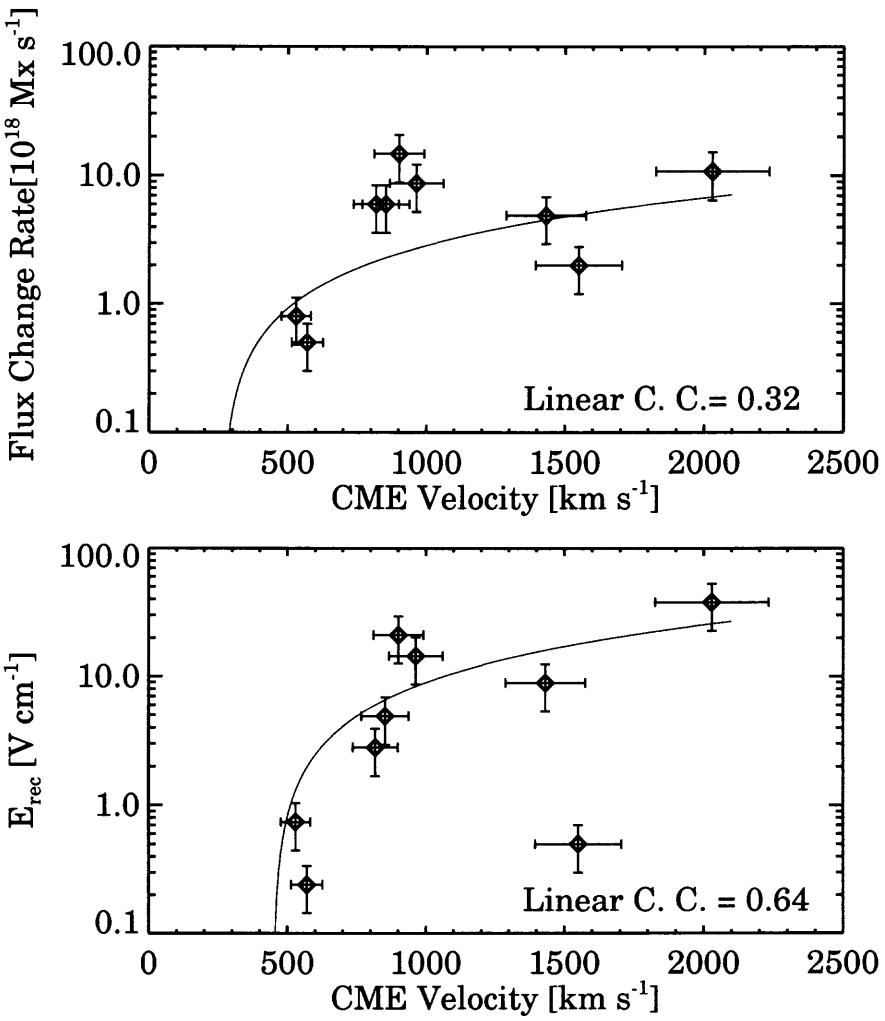

Figure 3.6 Scatter diagram of maximum φ_{rec} versus CME velocity at C2 in a logarithmic scale. The solid line is a fit of data points of φ_{rec} and Vel_{CME} in the form of $\varphi_{rec} = -1.0 + 0.004 \times Vel_{CME}$ with the correlation coefficient of 0.32; Bottom: Scatter diagram of maximum E_{rec} versus CME velocity at C2 in a logarithmic scale. The solid line is a fit of data points of E_{rec} and Vel_{CME} in the form of $E_{rec} = -7.3 + 0.02 \times Vel_{CME}$ with the correlation coefficient of 0.64; Error bars attached to each sign indicate the uncertainty of the measurement.

CHAPTER 4

MAGNETIC RECONNECTION RATE OF A TWO-RIBBON FLARE

4.1 Introduction

In the previous Chapter, a statistical correlation between the magnetic reconnection rate and the acceleration of flux-ropes is found from a sample of thirteen well-observed two-ribbon flares that are associated with rising flux-ropes. A positive and strong correlation is found with a cross correlation coefficient of 0.93– 0.97 between the magnetic reconnection rate and the acceleration of erupting filaments. This Chapter presents the result on a case analysis of a quiet-sun flare associated with an erupting filament and a fast CME on 2000 September 12. The flare exhibits a clear two-ribbon separation motion over several hours, which can be used to infer the evolution of the coronal magnetic reconnection. The Kanzelhohe Solar Observatory (KSO) and Solar and Heliospheric Observatory (SoHO) observations also provide continuous observations of the filament activation and eruption, which can be used to infer the dynamics of the CME at its take-off. Combinations of ribbon separation and filament/CME height would give us a 3-D physical picture associated with the eruptive flare. It is also possible to investigate the physical connection between the flare dynamics, filament eruption and CME quantitatively.

4.2 Observations and Data Reduction

The primary data source used in the current study are from full disk Hα data, with 1 arcsec pixel resolution and 1 minute cadence, obtained from KSO station on September 12, 2000. KSO had complete coverage of the M1 flare and the associated filament eruption at about 12 UT. Figure 4.1 is the time sequence of KSO Hα images showing the evolution of the event. It is a classical two-ribbon flare accompanied by the filament eruption.

The same event was covered by SOHO EIT, MDI and LASCO observations. It

is clearly associated with a fast Halo CME. MDI data provides full disk magnetograms, which are aligned with Hα data for the study of magnetic properties of moving ribbons. Figure 4.2 compares Hα image and the corresponding MDI magnetogram.

4.3 Results

4.3.1 Temporal Evolution

The top panel of Figure 4.3 shows GOES soft X-ray light curve of 1 to 8 Å and its derivative. The GOES soft X-ray light curve is used to represent the time profile of the flare energy release. To investigate the electron acceleration in the impulsive phase of the flare, the hard X-ray and microwave observations are essential. Unfortunately, there are not such data. Therefore the time derivative of GOES soft X-ray light curve is used to represent the hard X-ray time profile, assuming that the so-called Neupert effect is valid in this event.

The middle panel Figure 4.3 shows the average ribbon separation distance as a function of time. The position of the ribbon was defined by the location of the moving front. This flare exhibits a rather regular pattern of ribbon-separation motion, with both ribbons moving away from and nearly perpendicular to the magnetic neutral line.

The lower two panels of Figure 4.3 show the height-time profiles of the filament and CME front respectively. The solid line denotes the measurements of the filament height in Hα images with 1-minute cadence, and the '+' symbols represent measurements from EIT 195Å images with a 12 minute cadence. The measurement was not easy, because the contrast of the filament decreased rapidly as it moved up. The lateral displacement is measured and projected to the vertical direction based on the disk position of the filament. Of course, it is assumed that the filament moved up exactly vertically in the local solar coordinate system. Given the uncertainties in the measurements, the figure shows that the filament height profiles measured from the two kinds of images are consistent. The triangle symbols in the bottom panel of Figure 4.3 indicate the heights of the associated halo CME

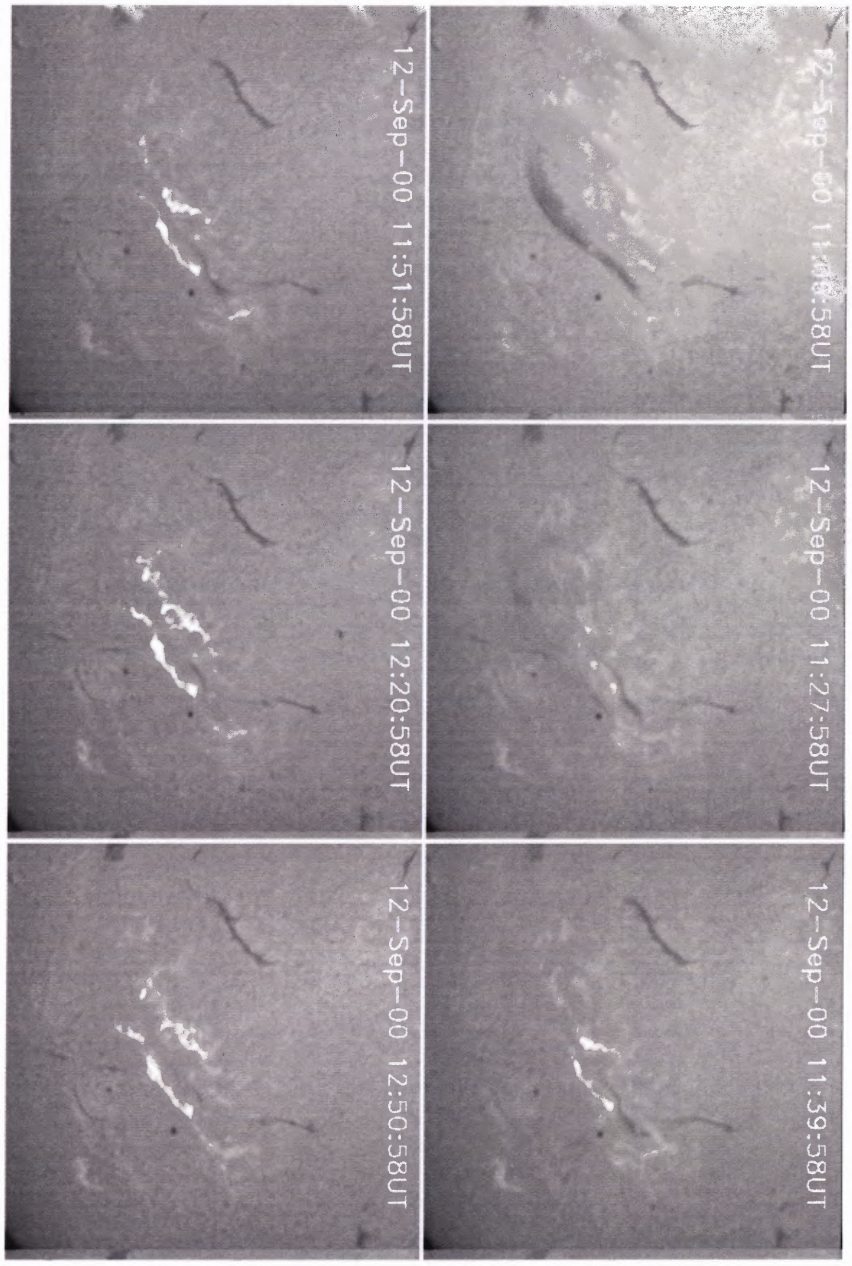

Figure 4.1 A sequence of Hα images showing the evolution of the flare and the disappearance of filament. The field of view is 512 by 512 arcsec.

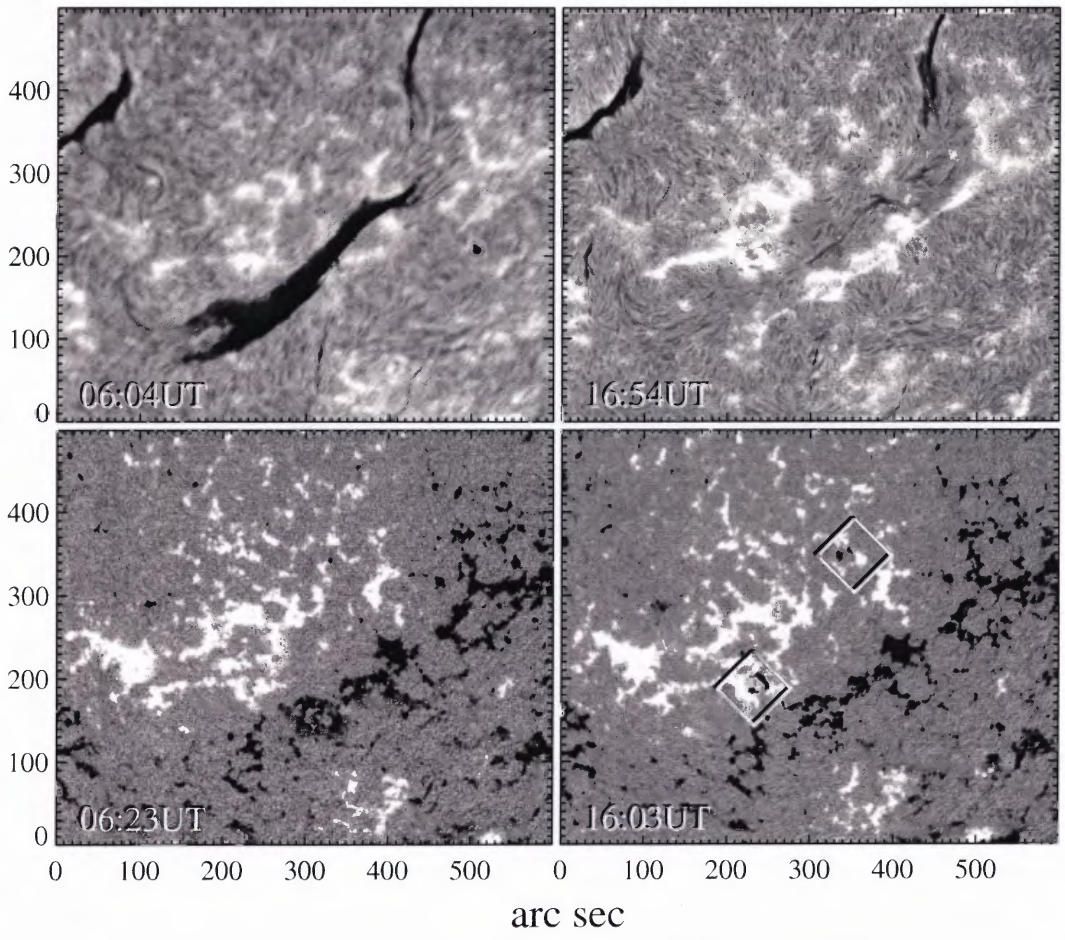

Figure 4.2 Comparison of a Hα image with corresponding magnetogram. Two bipoles emerged alongside the eruptive filament. The top two panels are Hα images taken before and after the eruption obtained at KSO and BBSO, respectively. The bottom two panels are MDI magnetograms. The two bipoles, as indicated by a square box, emerged on the positive polarity side of the filament.

front measured by Dr. Seiji Yashiro (*http://cdaw.gsfc.nasa.gov/CME_list/*). According to his measurements, the CME was first seen in LASCO C2 field at 11:54 UT, and the front speed measured from a linear fit is 1,500 km s^{-1}. Because of the limited FOVs of EIT and LASCO, one cannot identify the filament and CME in the same image. However, EIT and LASCO observations overlapped at around 12 UT when the filament and CME were observed by the two instruments separately.

Then these distance/height profiles are fitted to hyperbolic functions of time. The fits and the velocity profiles are shown in Figure 4.4. As shown in Figures 4.3 and 4.4, there are two stages in the ribbon-separation motion: a fast separation stage in the first 20 minutes of the event and a substantially slower stage afterwards. The filament started to rise about 30 minutes before the appearance of the flare ribbons, reaching a velocity of several tens of km s^{-1}. However, after the flare onset ($\sim$1120 UT), it was rapidly accelerated to over 200 km s^{-1} before becoming invisible in Hα ($\sim$1140 UT), and to at least 540 km s^{-1} when it moved beyond the limb in the EIT field of view around 12 UT. The fast stage coincides with the rising phase of the derivative of the soft X-ray light curve, i.e., the impulsive phase of the flare energy release when most of the flare non-thermal electrons are accelerated. On average, the speed of the ribbon separation during the impulsive phase of the flare is over 10 km s^{-1}, and the average speed in the later stage is about 1 km s^{-1}. Our observations therefore indicate that the fast ribbon motion corresponds to a greater energy release rate.

With certain assumptions, the above observations also allow us to reasonably estimate the acceleration rate of the CME at its takeoff in several ways. In the first way, the filament eruption and CME may be treated as mass ejections driven by the same mechanism in the same system at the early stage of the mass ejections. Estimated from the velocity profiles in Figure 4.4b, from 11:00 to 12:00 UT, the average acceleration rate was 260 m s^{-2}. The filament was not accelerated at a constant rate. From 11:40 to 12:00 UT, the average acceleration rate reached 380 m s^{-2}. In the second way, the CME is regarded to take off at 11 UT when the filament was observed to start rising in the EIT field of view.

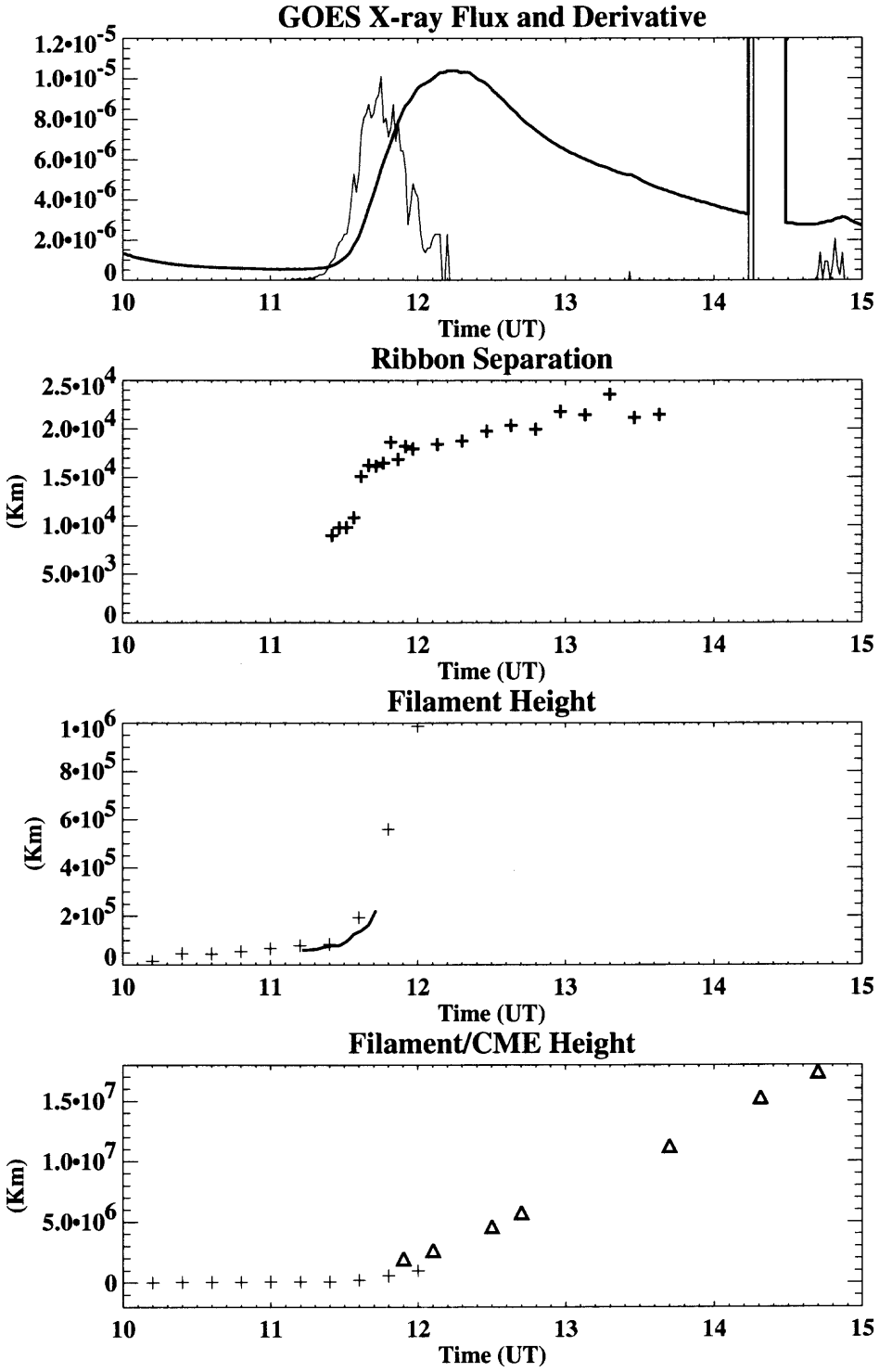

Figure 4.3 Top panel: GOES X-ray flux as a function of time in the energy channel of 1 to 8 Å. Second panel: mean flare ribbon separation as a function of time. Third panel: filament height as a function of time. The solid lines are KSO Hα measurements and the pluses are from SOHO EIT measurements. Bottom panel: EIT filament height and LASCO CME Height.

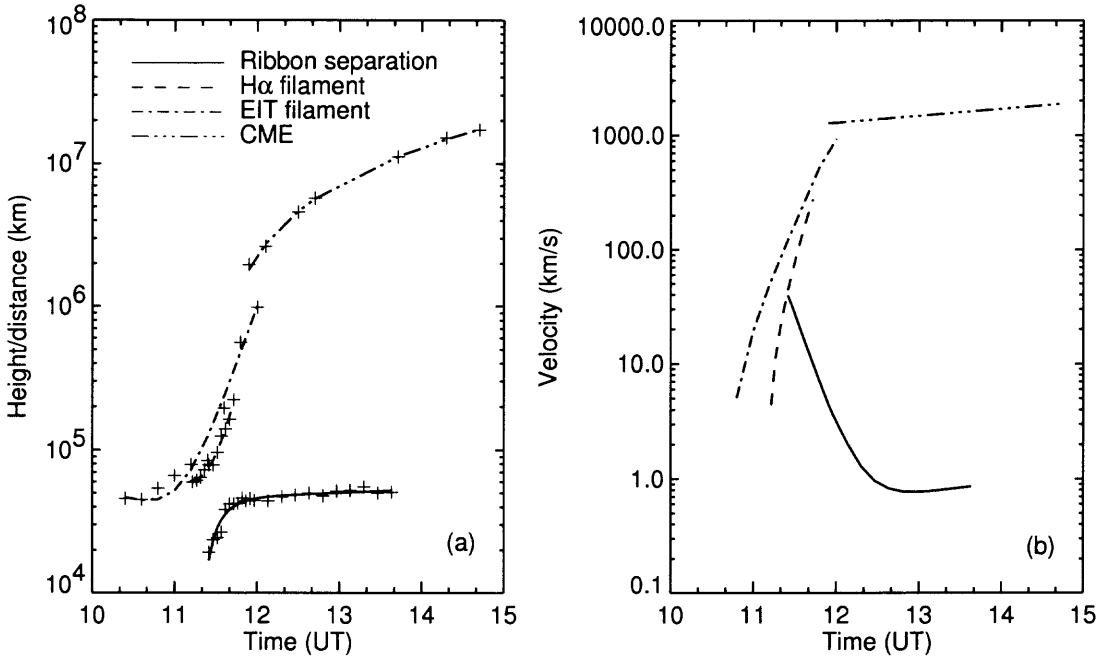

Figure 4.4 Left panel: time profiles of the flare ribbon separation, filament heights measured from KSO and EIT images, and CME heights measured by Dr. Yashiro (*http://cdaw.gsfc.nasa.gov/CME_list/*). The lines indicate the least-squares fits to hyperbolic functions. Right: velocity profiles of the ribbon separation, filament, and CME derived from the fits of the height profiles.

Accordingly, to accelerate the CME to 12:70 km s^{-1} at around 12 UT requires an average acceleration rate of 350 m s^{-2}. The acceleration rates estimated from these two methods are basically consistent, with the CME acceleration rate possibly a little higher than the filament due to the rapid expansion of the system. After 12 UT, the acceleration rate of the CME was estimated to be 58 m s^{-2} using the hyperbolic fit of the CME velocity profile in Figure 4.4b. Dr. Yashiro also estimated the CME acceleration rate to be 58 m s^{-2} from a second order fit of the height-time profiles (*http://cdaw.gsfc.nasa.gov/CME_list/*). These estimates suggest that fast acceleration of the mass ejections occurred before 12 UT, most likely during the impulsive phase of the flare. The rate of the fast acceleration is about five times that of the slow acceleration. This result is consistent with Zhang et al. (2001), yet our measurements are made with a better data coverage, under the assumption that the erupting filament and CME can be regarded as being accelerated in the same framework.

4.3.2 Electric Field Along the Current Sheet

Our results in the last section show that the speed of the ribbon separation resembles the rate of the flare energy release through magnetic reconnection. It is also of our interest to explore the spatiality of the ribbon motion representative of the energy release rate from the observational point of view. For this purpose, we track the separation speed at all locations along the ribbon as a function of time. It is found that the speed of the separation was not uniform along the flare ribbon, but at every point, the motion exhibits the same evolution pattern as the averaged separation mode shown in Figures 4.3 and 4.4. Therefore, the data are divided into two time bins: fast and slow separation stages. Figure 4.5 displays the speeds of the ribbon motion (away from the magnetic neutral lines) as a function of position along the ribbon. The positive and negative numbers represent the upper (north) and lower (south) ribbons, respectively. The thick lines represent the fast moving stage corresponding to the impulsive phase of the flare, and thin lines, the slow moving stage during the decay phase of the flare. In the first stage, the maximum speed V_t along the ribbon was over 10 km

s^{-1}, while in the following stage the maximum V_t was about 1 km s^{-1}.

The electric field $E_c = V_t B_n$ is derived as a function of ribbon position and plotted in the middle and bottom panels of Figure 4.5. The line-of-sight magnetic field B_n was measured from MDI observations. First, the evolution of E_c exhibits the same pattern as the speed. During the early time bin, the flare has a much stronger electric field of order 1 V cm^{-1} on average, while in the later time bin E_c is around 0.1 V cm^{-1}. Since E_c is proportional to the magnetic reconnection rate at the reconnecting point, our results confirm that the flare energy release is most efficient when the magnetic reconnection rate is also big. While during the decay phase lasting for about 2 hrs, the magnetic reconnection still continues at a slow rate. Second, Figure 4.5 shows that E_c is inhomogeneous along the ribbon, most likely indicating the inhomogeneity in the magnetic reconnection rate along the ribbon. Such inhomogeneity should be determined by the magnetic configuration in the corona.

4.4 Conclusions and Discussions

This Chapter presents the detailed study on the temporal and spatial properties of a quiet-sun two-ribbon flare. This event exhibits a good example of a standard solar flare characterized by the long duration, filament eruption, two-ribbon separation, and its association with a fast CME. Observations from various instruments provide an almost complete coverage of the dynamic evolution of this event. The most important result is the differences in the two evolution stages of the event, which is evident in several aspects and summarized in Table 4.1.

The two evolution stages are distinguished by the sudden switch of the electric field amplitude and mass acceleration rate. The rapid stage coincided with the impulsive phase of the flare energy release, yielding clear evidence that the impulsive flare energy release is governed by the fast magnetic reconnection in the corona.

The parameters derived in this study for the two-stage evolution of the dynamics and

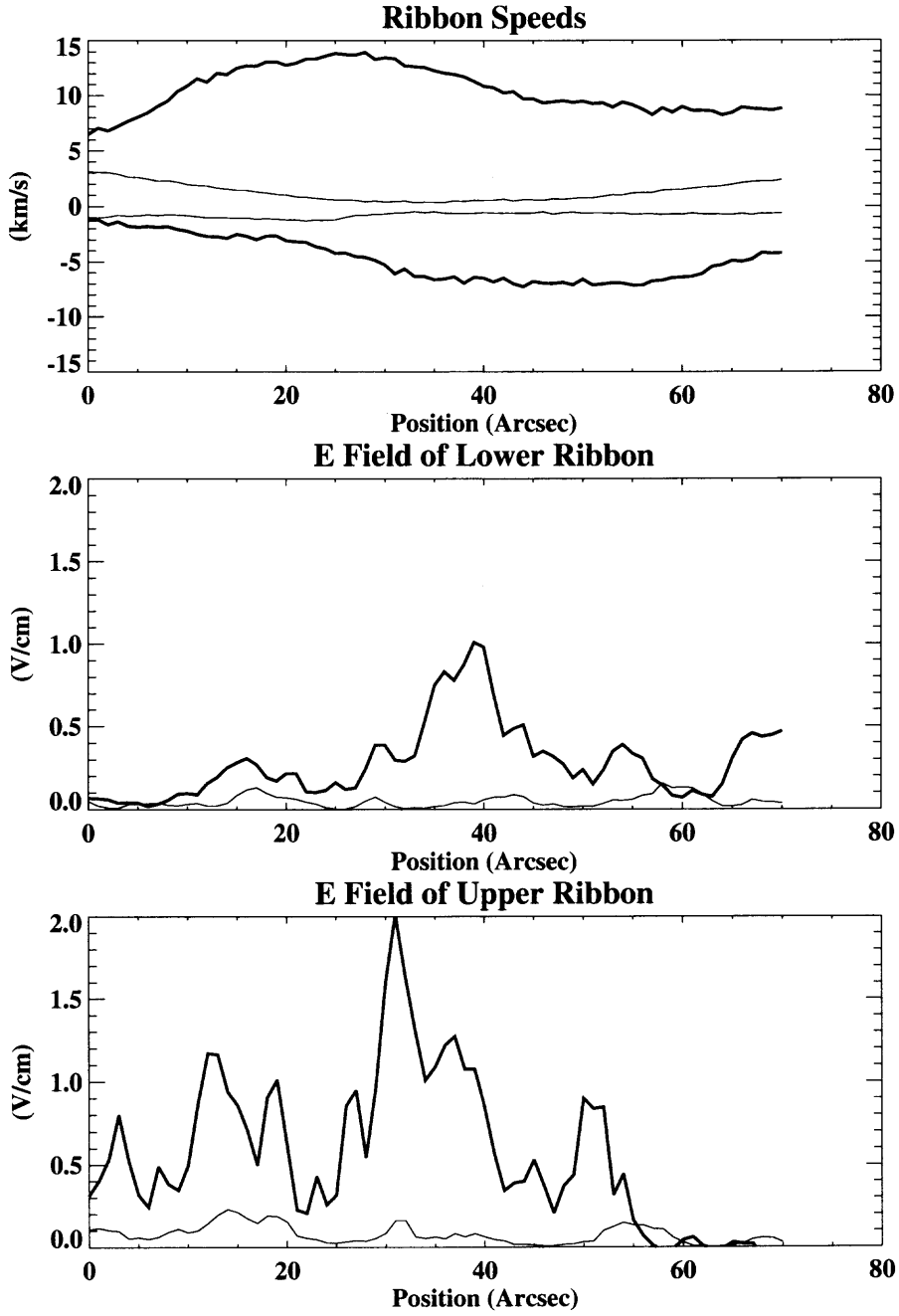

Figure 4.5 Top panel: the mean ribbon moving speeds along ribbons. Thick lines are for the time period of 1125 to 1200UT (time bin 1), and thin lines are for the time period of 1200 to 1350UT (time bin 2). Middle and bottom panels are derived electric fields for the lower and upper panels, respectively. Again the thick lines are for the time bin 1 and thin lines are for the time bin 2. The electric fields are derived from the ribbon moving speed and line-of-sight magnetic fields measured at the location of ribbons.

magnetic reconnection should provide information for theoretic modelling. A few questions stemmed from this study and their answers may help reveal the underlying physics. First, the two evolution stages are distinguished by the sudden switch of the electric field amplitude and mass acceleration rate. What is the mechanism of such switch? Is it due to a sudden change in the magnetic configuration, such as opening of the magnetic field lines, at that particular time? What is the physics behind the apparent coincidence between the magnetic reconnection rate and the dynamical evolution of the mass ejections? Second, apart from the two-stage evolution, Figure 4.4b also shows that during the first stage, while the velocity profile of the filament shows the filament being accelerated, the velocity profile of the ribbon motion suggests a deceleration. From an observational point of view, the sample of such studies should be enlarged to understand whether such anti-correlation can be established or it is purely an accident due to uncertainties in data analysis. Theoretically, shall we or shall we not expect such results?

Answers to these questions are important for understanding the physical mechanisms governing the dynamical evolution and magnetic reconnection in eruptive solar events. Some CME models have been presented which do not involve magnetic reconnection (e. g., Low 1994), but in many other cases, CMEs and flares are associated though in a way yet unclear to us. In the first place, even given the sharp contrast between the spatial scales of CMEs and flares, the radiative energy in a typical eruptive flare, which is released mainly through magnetic reconnection, is comparable to the kinetic energy car-

Table 4.1 Ribbon Separation, Electric Field, and Acceleration of Eruptive Filament in the Two Evolution Stages.

		Rapid Stage [11:20 – 11:40 UT]	Slow Stage [11:40 – 13:40 UT]
Ribbon Separation	$[kms^{-1}]$:	15	1
Electric Field	$[Vcm^{-1}]$:	1	0.1
Filament Acceleration	$[ms^{-2}]$:	over 300	58

ried by ejected masses. More importantly, even though past studies have found it hard to conceive a causal relationship between flares and CMEs, it remains intriguing what role the magnetic reconnection plays in the framework of the large-scale eruption. The configurations invoked by both the flux rope and break-out models, if correctly depicting the real situation, would naturally address the link between the rate of the magnetic reconnection and the rate of mass acceleration at least during the early stage of the event, because the laws of magnetic flux and mass conservation are to be observed. The direct relationship between the two, such as the time profiles of magnetic reconnection and CME acceleration may be calculated given a specific magnetic configuration.

A somewhat different but not unrelated issue raised in this study also deserves further investigation in the future. In Figure 4.5, one can see that the amplitude of the electric field, nominally representative of the magnetic reconnection rate, is not uniform along flare ribbons, indicating a large inhomogeneity in the coronal magnetic reconnection. So far theoretical models mentioned above only deal with 2.5-D configurations with a translational symmetry along the axis of the arcade. Our observations show that at least in the case of the magnetic reconnection, such a translational symmetry may not exist. Taking into consideration the real 3-D configuration may result in some different theoretical arguments. Furthermore, very recently, Asai et al. (2002) found that hard X-ray sources only concentrates in some parts of Hα radiation source, where the magnetic fields, and consequently the magnetic reconnection rates, are strong. It is interesting to derive the electric fields at these locations to compare with other locations along the ribbon. It is also worthwhile to compare with other events for which the photospheric magnetic fields are more homogeneous, in order to understand what agent plays the role of controlling the magnetic reconnection rate.

CHAPTER 5

PERIODIC MOTION ALONG A SOLAR FILAMENT

5.1 Introduction

Mass motion in and around filaments (prominences), which are often visible in Hα and EUV, has attracted a great deal of attention from solar physicists, since such investigations may provide important clues to magnetohydrodynamic instability in filaments and also sheds light on the still not well understood filament formation process. Under the conventional idea, a filament should have a concave upward magnetic structure called "magnetic dip" that plays essential roles not only in providing the support of cool dense material against gravity, but also as a material reservoir and protecting the material via thermal insulation against hot corona surrounding the cool material. Specific magnetic field configurations are proposed for the magnetic dip: Kippenhahn & Schluter (1957) proposed the normal polarity dip model in which the magnetic dip field in the filament has the same direction as the underlying magnetic field; Kuperus & Raadu (1974) proposed the inverse polarity flux rope model in which the directions of the magnetic field in the filament and the underlying magnetic field are opposite. In spite of these theoretical considerations, however, such magnetic dip structures have never been directly observed (Martin & Echols 1994, Martin & McAllister 1997, Demoulin & Klein 2000).

There has been continuous efforts on observing filaments and prominences using improved Hα camera system at Big Bear Solar Observatory (BBSO). Outstanding results obtained in recent years include counter-streaming motion (Zirker et al., 1998) and periodic mass motion in quiescent filaments (Yun et al., 2001), which are interpreted under two different, confronting ideas regarding the nature of the filament.

Recently, a drift motion within filaments, in the form of counterstreaming flows, i.e., concurrent flows in opposite directions along the filament at speeds of 5–10 km s^{-1}, has

been found using off-band Hα filtergram at the BBSO (Zirker, Engvold, & Martin 1998; Martin 1998). This observation has been accepted as a crucial new result since, if cool prominence material continually forms, flows, and disappears, then stable gravitational support might not be necessary. Since mass exchange can occur through barbs (Martin et al. 1994) between its top and lower solar atmosphere, the role of magnetic dip as a material reservoir is not as essential as believed. A theoretical model for the counter-streaming flows has followed in which heating localized near the footpoints of a coronal loop can yield condensations suitable for explaining the drift motion along the magnetic loop (Antiochos & Klimchuk 1991; Dahlburg, Antiochos, & Klimchuk 1998; Antiochos et al. 1999; Mok et al. 1990). The basic cause of this dynamical process is imbalance of energy input at the footpoints, i.e., "thermal non-equilibrium" drives an intrinsically dynamic cycle of condensation formation, drift, and destruction, reproducing the observed flows (Antiochos, MacNeice, & Spicer 2000).

The periodic mass motion across a filament was, on the contrary, presented as evidence for the presence of a magnetic dip (Yun et al. 2001). In their interpretation that oscillation was due to free fall motion of cool material trapped in a magnetic dip. The observed width, tilt angle geometry are compared with a theoretical model (Choe & Lee 1992) to predict a period of oscillation under gravity, which agrees well with the observed period ($\sim$ 40 min). The magnetic field configuration that they inferred from the observation agrees to the traditional models by Kippenhahn & Schluter (1957) or Kuperus & Raadu (1974). It was however noticed that ascending and descending motions along the barbs, when viewed as projections on the disk, can also look similar to the above phenomenon. To resolve this ambiguity, Yun et al. (2001) construct a Dopplergram to find that the cool material shows blueshift reaching the maximum displacement from the main body of the prominence, whereby the hypothesis of material falling toward a barb is excluded.

On the other hand, the periodic mass motions in filaments have been known for a long time. It appears that this type motion occurs in two types: large-amplitude ($\geq$ 20 km

s^{-1}) and small-amplitude ($\leq$3 km s^{-1}) oscillations (see, for review, Oliver 1999, Oliver & Ballester 2002). Ramsey & Smith (1966) presented the first detailed study of the large-amplitude oscillatory motions in 11 filaments by using three narrow filters: one at Hα center line and two in the line wings, $\pm$0.5 Å from the line center. In their observations, an entire filament is hit, and shaken, by Moreton waves (Moreton 1960) which initiate the oscillatory motion. The resultant velocity of filament oscillation is so large ($\geq$ 20 km) that, in the course of the oscillations, the Doppler motion can even cause the wavelength emitted by the filament material to shift beyond the band pass of the filters. This effect has given rise to the term "winking filament." Physical interpretations of this winking were provided by Hyder (1966) and Kleczek & Kuperus (1969) in which a flare-produced disturbance causes a filament to freely oscillate under magnetic tension.

Extensive studies of filament oscillations have then been conducted using spectrographs to measure the temporal variation of Doppler signals, which yield, with subsequent Fourier analysis, information on the periodicity of the mass motions at the location of the filament along the slit (see, for review, Oliver & Ballester 2002). The line-of-sight velocities were found to be in the range of 1–3 km s^{-1}. The measured periods appeared in such a wide range that they could be classified as short period ($\leq$ 10 min) and long period (40–80 min) types (see, for a review, Tsubaki 1988, Schmieder 1989). A number of theoretical investigation of these small-amplitude oscillations are made employing slow, fast and Alfvén mode and further subdivision into the internal, external, and hybrid modes (see Joarder, Nakariakov, & Roberts 1997 and references therein), and also including a more complicated fibril structure (Oliver & Ballester 2002). The small amplitudes of these oscillations imply that they are locally generated by perturbations omnipresent in the photosphere and chromosphere and not related to flare activity.

It remains a mystery as to why the large-amplitude oscillations have thus far seldom been reported, since they were initially discovered almost a half century ago (see references in Ramsey & Smith 1966, Hyder 1966). In this Chapter, I present an observation of a clear

oscillatory motion persisting in a long filament as seen at the Hα line center with complete temporal and spatial coverage, and analyze the time sequence of data to determine period, velocity, and damping rate of the motion. The derived properties are then discussed in comparison of the theoretical ideas to find whether any of the theoretical ideas can be supported by observations.

5.2 The Periodic Motion

The filament discussed in this Letter appeared near the center of the solar disk on 2001 October 24 and was observed with BBSO full-disk Hα filtergrams with 1 minute cadence and a pixel size of 1 arc sec.

The filament lies between the two active regions NOAA 9672 and 9673 which is an ideal environment for the formation of long, extended and highly sheared field lines (Karpen et al. 2001). The top panel in Figure 5.1 shows a large field of view around the filament at 16:00 UT, which corresponds to south of the disk center (see the center of the solar disk marked at the upper edge of the frame). Boxes 1 and 2 are defined for close-up views displayed in the lower panels of Figure 5.1 and the upper panels of Figure 5.2, respectively. Box 3, plotted as the dashed lines, shows the extent of the oscillatory motion which occurred within the filament. The motion starts at the south-eastern footpoint and travels north-westward. The motion then reverses direction upon reaching the approximate midpoint of the filament.

The bottom three panels in Figure 5.1 are close-up views around the south-eastern footpoint where the motion initiated. Chronologically from left to right, a mini-filament can be seen in the preflare stage (17:37 UT), a subflare associated with the eruption of the mini-filament (17:45 UT) and a small two-ribbon like phenomenon caused by the subflare (17:49 UT). This is denoted a subflare because the event did cause an increase in the GOES soft X ray lightcurve, but was of insufficient magnitude to be classified as an official flare event by NOAA. Concerning the eruption and oscillation, I note the following properties.

(1) In these frames, the mass motion along the filament is not newly formed but already existed near the footpoint of the large filament before the subflare. (2) The moving material became darker, in Hα, after the eruption of the mini-filament, which is believed to be due to the squeezing of the existing material rather than the injection of new material from the mini-filament. (3) The mass motion associated with the mini-filament eruption could be traced on sixteen consecutive frames, and its mean speed is estimated as $\sim$32 km s^{-1}. This speed of mass perturbation coming from the eruption is rather low compared with that of Moreton waves, typically in order of 10^3 km s^{-1}. (4) The oscillatory motion along the large filament starts on arrival of the mass perturbation from the mini-filament eruption, which suggests that the oscillatory motion was triggered by this subflare.

The top three panels in Figure 5.2 trace out the mass motion, with arrows overlaid on the Hα frames. The position of the mass, in each subsequent image in each cycle, is determined by manually tracing the trajectory of the mass packet. The length of each arrow represents the displacement during a 5 min period. In the first cycle of the oscillation (the top-most panel) the mass moves up to the north-west and then back to the south upon reaching its maximum displacement at $\sim$18:40 UT. As mentioned above, the maximum displacement is about the mid-point of the entire filament. The second and third panels show the motions in the next two cycles in which the maximum distance travelled by the moving mass gradually decreases and, finally, stops at the midpoint of the filament. This motion is, therefore, like a damped oscillation. It is also noted that final position of the mass packet is displaced northward from its initial point, which could imply a change in magnetic structure associated with this large-amplitude oscillation.

The bottom-most panel of Figure 5.2 shows the oscillatory motion as a function of time. The cross symbols are the displacement of the moving condensation from the reference point. The time $t = 0$ is 18:00 UT, at which time the acceleration began. Note that the mass was already in motion, but at a lower speed, before the subflare (see the data points at $t < 0$) and then amplified to an oscillation with a much larger amplitude at $t \geq 0$.

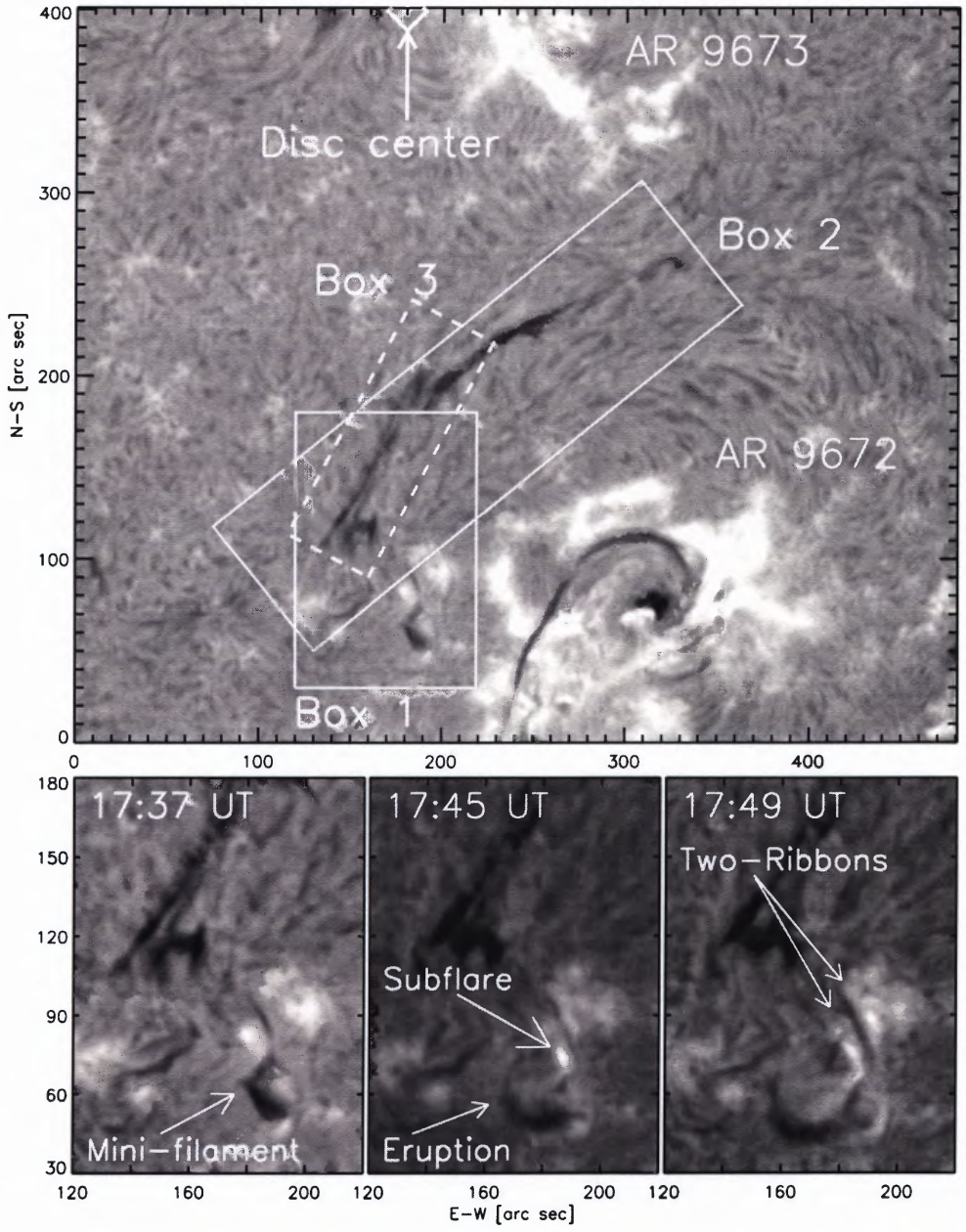

Figure 5.1 Hα images of the 2001 October 24 filament obtained at BBSO. The top panel shows a large FOV frame near the disk center at 16:01:49 UT. The solar disk center is indicated by a symbol and an arrow. Box 1 is defined for the close-up images in the bottom three panels in this figure, and Box 2 is used in the upper panels in Figure 2. Box 3 is drawn to mark the maximum range of the oscillatory motion. The bottom three panels are frames at selected times before the large amplitude oscillation began at 18:00 UT. A mini-filament, its eruption and the triggering subflare with small two-ribbons are indicated with arrows.

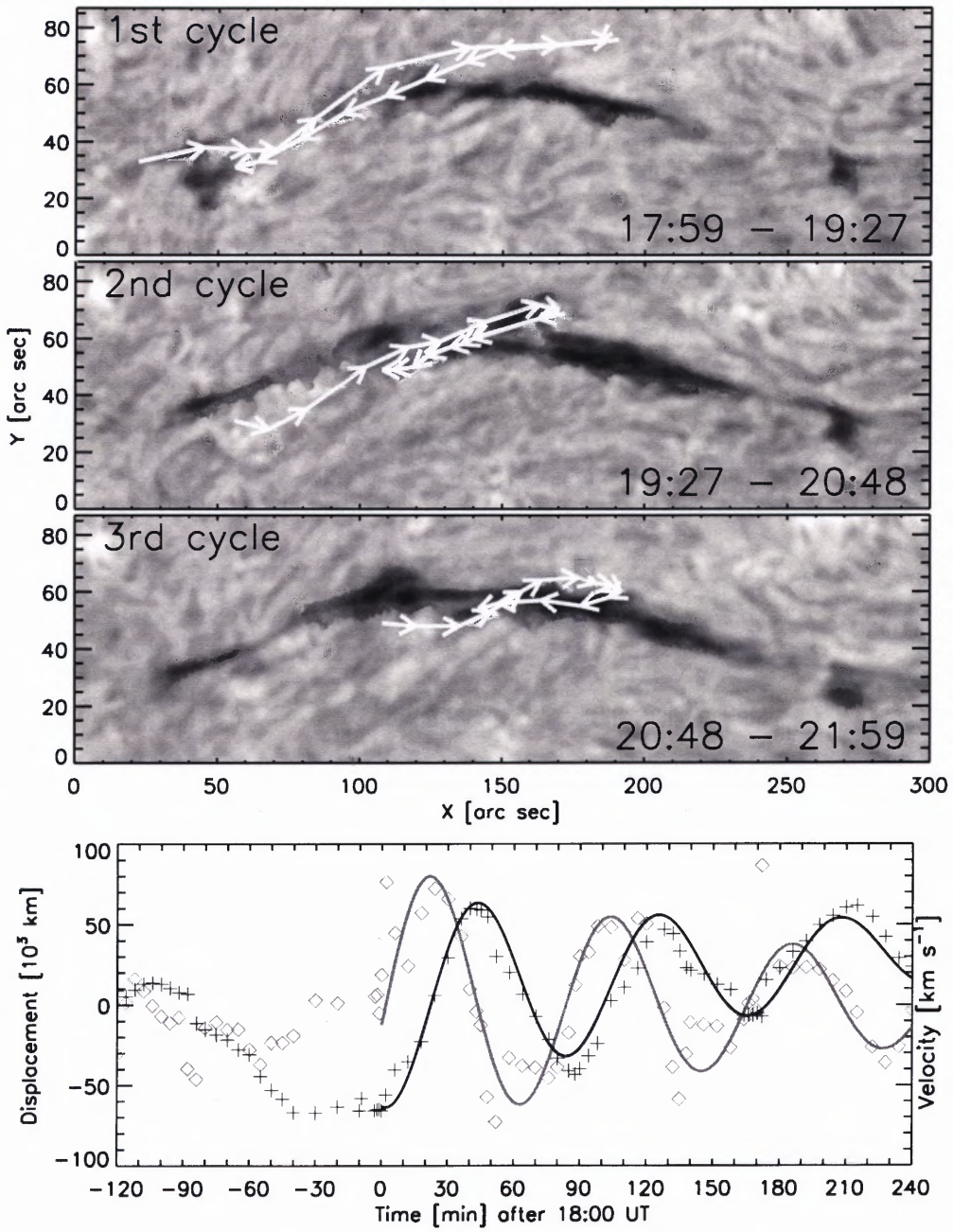

Figure 5.2 The periodic motion along the filament. The upper three panels show the motion of the moving condensation, in time intervals of 5 min, during three consecutive cycles. The Hα images, used as backgrounds, are from the middle of each cycle and were obtained at 18:00 UT, 20:08 UT and 21:34 UT, respectively. The bottom-most panel shows the measured position (cross symbols) and velocity (diamond symbols).The solid lines are fits to a damped simple harmonic oscillation. The best fit is made with an oscillation period of 80 min and a damping timescale of 210 min. The maximum displacement is $\sim 1.4 \times 10^4$ km and the maximum velocity amplitude is ~ 92 km s^{-1}. The scales for the velocity axis is the same as that for the displacement axis, which is thus omitted.

The solid line is a fit to the data points in a form of $d(t) = d_0 \cos[2\pi t/T] \exp[-t/\tau]$ plus some bias motion. The bias motion is northward and has linear trend of $\sim$3.25 km s^{-1}. The best fit parameters are: amplitude $d_0 \approx 7.0 \times 10^4$ km, oscillation period $T \approx 80$ min and damping timescale $\tau \approx 210$ min. The corresponding velocities are derived by numerically differentiating the measured positions with respect to time, and are shown as diamond symbols. The gray curve is a fit of the velocities to a sine function. The maximum velocity is $v_0 = 2\pi d_0/T \approx 92$ km s^{-1}. The ratio of damping to oscillation period is $\tau/T \approx 2.6$ while Kleczek & Kuperus (1969) found this ratio in the range of 2–3 for the 1960 June 25 event of large-amplitude oscillation.

5.3 Discussion

This periodic motion along the filament, which was discovered from the high resolution Hα images of BBSO, is distinct from other motions ever reported of filament observations. With a velocity amplitude of $\sim$ 92 km s^{-1}, this event should be classified as a large-amplitude event as defined. However, the above-mentioned large-amplitude oscillation observed with the Dopplergram was across the filament, whereas the observed motion is along the filament. These two types of oscillations could, therefore, be different in nature.

The obvious questions arising from this observation are: what mechanism can drive such a high speed motion ($\approx$ 92 km s^{-1}) over a global scale ($2d_0 \approx 1.4 \times 10^5$ km) and which process causes the damping on the time scale of $\sim$210 min.

As for the driving mechanism, it can generally consider the gravitational force, pressure imbalance, and magnetic tension that are present in the solar atmosphere. For the gravity to cause an oscillation of mass, there should be a concave upward magnetic field (also called a magnetic 'dip') within the filament. Although I cannot directly tell the presence of such a dip because of its location near disk center, I can estimate the depth of the magnetic dip required to explain the observed maximum speed solely under gravity as $v_0^2/2g \approx 1.5 \times 10^4$ km, where $g = 0.274$ km s^{-1} is solar gravitational constant. Interpreting

that the oscillatory motion shown in Figure 2 is exactly along the magnetic field lines, this implies a geometry in which the field lines have a dip with depth about 10% of its whole length. Such magnetic geometry seems plausible in view of numerous simulations made so far for the magnetic dip (e.g., Mackay, Longbottom, & Priest 1999). Furthermore, the fact that the oscillatory motion initiated at one end of the filament and came to a stop at the mid point of the whole interval of oscillation seems to favor this hypothesis.

The second possibility is considered that the observed motion is due to a pressure-driven motion, i.e., a siphon-like mechanism (Pikel'ner 1971). First of all, the observed motion apparently looks like a longitudinal (field-aligned) drift when considering the displacement of the oscillation is as large as 10^5 km. Furthermore the triggering event, the subflare, is located near a footpoint of the filament. It is thus presumable that the pressure imbalance caused by the subflare drives mass motions along field lines.

A similar picture has recently been presented in the models which successfully explain the counter-streaming flow as a drift motion driven by the unbalanced heat flux from two footpoints (Antiochos, MacNeice, & Spicer 2000, hereafter AMS). An analogy is then that in this case, the subflare provides a strong heat flux from a footpoint so that the observed drift motion can result in an extreme form of counter-streaming flow. The AMS model also predicts a damped oscillation as the condensation moves around the equilibrium point, under the restoring force perhaps provided by the pressure difference around the condensation. In this case, the radiative damping time can also be long $\sim 10^4$ s, which is similar to the damping time found in the present observation. There is indeed a remarkable similarity between the bottom panel of Figure 2 in this Chapter and Figures 2 and 3 in AMS, both of which show damped oscillatory motion as a function of time. In spite of these qualitative agreements, there are also obvious discrepancies. First, the observed oscillation is over a large portion of the filament, about half of the entire length, whereas the oscillatory motion shown in the AMS model is confined within a small section of the loop. Second, in our observation, the slowly moving condensation already exists and is subsequently

amplified by an external event, whereas the AMS model predicts the formation, drift and damping of the condensation in one dynamic cycle. Third, the AMS model assumes steady heating, while the heating is considered impulsive in our event. Therefore, a siphon-like mechanism generally lacks a restoring force needed for explaining this large-amplitude oscillatory motion as observed.

Finally the restoring force due to magnetic tension is considered. While this hypothesis is obvious for large-amplitude oscillations initiated by Moreton waves which impact a filament from the side (Hyder 1966, Kleczek & Kuperus 1969), it is dubious in this case because both the observed motion and the filament are apparently along the local magnetic field. As a possibility, consider that the field-aligned motion may occur when a large-scale Alfvén wave packet containing condensed material squeezes the field line. This scenario requires that the Alfvén wave packet should efficiently be reflected near the footpoints and carry sufficient amount of energy to overcome the gravity. It should also be noted that the filament could be composed of many unresolved, thin loops (prominence fibrils) stacked horizontally with some finite angles to the filament axis, as sometimes observed through high resolution observations (Engvold 2001). Each fibril is presumably composed of an upper part filled with cool dense material and a lower part which is highly evacuated (e.g. Yi & Engvold 1991). In this configuration, the disturbance propagating from the subflare may excite a *transversal* oscillation of the nearest fibril, which subsequently activates the next fibrils. Thus, the propagation of successive compression from one fibril to the next may apparently look like a *longitudinal* motion of condensed material. To produce the apparent motion, it should be fast mode waves propagating at a small angle with respect to the magnetic field. With this scenario, however, it is difficult to explain why the velocity of the mass motion takes the maximum near the prominence axis.

Another property which may deserve attention is the northward drift motion of the mass in addition to the east-west oscillation. That the returning flow of the mass is displaced away from the initial position might indicate that a modification of the magnetic

structure has taken place. This modification could be merely due to change in mass distribution over different field lines caused by possible drainage and supply of mass through the chromosphere. Alternatively, the impact of the perturbation might have caused reconnection between fibrils, which induces a partial magnetic restructuration. In this case, a plasma element may go along one flux tube and come back along a different one finding an equilibrium position at another place. This reconnection can generate a field line kink, which may provide some restoring force.

As for the damping of filament oscillations, radiative damping has commonly been considered (e.g., Terradas et al. 2001). If the oscillation is entirely local inside a chromosphere-like medium, the radiative damping timescale should be as short as 1–2 min. A longer radiative damping time, comparable to the value found in this case ($\sim$ 210 min) may result in a case where the medium surrounding the filament material is of a coronal temperature (cf. Antiochos et al. 2000). Kleczek & Kuperus (1969) considered that the transversal oscillation of a filament radiates compressional waves into the surrounding corona, which reacts on the filament to dissipate the power of the oscillations. Their theory predicts a specific relationship between the period and the ratio of the damping to period in a way that the damping per period increases with period and the proportionate constant between this two quantities decreases with the length of filament (see their Figure 3). The presently observed damping per period $\approx$ 2.3 follows, together with their values found for another event, this trend and lies in the range of their prediction.

As a comparison to the 'winking' filaments, an apparent difference lies in that the present large-amplitude oscillation is triggered by a subflare at one end of the filament, whereas the winking filaments are activated by Moreton waves impinging on their sides. This geometrical difference may, however, be non-essential, provided that the yet unconfirmed complexity of the internal fibril structure is postulated. The perturbation from the subflare is rather slow at $\sim$32 km s^{-1}, and therefore of chromospheric origin, unlike Moreton waves. A much higher speed of oscillation ($\sim$92 km s^{-1}) is found in the present event

than those reported for the 'winking' filaments by Ramsey & Smith (1966). It could be that either this event was a stronger sample of the same type, or our spatial and time coverage was so complete as to fully measure the entire extent of the motion.

5.4 More Events

Besides the event discussed above, three additional events of this type during 2001 and 2002 have been studied, which clearly showed large-amplitude periodic mass motions observed by using high resolution (1 arc sec) and high cadence (1 min) full disk Hα system at BBSO. They may be under the similar physical mechanism but not the same. Figure 5.3 is Hα image of the filament on the same day as the above mentioned event, 2001 October 24. The filament stemming from NOAA AR9672 shows an oscillatory motion which is seemingly related to a C2.0 flare occured at 17:06 UT. Figure 5.4 shows a limb event that is triggered by a C4.0 flare occurred in NOAA AR9866 at 18:08 UT, 2002 March 20. It looks like the material is being ejected to a height greater than the the filament along the visible filament. This event is perhaps surge rather than the oscillatory motions and could well be explained in terms of a pressure imbalance mechanism. A rather turbulent, oscillatory motion is seen in the middle of the long filament in a quiescent region, shown in Figure 5.5, which is seemingly influenced by the activity of the nearby filament (the shorter one). There is no clear relationship with any flare around. Accordingly, Figure 5.6, 5.7, and 5.8 plot the motions as a function of time. The top panel trace out the trajectory of the moving mass. The plus symbols in the top panel are the measured positions of the moving mass from a reference point adding on a arbitrary displacement. The symbols in the middle and bottom panels are corresponding displacements and derived velocities with respect to time. The solid lines are fits to the data points, respectively.

A summary of the properties of the periodic motion is presented in Table 5.1. These four events have the following properties:

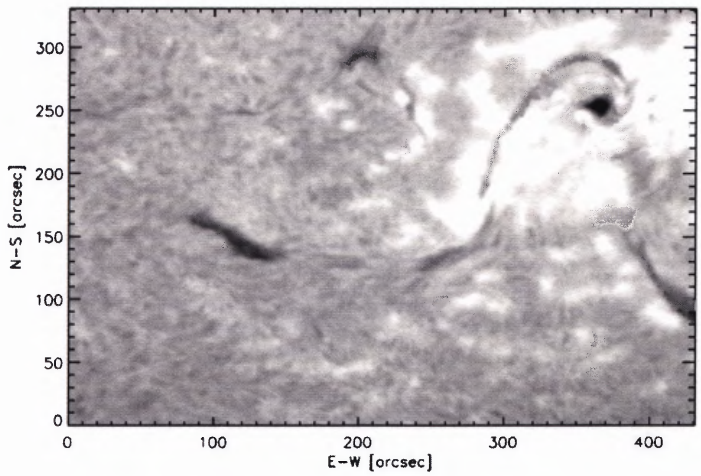

Figure 5.3 Hα image of the filament on October 24 2001. The filament stemming from NOAA AR9672 shows an oscillatory motion which is seemingly related to a C2.0 flare occured at 17:06 UT.

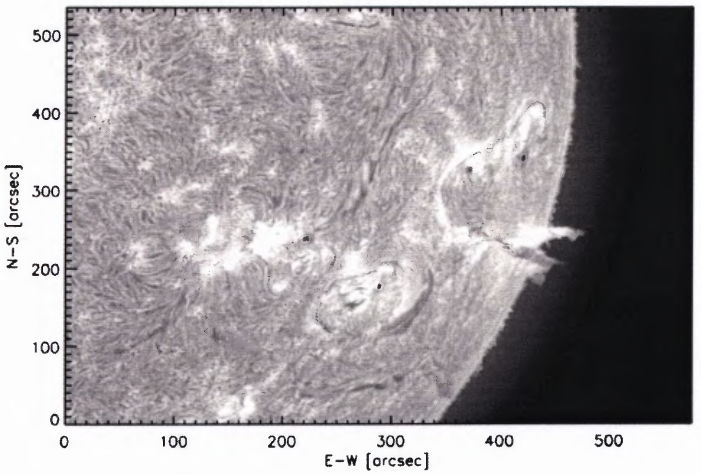

Figure 5.4 Hα image of the filament on 2002 March 20. A limb event is triggered by a C4.0 flare occurred in NOAA AR9866 at 18:08 UT

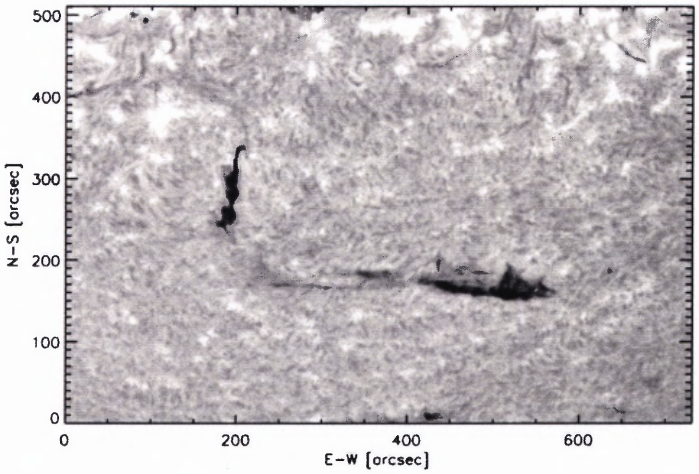

Figure 5.5 Hα image of the filament on 2002 March 22. A rather turbulent, oscillatory motion is seen in the middle of the long filament which is seemingly influenced by the activity of the nearby filament (the shorter one). There is no clear relationship with any flare/active regions around.

Table 5.1 Properties of Four Periodic Motion along Solar Filaments

Date yy/mm/dd	NOAA*	Period [min]	Length [km]	Velocity [kms^{-1}]	Damping [min]
01/10/24 A	9672-9673	80	$\pm 7 \times 10^4$	80	210
01/10/24 B	9672	160	$\pm 9 \times 10^4$	60	950
02/03/20	9866	150	$\pm 4 \times 10^4$	30	
02/03/22	QS*	104	$\pm 1 \times 10^5$	100	450

*NOAA: Active Region Number

*QS: Quiescent Area

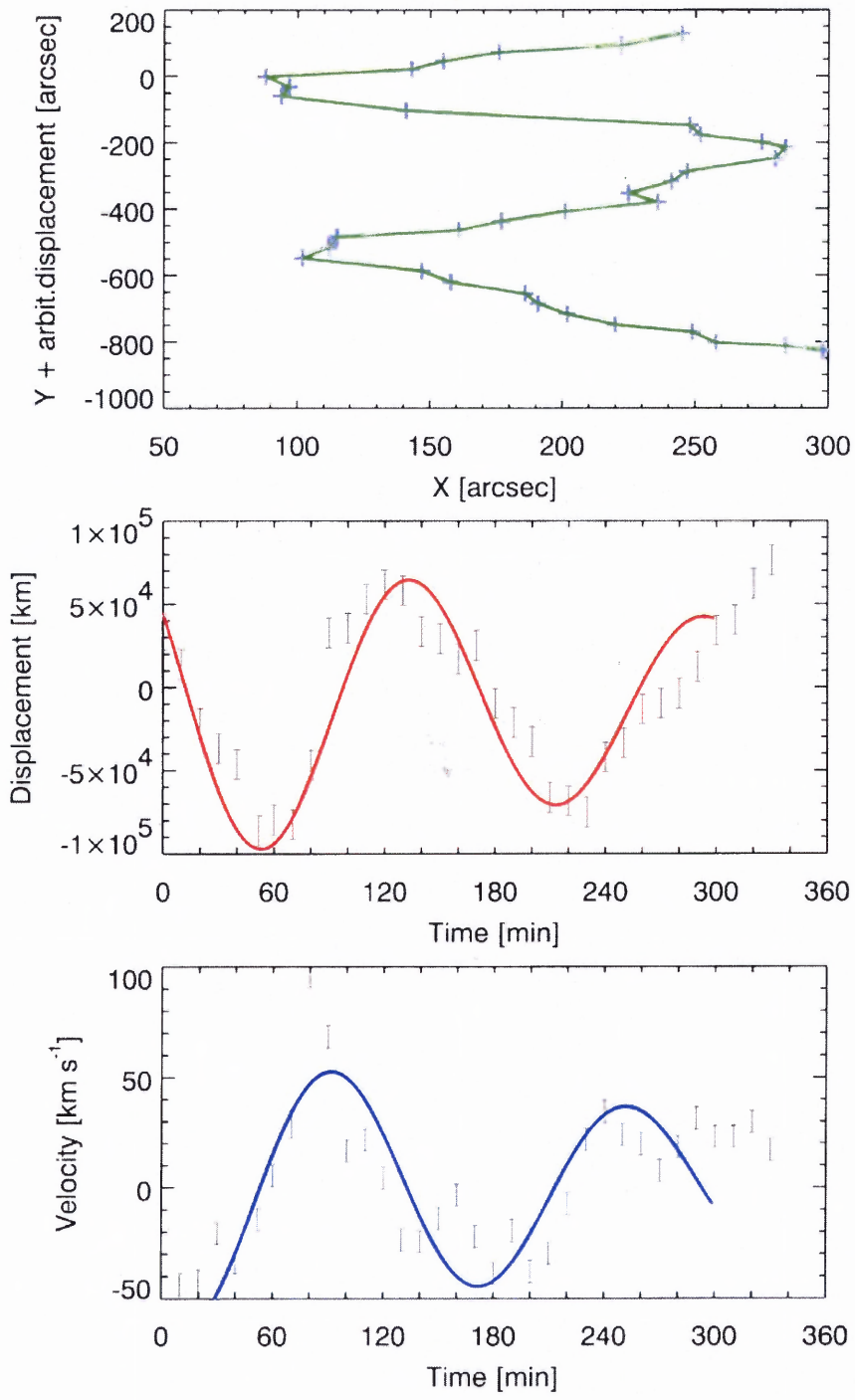

Figure 5.6 Another periodic motion of 2001 October 24. The top panel: The periodic motion over the whole cycle is shown as plus symbols, every 5 min, and arbitrary drift along the y-axis is added in order to avoid overlap of oscillatory motion at each cycle. The middle panel: the measured positions are fitted to a function of time. The bottom panel: The derived velocities are fitted to a function of time.

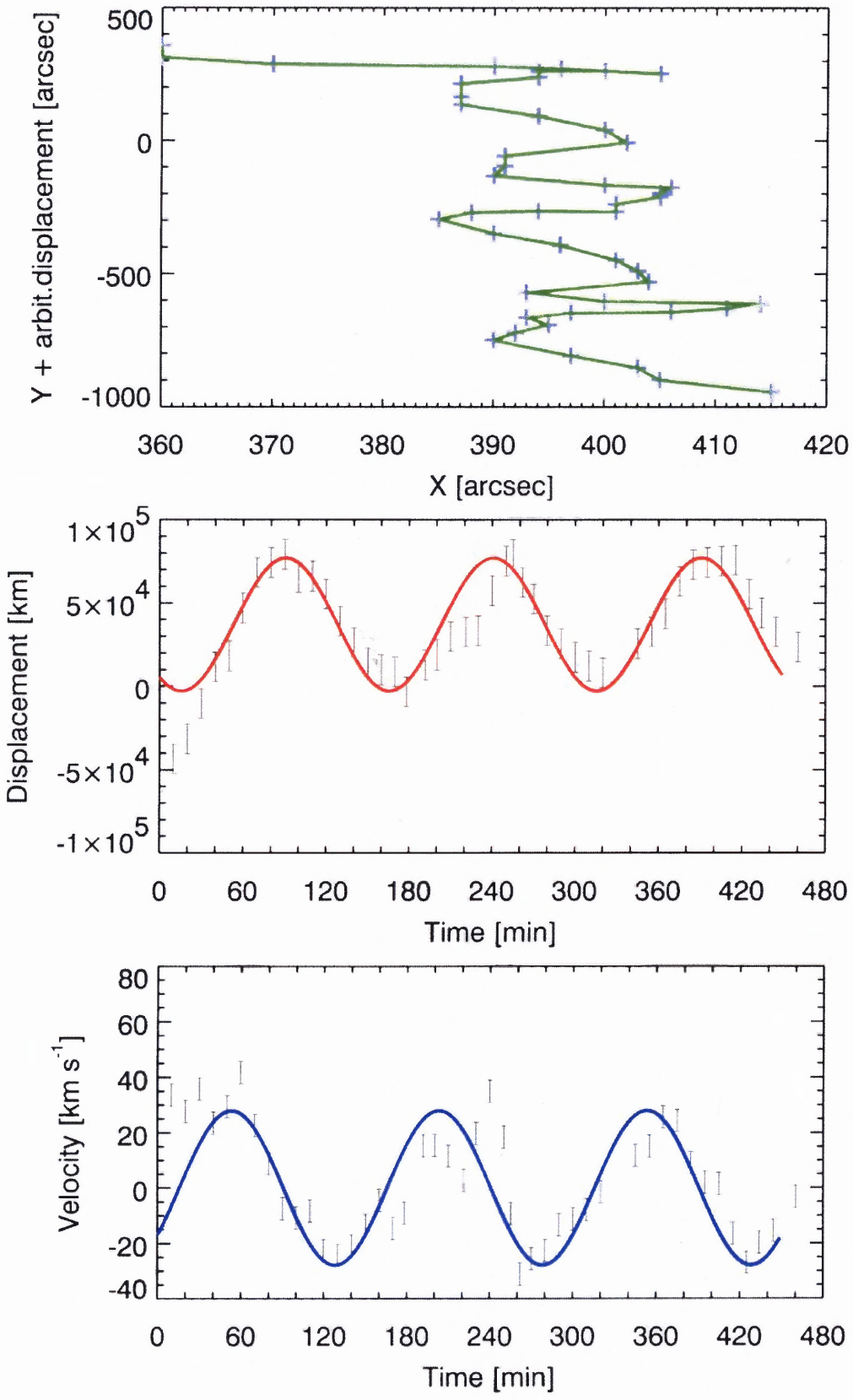

Figure 5.7 Same as Figure 5.6, but for the periodic motion of 2002 March 20.

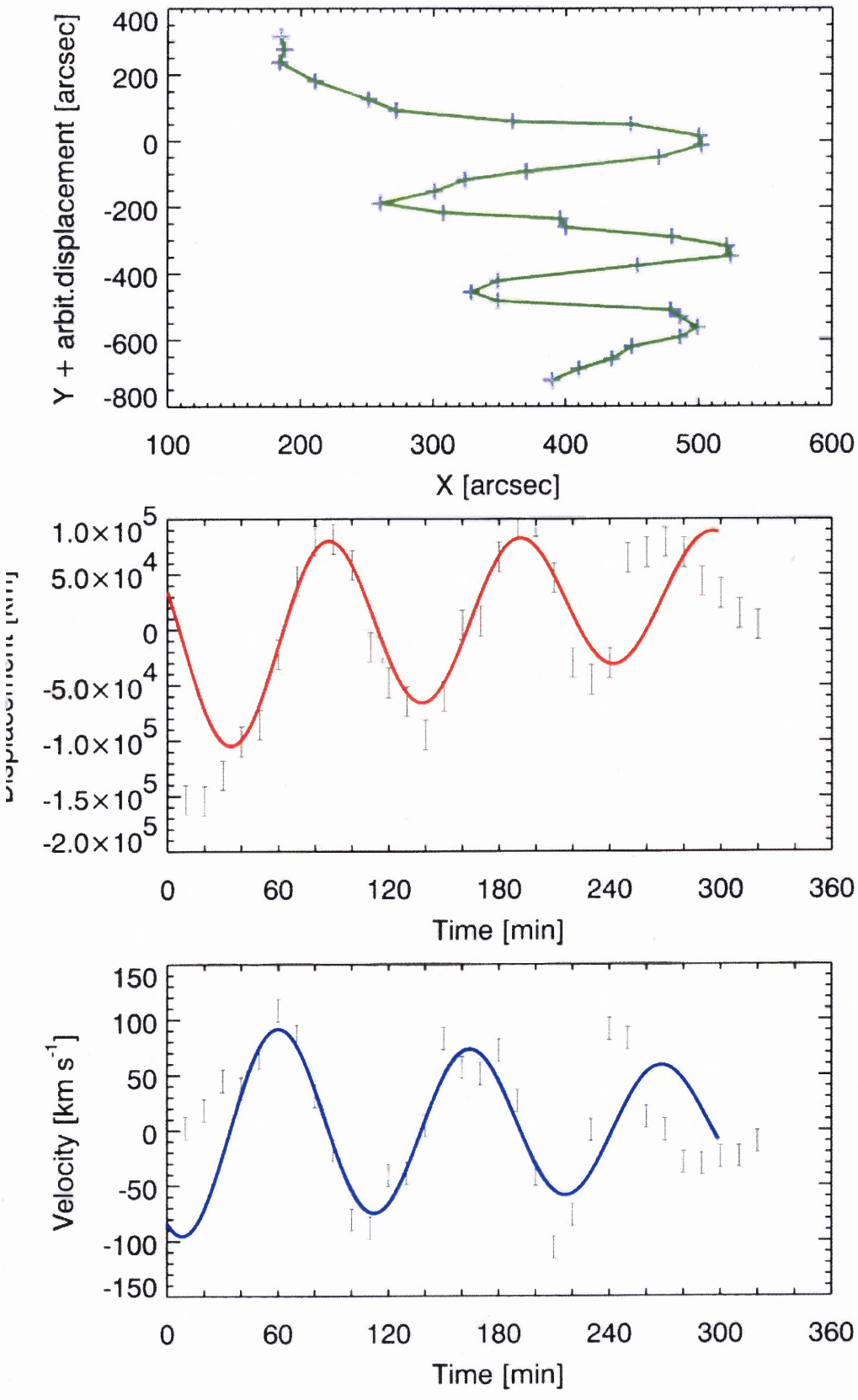

Figure 5.8 Same as Figur 5.6, but for the periodic motion of 2002 March 22.

1. long period (80 to 160 min)
2. travelling over large distances (about 10^5 km)
3. high velocity amplitudes (30 to 100 km s^{-1})
4. moderate damping (>210 min)
5. seemingly initiated by nearby flares or filament eruptions

With their speed and dimension, these large-amplitude motions represent not only the most spectacular but also the most energetic oscillatory phenomenon above the solar surface.

In summary, observations of the large-amplitude filament oscillations with improved spatial and time coverage are presented, which brings up more issues than raised with the previous observations (Ramsey & Smith 1966) and presents a new problem to be discussed in relation to the filament dynamics. Answer to the restoring force is unlikely to be found easily. At this stage, I could only discuss various possible mechanisms for the driving and damping of the motion against our observation without final conclusion. Since it appears that a proper interpretation of the restoring force and damping mechanism strongly depends on the geometry of the filament and the magnetic field, it will be important to study the 3-dimensional spatial structure of such filaments via continued high-resolution observations to further advancing our understanding of the nature of filaments.

CHAPTER 6

EVOLUTION OF TWIST OF A ERUPTIVE FILAMENT

6.1 Introduction

There is an accumulation of observational evidence over the years that the different manifestations of solar activity in the corona – filament eruptions, flares, CME onsets, – all relate into a coherent global physical process. The origin of this process must be traced to the evolution of the magnetic fields. The observations of the emergence of twisted fields and the helicity of a preferred sign in each hemisphere (Leroy 1989; Martin et al. 1993; Pevtsov et al. 1994; Rust 1994) lead naturally to the idea that twisted magnetic field may form in the corona and manifested itself in many features. The twisted, helical-like structure are more frequent in active region prominences, but sometimes can be found also in quiescent prominences, especially clear when they erupt (Rompolt, 1975, 1988,1990; House & Berger 1987; Vršnak et al 1988, 1990;).

There has been continuous efforts on understanding the role of twisted flux rope in the process of the eruptive events. Observationally, in particular, Vrsnak et al. (1991) investigated internal structure of 28 prominences and found that eruptive prominences show higher observed twist than quiet ones. More recently, Nindos & Andrews (2004) studied 133 active regions and found that coronal helicity of the active regions that produce CME-associated flares is generally larger than those of active regions producing flares without CMEs. On the other hand, theoretical models for the filament or CME have been developed to take into account the effect of the twist. In these models, the filament is regarded as a twisted magnetic flux tube for simplicity. The basic cause of the eruption is the imbalance between the magnetic pressure gradient and the restoring magnetic tension. The maximum amount of twist for a filament to be stable are imposed by the theory (Hood & Priest 1981; Priest 1982) and confirmed by the observation (Vrsnak & Rompolt 1991).

In this chapter I report a case study of a filament eruption observed using high resolution (1 arcsec) and high cadence (1 min) Hα images obtained at KSO on July 23 2002. Hα observations of the filament reveal apparent twisted structure that correlates well with the twisted flux rope model. The basic character of the eruption appears to be the rising and expanding of the twisted structure. Particular attention is given to the evolution of the pitch and the twist of the filament. In our estimation, a rapid increase in pitch angle occurs at the pre-eruption phase whereas the twist stays constant during this course. With the above results of the twist and the equation of motion for the twisted flux rope, the filament acceleration can be evaluated and compared to the observation.

6.2 Observations

6.2.1 Hα observations

The filament discussed in this chapter appeared on the east limb on 2002 July 14, travelled across the disk, and erupted on July 23. I use BBSO and KSO full-disk Hα images, obtained over 9 days, to follow the evolution of the filament. The filament's disk-crossing and eruption permit a comprehensive view of its shape from different perspectives. Figure 6.1 shows its configuration and evolution from July 18 to July 23. The central part of the filament extends over approximately 40^o of the solar surface. A particularly good data set was obtained on July 23 from 07:10 UT to 16:11 UT. The spatial and temporal resolutions are approximately 1 $''$ and 1 min, respectively. High-resolution Hα observations of the filaments provide fine structure details. In this case, a bundle of fine structure threads in the filament can be identified. It should be noted that these threads are seen in projection on the disk plane and the observation of the fine structure is down to the limit of spatial and temporal resolution.

The evolution process of the filament follows a scenario:

1. July 14 – July 18: During this period, the filament appears near the east limb. The fil-

ament exhibits a clear shape that consists of a few, at least 4 on July 18, well-defined arches which anchored with thick legs to lower chromosphere at some separate footpoints that are almost aligned with the filament axis (see Figure 6.1a). The arches have sharp edge and narrow width (the diameter of the arch tube) in proportion to the length (the span of the arch). The threads forming at the spine of the arches are predominantly longitudinal, i.e., threads are stretched along the filament axis. Moreover, Hα movies show that the material in the filament flows along the arches without apparent transverse motion. If I treat the filament as a ideal cylinder flux tube, such a sharp and slender configuration with negligible transverse dimension and the prevailingly longitudinal mass motion lead us tend to believe that the flux rope is untwisted or very weakly twisted at this stage.

2. July 19 – July 20, The filament comes over the east limb to the disk and to the higher latitude. Meanwhile, the slender structure expands in transverse dimension. That is, besides the longitudinal component manifested by the spine of the arches, the filament exhibits apparent transverse fine structure threads suspending down from the spine to the chromosphere (see Figure 6.1b). When viewed in projection on the disk plane, these threads are orientated at some intermediate angle with respect to the filament axis. Hα movies show the continuous bi-directional mass flows along the observable longitudinal and transverse threads. It would be of interest to recall the discovery of counterstreaming flow within filaments (Zirker et al. 1998). Overall, at this stage, the filament appears to have a sheet-like geometry characterized by both vertical and horizontal fine structure threads.

3. July 21– July 23, During the disk-crossing the filament shows a continuous expansion of the width. Although I cannot state completely unambiguously due to the effect of the projection, the whole structure appears to be in a form of three arches with different height and width (see Figure 6.1c, 6.1d). One can easily perceive that the

most conspicuous and the largest arch (on the west, or right) is built from the threads packed around the filament body. The filament evolves to a more diffuse and intricate structure in which the threads are curve themselves like a coil.

Eventually, the filament erupts on July 23. Detailed erupting process is illustrated by KSO Hα images in Figure 6.2 and EIT 195$\dot{A}$ running difference images in Figure 6.3.

In the left column of Figure 6.2, two barbs are visible and the barbs are stable up to 11 UT holding the filament. The main location of the filaments (outlined by the orange lines) changes little. The major change in this period is the decrease in the interval between the vertical patterns. If we assume that the vertical intermittent structure (highlighted by the blue contours) represent the density contrast of the materials along the magnetic field, we can interpret the changes in the interval between the vertical patterns as the changes of pitch of the spiral magnetic field lines along the field axis.

In the right column of Figure 6.2, after 11 UT the filament starts to rise. Presumably only the right part is visible, and as expands the pitch decreases in fact. This is due to either coils are relaxed, or just expansion of the loop. Another noticeable change occurs in the left part of the filament. The field lines stemming from the barb 'a' expands greatly. The barb 'b' seems to be displaced, and also be lengthened and then vanishes by the time 14:27 UT. The third bard 'c' is seen until the last time and finally vanishes too when the filament fully erupted. Our measurement of this rising motion is presented in another Figure 6.6, which shows a continuous acceleration of the filament and the CME.

6.2.2 EIT Observations

Figure 6.3 gives the EIT running difference images which show the coronal emissions associated with the filament eruption. Each image is obtained by subtracting it from the previous image to enhance the faint features. As Figure 6.3b shows, at 10:13 UT, a dimming region appears and the filament starts to rise. In the sequence of Figure 6.3c to 6.3f, a

loop connecting the western footpoint of the filament and a nearby region is seen and gradually ascending. This means that the filament is situated at the western portion of a larger rising arcade and, furthermore, the ejective mass mainly originates from the western leg of the large arcade. As Rompolt (1990) pointed out that the direction of motion during an filament eruption depends on the location of the filament material within an erupting arch. As a result of the balance of velocities involved in the process in such a geometry, a part of eruptive filament material flows down, a part of material is transported to the nearby region along the arch, as well as a part of the material ejects to the upper corona. In addition, from the observation, the orientation of the erupting structure appears to change with time, from being roughly parallel to the limb at the pre-eruption phase (Figure 6.3b) to being inclined with some angle to it in the late phase of eruption (Figure 6.3f). It is generally known that filaments are located at the base of coronal arcades. The overlying arcades, such as the one shown in Figure 2g, are stretched and distended, or even opened, by the erupting flux tube. I also note that the observed overlying arcade is almost aligned with the erupting structure at its later time. This may imply a process during which the erupting flux tube aligns itself with the coronal loop.

6.2.3 LASCO C2 Observations

This filament eruption is accompanied by a CME that is first detected at 19:31 UT by LASCO C2 coronagraph. Figure 6.4 displays two LASCO C2 images taken during the CME (top two panels). The bottom-left panel shows the difference image. The bottom-right panel is the same difference image processed by edge enhancement which was described by Karovska, Blundell, & Habbal (1994). This technique computes second derivatives of the intensity throughout the image in multiple directions and assigns to each pixel the maximum of these derivatives. As a result, the locations of significant changes in the gray-scale level are emphasized. The basic structure of the CME is a roughly circular rim whose leading edge, trailing edge can be identified and are still connected with the Sun.

6.3 Data Analysis and Discussions

6.3.1 Dynamics

Figure 6.5 shows the height-time diagram of the rising motion of the filament and the associated CME. The filament heights are measured from Hα images. The height of the filament axis is measured in projection against the disk plane and the zero-height is taken at the top of the filament before the eruption. CME height-time data is provided by the LASCO web site. The velocity are derived numerically as the first derivative of corresponding height with respect to time. The filament has a initial ascending velocity of a few kms^{-1} which remains constant during the pre-eruption stage and then slowly increases to several tens of kms^{-1} with an maximum acceleration of 15 ms^{-2} during the observed eruption process.

6.3.2 Twist

Since the basic character of this erupting filament is the expansion of the twisted structure at the pre-eruption phase, it would be of physical interest to summarize the properties of the twisted structure here. On a cylindrically symmetric flux tube with longitudinal component B_l and azimuthal component B_{az} of the magnetic field line, the pitch-length λ specifies the axial length of a twisted line that encircles the axis once. It is given by $\lambda = 2\pi r B_l / B_{az}$, where r is the radius of the tube. Alternatively, the pitch-angle ϑ specifies the ratio of the azimuthal component of the magnetic field to the longitudinal component, and can be quantified by $tg\vartheta = B_{az}/B_l = 2\pi r/\lambda$. Usually, a increase of the pitch-angle suggests a "twisting" progress. More generally, according to Priest (1982), the amount by which a field line is twisted in the tube (length$l$) is:

$$\Phi = \int d\Phi = \int_0^l \frac{B_{az}}{rB_l} dl = \frac{lB_{az}}{rB_l} = \frac{ltg\vartheta}{r} = 2\pi l/\lambda \tag{6.1}$$

That is, Φ specifies the angle through which each line has been turned.

The twisted structure and measurements of the twist are schematically shown in Figure 6.6a. The twist in the flux tube can be estimated from the observations. To analyze the twist in the filament quantitatively, I choose a few images under the best seeing condition. As seen in the high resolution $H\alpha$ images, the overall structure of the filament might approximately fit into a cylindrical twisted flux tube and twisted lines in the tube could be identified and measured(e.g., see Figure 6.6b). I perform the measurement at left, right and central part of the filament, see Figure 6.6c, at several moments during the pre-eruption stage. Table 6.3.2 summarizes the measurements and the deduced values, including the length of the filament l, the radius of the tube r, the pitch-length λ, the tangent of the pitch-angle $tg\vartheta$, and the estimated twist Φ. In this event, I see a general increase in r as the filament rises whiles λ proceeds in different ways from right and left, i.e., λ increases at the right, decreases at the central and nearly stays constant at the left. The changes in pitch-lengths at different locations suggest such a redistribution of the twisted lines. As a consequence, the evolution pitch-angle displays different behavior.

To better illustrate our deduced results in Table 6.3.2, Figure 6.7 displays the temporal variation of the pitch-angle and the twist. The uncertainty of measuring the parameters r and λ is estimated to be less than 5 pixels in each image, depending on the sharpness of the fine structure while the uncertainty of measuring the length of the filament l is less than 5%. In our estimation, I see a slight decrease at the right as a consequence of that the pitch-length in this part increases faster than the radius. On the other hand, the angle rapidly increases at the central and left at a timescale of 40 min and then it nearly remains constant at the left and keeps increasing at the central. The twist shows very slight variation. Since the filament remains rooted in the chromosphere, the twist over the filament should be constant that is roughly confirmed in Figure 6.7b.

Theoretically, it has been shown that when the twist exceeds a certain amount the flux tube goes unstable and subject to the helical kink instability. The threshold of the twist for the instability ranges from 2π (Kruskal-Shaftanov limit) to 3.3π (Hood & Priest 1981).

Table 6.1 The Measured and Deduced Data

	Left Part			Central Part			Right Part				
Time [UT]	r $[Mm]$	λ $[Mm]$	$tg\theta$ $[\pi]$	r $[Mm]$	λ $[Mm]$	$tg\theta$ $[\pi]$	r $[Mm]$	λ $[Mm]$	$tg\theta$ $[\pi]$	l Mm	Φ $[\pi]$
07:24	14.5	10.9	2.7	17.8	20.3	1.8	24.0	37.0	1.3	240	21.1
07:35	12.3	10.2	2.4	19.6	18.9	2.1	25.3	45.0	1.1	236	19.1
07;51	14.8	6.5	4.6	18.1	12.3	2.9	25.0	47.9	1.0	231	20.8
08:04	17.8	8.7	4.1	21.0	11.6	3.6	23.5	54.4	0.9	236	19.0
08:16	16.7	7.3	4.6	21.8	14.5	3.0	27.2	63.1	0.9	237	16.8
09:23	19.6	8.7	4.5	21.8	16.7	2.6	30.1	68.9	0.9	247	15.7
10:08	22.1	10.9	4.1	22.1	12.3	3.6	29.0	70.3	0.8	244	15.6
11:59	25.0	11.6	4.3	22.5	9.4	4.8	31.2	66.0	0.9	262	18.0

Even if a flux tube is not subject to the kink instability, Parker (1974) points out that when the flux rope is twisted sufficiently, it becomes unstable to buckling. The condition for buckling is that the magnetic pressure due to B_{az} exceeds the magnetic tension due to B_l. Observationally, Vrsnak & Rompolt (1991) establish empirical criteria for the onset of an eruptive instability from a sample of 28 prominences. The results shows that the eruptive promineces are characterized by a pitch-angle$>$ 50°. In the present case, the amount of twist preceding the eruption is rather large, i.e., one order of magnitude larger than the theoretical limit and the pitch-angle is also larger than the empirical criteria. The filament is certainly an extremity of this type of structure.

A question arises from the observation: what mechanism causes the formation of such a highly twisted structure and the growth of the twist. A detailed analysis of the magnetic field may help to answer this question. However, the magnetograms are not really informative because the filament is located near the limb. I can only speculate that either sheared transverse magnetic field or new flux emergence or magnetic flux cancellation may cause some reconnection and, consequently, the formation of a huge, twisted erupting arch (Rompolt 1990).

6.3.3 Comparison with the Twisted Loop Model

An order-of-magnitude model for a filament or CME as a twisted flux rope was presented by Monschovias & Poland (1978). In their picture, the summit of the coronal loop has both a longitudinal field component B_l and an azimuthal field component B_{az}. The difference in magnetic pressure between the bottom and top of the loop due to B_{az} provides upward force. In the case of the constant-velocity motion, the upward force is balanced by the downward magnetic tension force and the gravity force. Under the neglect of the effect of the background corona on the loop the MHD force equation reduces to a simple form:

$$\frac{B_{az}^2}{\mu R_c} - \frac{B_l^2}{\mu R_c} - \rho g = 0 \tag{6.2}$$

where R_c is the radius of curvature of the loop, ρ is the mass density in the loop and g is the solar gravitational constant.

This model is applied to the present twisted filament structure and modified by the presence of a filament acceleration a,

$$\frac{B_{az}^2}{\mu R_c} - \frac{B_l^2}{\mu R_c} - \rho g = \rho a \tag{6.3}$$

I rewrite the above equation in the following form:

$$\frac{B_l^2}{\mu R_c}[tg^2\vartheta - 1] - \rho g = \rho a \tag{6.4}$$

Note that here the radio B_{az}/B_l is written in the tangent of the pitch angle $tg\vartheta$ which can be obtained from the observation. The above equation can be used to estimate the acceleration of the filament and make a quantitative comparison with the observation. The quantities μ and g are taken as $4\pi \times 10^7 Hm^{-1}$ and 274 ms^{-2}, respectively. The quantity R_c can be estimated from the geometry of the filament. I take it to be $7 \times 10^5 km$, comparable to the solar radii, because the spine of the filament is rather flat and nearly parallel to the solar surface. In addition, I take a typical value of the number density of the electron in the filament, $10^{18} m^{-3}$, and assume the longitudinal field strength B_l in the erupting tube is 1G (Athay & Illing 1985). With these values as well as the observed average $tg\vartheta$, I obtain an estimate of the filament acceleration of $0.1 - 0.9$ kms^{-2}, which is an order of magnitude larger than the observed acceleration.

A primary reason for the difference between the expected acceleration and the observed one is the ignorance of the effect of the background corona. The expression 6.4 is derived under the assumption that the background corona plays a minor role on the coro-

nal loop as it rises for simplicity. However, in this case, the erupting filament is initially oriented at some intermediate angle with respect to the overlying coronal arcades, as mentioned in the previous section, which might temporarily act to restrain the eruption and is expected to exert a remarkable drag on the ascending mass. The flat spine of the filament arch may be an evidence of the presence of the drag. Apparently, this simple model cannot be expected to describe such a complicated process in quantitative detail. The effect of the background corona should be included.

Based on MHD approach, Chen(1996) developed a theoretical model that can describe the essential physics of the initial eruption and the subsequent propagation. The initial structure is assumed to be a twisted magnetic flux rope with toroidal B_t (same as B_l mentioned previously) and poloidal B_p (same as B_{az}) components. The circular cavity observed in many CMEs is interpreted to be the top of a broad flux rope viewed edge-on, where the flux rope is still connected with the Sun. This model is significantly distinct from the model of Mouschovias & Poland (1978) in that the eruptive filament and the CME are treated as the trailing edge and leading edge of one flux rope respectively. Moreover, it includes a cold component in the initial flux rope, qualitatively corresponding to the filament material, and the momentum coupling of the flux rope with the ambient gas, represented by a drag term (Chen 1996). The simulation results are based on a range of initial values in a number of parameters. Besides the similarity in appearance, I note that this event has many features similar to those predicted by the model:

First, the simulation of the initial dynamics shows that the CME (leading edge) is forced ahead and the filament (trailing edge) is dragged along by the flux rope, which seems to be consistent with the observation. Second, in this model, the eruption is triggered by a rapid increase in the poloidal magnetic flux(Chen 1996; Krall & Chen 2000). In response to the increase, the overall behavior of the flux rope is to expand slowly as the apex rises, which is also consistent with the observation. Another attractive point of the Chen's model is that it does predict the temporal evolution of the field line twist at the apex and footpoints.

In his picture, the pitch at the apex remains nearly constant during the eruption whereas the the pitch near the footpoints increases for tens of minutes and then decreases. At any time after the the initial eruption, the pitch at apex is larger than that at footpoints, implying the field lines are more twisted near the apex. The overall tendency of the twist is a decrease.

To summarize, a highly twisted helical-like structure ($\sim 20\pi$) is found in an quiescent filament and seems to be an extreme case of this type structure which has not been discussed before. Because of its apparent similarity with the twisted loop model, it is of particular interest to test whether the observed dynamics are explicable under the theoretical model. To follow the Monschovias & Poland model (1978), the rising motion is mostly due to the unbalance of the upward magnetic pressure gradient and the downward restoring tension. However, the quantitative comparison between theory and the observation shows a large difference, i.e., the observed acceleration is 1 order of magnitudes less than the predicted one. This tells us that there is one important elements is missing such as the drag force exerted by the overlying coronal arcades. The theoretical model of erupting magnetic flux rope, presented by Chen(1996), is also considered. In this model, the flux ripe eruption is driven by a increase in poloidal flux. The observed behaviors of the motion are in good agreement with those predicted by Chen's model. Therefore, the variation of the pitch over the filament might be a consequence of the flux injection.

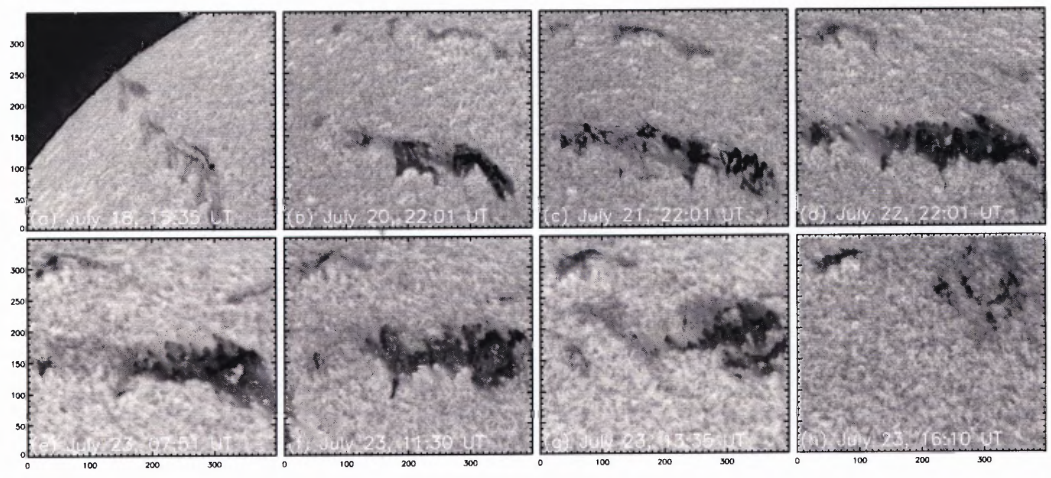

Figure 6.1 Sequence of Hα images showing the configuration and evolution of the filament from 2002 July 18 to July 23. The upper images are obtained at BBSO while the lower images are obtained at KSO. 1 pixel=1 arc sec.

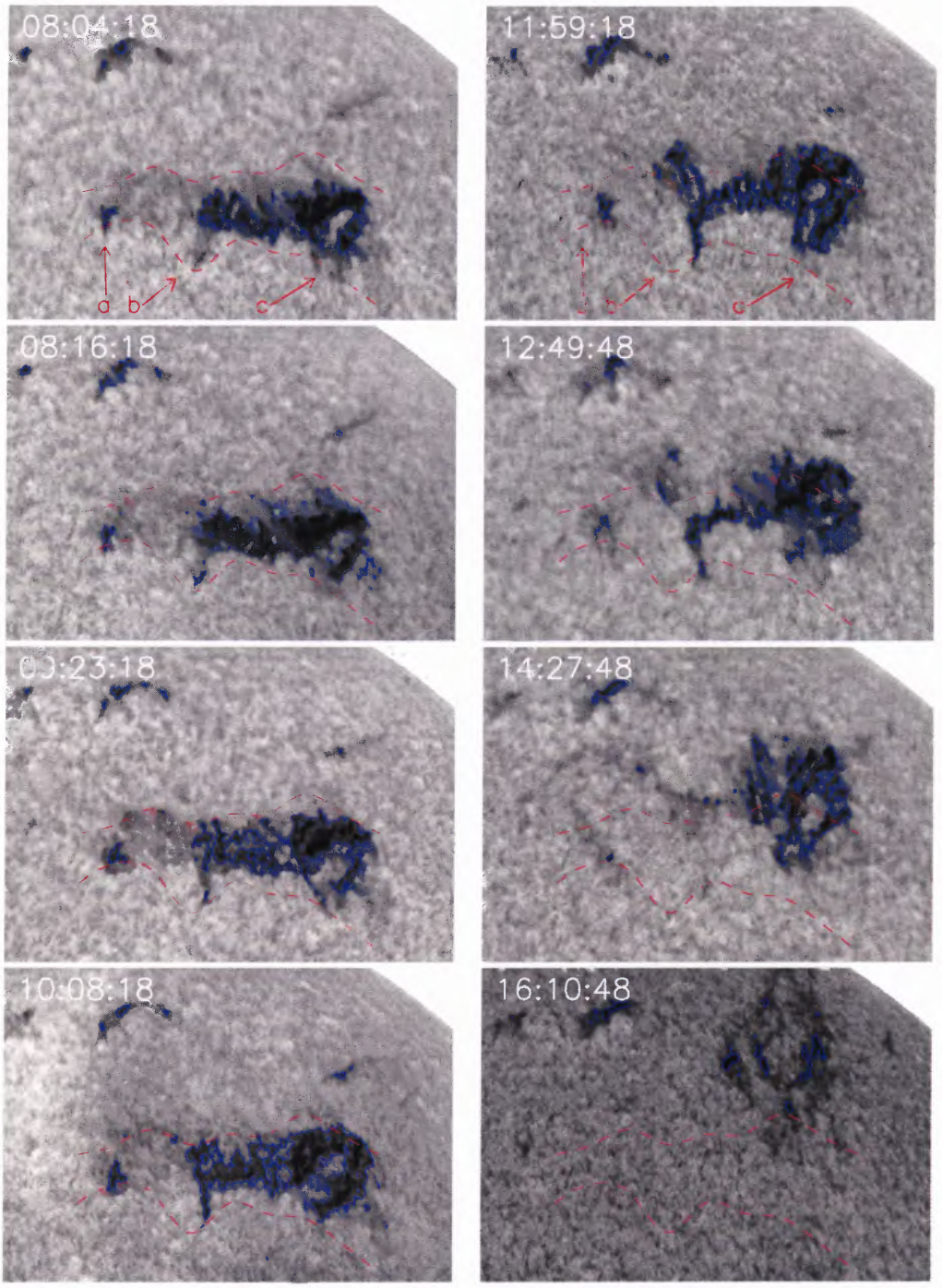

Figure 6.2 Sequence of Hα images showing the evolution of the filament prior to eruption on 2002 July 23. The solar north-west limb is partly seen in the upper right corner. The blue contours are drawn to highlight the dark materials within the filaments, and the dashed orange lines outline the filament body at the starting time 08:04 UT taken as reference. The three arrows indicate barbs observed around the filament. Images are obtained at KSO. 1 pixel=1 arc sec.

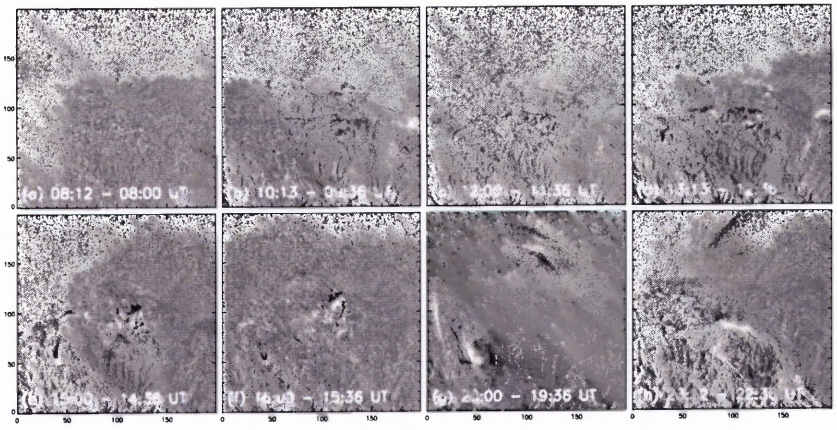

Figure 6.3 Sequence of EIT 195*Å* running difference images showing the filament eruption. 1 pixel = 2.62 arc sec.

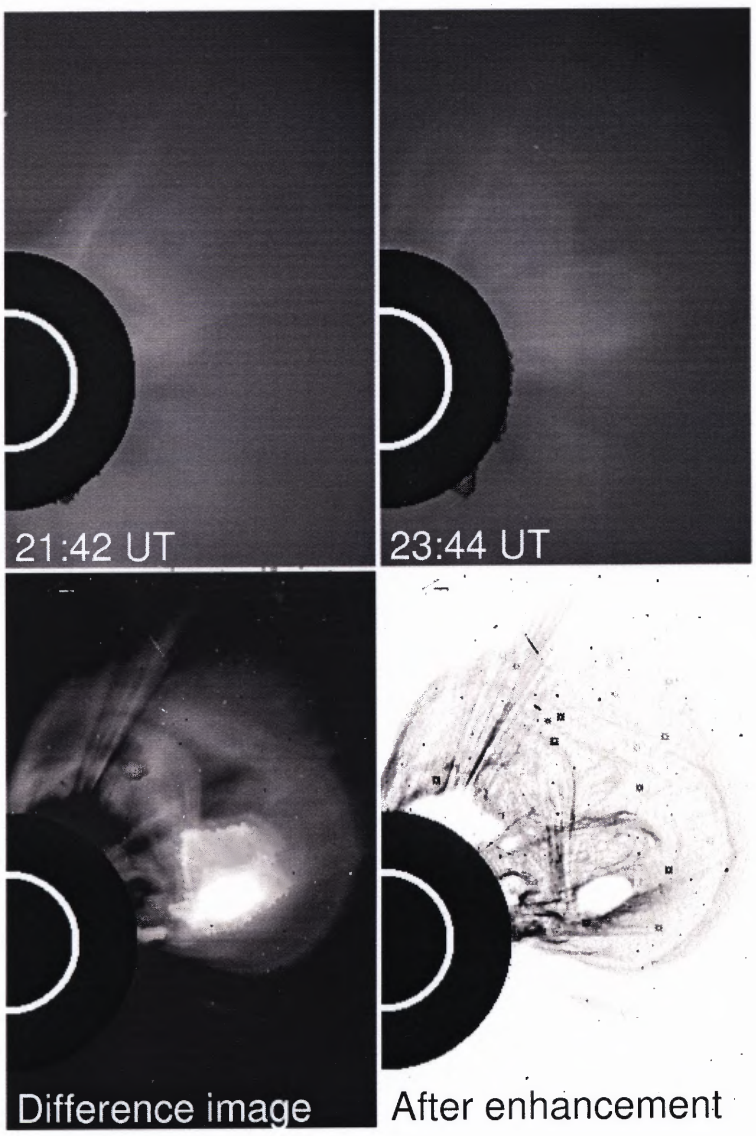

Figure 6.4 Top two panels: LASCO C2 images of the CME of 2002 July 23; Bottom left panel: difference image; Bottom right panel: processed by edge-enhancement techniques.

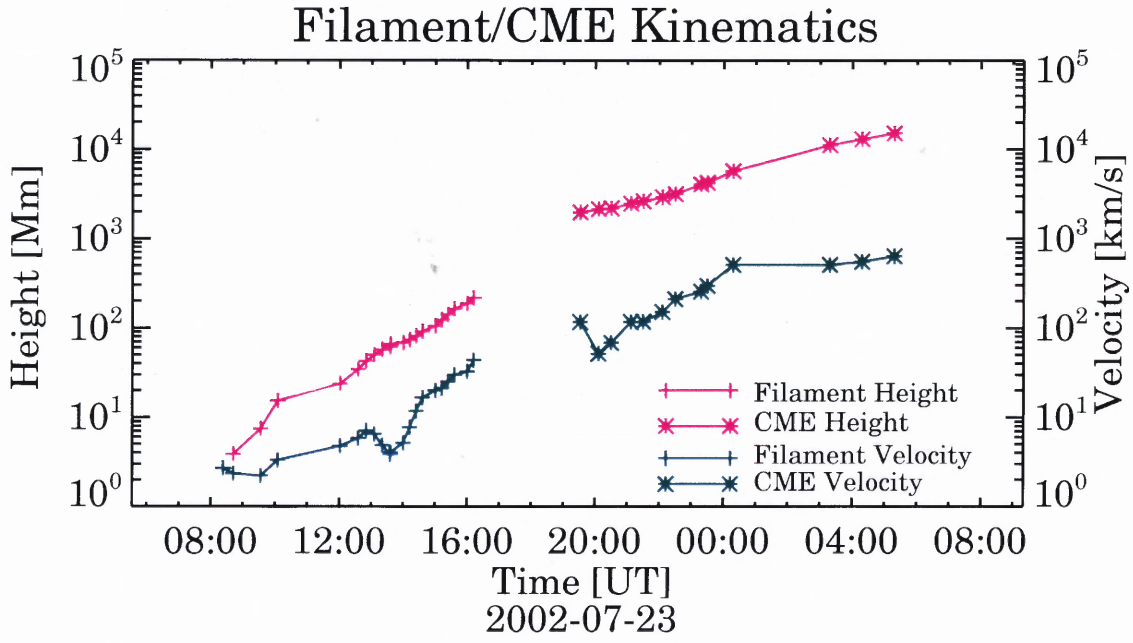

Figure 6.5 Measured height and deduced velocities of the filament and CME.

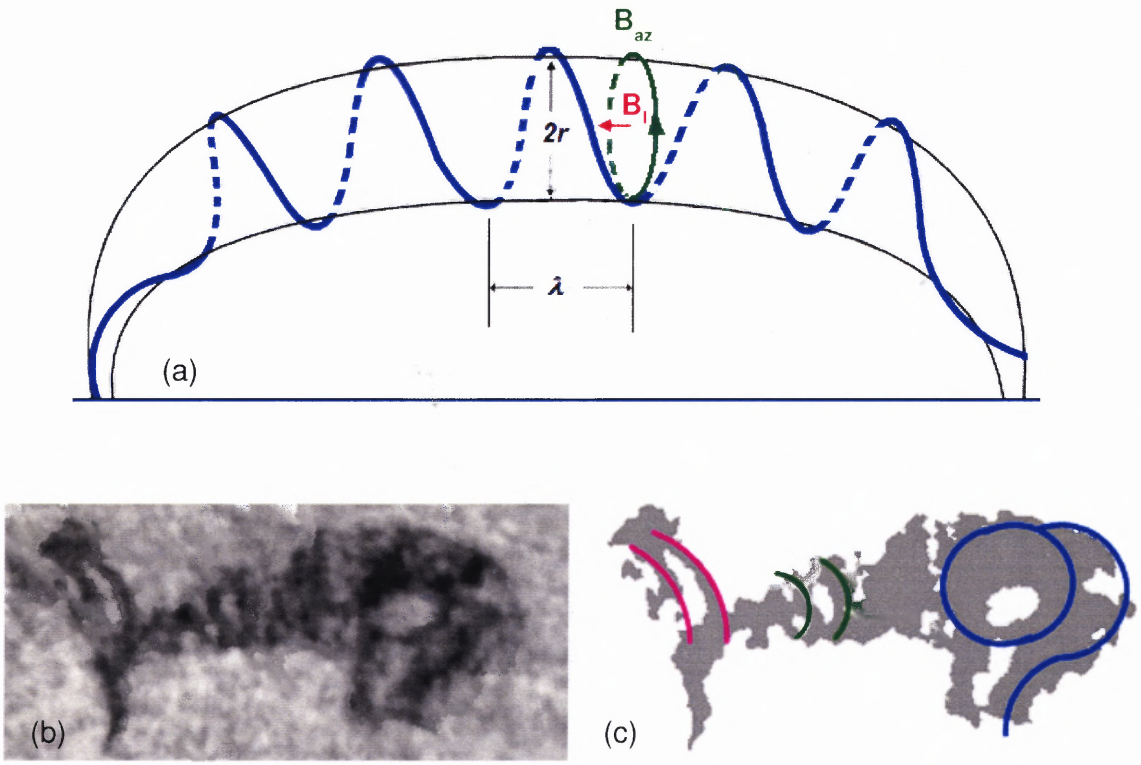

Figure 6.6 (a) A schematic drawing of the twisted flux rope. The symbols are explained in the text; (b) Hα image of the filament; (c) Curves are drawn overlaid on the Hα frame to mark the identified twist structure at three parts.

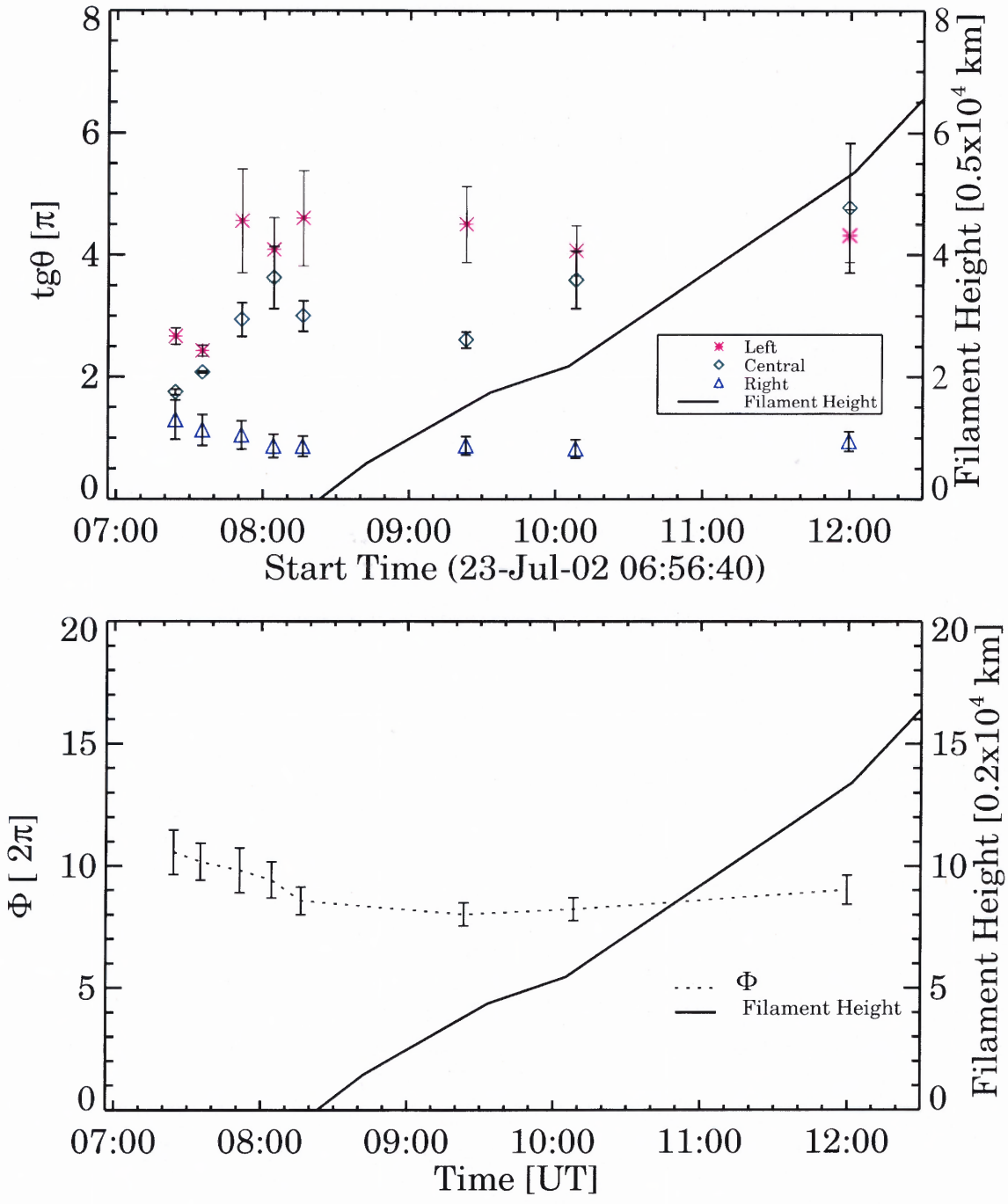

Figure 6.7 Temporal variation of the filament height, $tg\vartheta$ and ϕ.

CHAPTER 7

TWIST PARAMETER OF ACTIVE REGIONS AND SOLAR ERUPTIONS

7.1 Introduction

Magnetic helicity, generated by differential rotation and the convective flows, describes the topological complexity of a magnetic field (Moffatt & Ricca 1992; Ricca & Berger 1996). The study of helicity has attracted a great deal of attention from solar physicists since it is relevant to both the solar interior and space weather and may improve the understanding of some questions, e.g., how magnetic helicity is related to filament eruption, flares and CMEs. Although the helicity may be conserved on a global scale, it could be redistributed locally through magnetic reconnection. Such redistribution of helicity may play an important role in the build-up of the twist, the loss of the equilibrium of magnetic field, and therefore the eruption of the flux tube. The helicity of a filament arises from the twist of internal field lines about the filament axis (Berger & Field 1984). Due to its close relevance to the helicity, the quantity twist may be important to the dynamics of helicity-carrying magnetic flux tube.

Theoretical arguments concentrate on the causality between the magnetic twist and the solar eruption. That is, whether twisted flux ropes are necessary for the initiation of a CME (Low & Smith 1993; Low 1994; Amari et al. 2000,2003), or they occur as a consequence of the solar eruption and the reconnection (Antiochos et al. 1999). To deal with this question requires the consideration of whether the energy for the CME-flare process is stored and supplied by the magnetic twist in the pre-eruption corona.

In the previous Chapter, the evolution of twist in an eruptive filament eruption is studied and tried to reconcile with the twisted flux loop model. Although the simple model cannot be expected to describe such a complicated process in quantitative detail, it does outline the basic fundamental physical processes. This twisted model together with the

estimates of the field in twist can also be used to empirically evaluate the energy decrease during a solar eruption (Moore 1988). According to Moore(1988), the estimated decrease in magnetic energy is of order of the total energy released in the flare and/or CME. This suggests that the magnetic energy dumped in a filament-eruption flares comes from the eruptions of twisted flux tube, and further, leads us conjecture that the eruptive filaments with higher twist will show higher acceleration (see Equation 4.3 in the previous Chapter). In order to test the theoretical idea from observations, we will attempt to relate the magnitude of the magnetic twist to some deduced properties of the solar eruption, i.e, CME acceleration and magnetic reconnection rate. We expect such study would shed light on the still not well understood physical picture. This is the primary motivation in this study.

7.2 Measure of the Twist Parameter α

7.2.1 Linear Force-Free Field

The interpretation of the observed twist in the filament is based on the assumption of a MHD frozen-in condition. Coronal magnetic field is not yet observationally accessible. Therefore, in order to extrapolate the magnetic field in the chromosphere and the corona using the measured photospheric magnetic field as boundary conditions, some assumptions about the physical state of the coronal magnetic field have to be introduced.

The simplest assumption of the coronal magnetic field is that the magnetic field is current-free (i.e., potential magnetic field):

$$\nabla \times B = 0 \tag{7.1}$$

In this case, magnetic field is the state of minimum magnetic energy for the given boundary (Margenau & Murphy 1956) and its energy cannot be released to the solar atmosphere. This approximation is not appropriate to the active regions and flares because a number of studies suggested that the energy can be stored and librated in the magnetic configuration.

Moreover, it is found that the sites of flare emissions are cospatial with the sites of the vertical current(Hagyard et al. 1984b; Lin & Gaizauskas 1987; Wang et al. 1994; Zhang & Bao 1999).

Therefore, we consider a more general case of the magnetic field, force-free magnetic field:

$$\bigtriangledown \times B = \alpha(r)B \tag{7.2}$$

In the chormosphere and lower corona, where the magnetic field is so strong that the forces due to gravity and gas pressure are insignificant compared to the magnetic pressures, the force-free assumption is reasonable. The choice of the function α(r) is not completely arbitrary, because it must satisfy the divergence-free Maxwell equation $\nabla \cdot \mathbf{B} = 0$, and the vector identity $\nabla \cdot (\nabla \times \mathbf{B}) = 0$. These two conditions yield

$$\nabla \cdot (\nabla \times \mathbf{B}) = \nabla \cdot (\alpha \mathbf{B}) = \alpha(\nabla \cdot \mathbf{B}) + \mathbf{B} \cdot \nabla\alpha = \mathbf{B} \cdot \nabla\alpha = 0 \tag{7.3}$$

This condition is fulfilled if $\alpha(\mathbf{r})$ is constant and does not vary along a magnetic field line, so that $\nabla\alpha = 0$. This means that $\alpha(\mathbf{r})$ is not a scalar function anymore, but a simple constant, and Equation (7.2) becomes,

$$\bigtriangledown \times B = \alpha B \tag{7.4}$$

This parameter $\alpha$is commonly referred to as the "twist" parameter which is a measure of the helicity. Under the assumption of liner-force-field, α can in principle be determined by measuring the line-of-sight component of the magnetic field as well as the transverse field components. That is

$$\alpha = \frac{1}{B_z}\left(\frac{\partial B_y}{\partial x} - \frac{\partial B_x}{\partial y}\right) \tag{7.5}$$

7.2.2 Force-Free Parameter α and Helical Twist

As mentioned in previous chapter that a filament may be characterized by a twisted cylindrical flux tube. In this case, a relation between the force-free parameter α and the helical twist can be derived.

Considering a twisted cylindrical flux with the pitch-length λ and radius r. Recall that the radio of the azimuthal component of the magnetic field to the longitudinal component can be quantified by

$$tg\vartheta = \frac{B_\varphi}{B_l} = \frac{2\pi r}{\lambda} = br \tag{7.6}$$

Obviously, the magnetic components depend only on the radius r, but not on the length coordinate l or azimuth angle φ. Consequently, the general expression of $\nabla \times B$ in cylindrical coordinates,

$$\nabla \times \mathbf{B} = \left[\frac{1}{r}\frac{\partial B_l}{\partial \varphi} - \frac{\partial B_\varphi}{\partial l}, \frac{\partial B_r}{\partial z} - \frac{\partial B_z}{\partial r}, \frac{1}{r}\left(\frac{\partial}{\partial r}(rB_\varphi) - \frac{\partial B_r}{\partial \varphi}\right)\right]$$

is simplified, yielding a force-free current density j of

$$j = [j_r, j_\varphi, j_l] = \frac{1}{4\pi}(\nabla \times B) = \frac{1}{4\pi}\left[0, -\frac{\partial B_l}{\partial r}, \frac{1}{r}\left(\frac{\partial}{\partial r}(rB_\varphi)\right)\right]$$

Force-free field requires that the Lorentz force is zero, i.e., $F = j \times B = 0$. Thus a single differential equation for B_l and B_φ is obtained,

$$B_l \frac{dB_l}{dr} + B_\varphi \frac{1}{r}\frac{d}{dr}(rB_\varphi) = 0$$

By substituting $B_\varphi = brB_l$ this simplifies to

$$\frac{d}{dr}\left[(1+b^2r^2)B_l\right] = 0$$

A solution is found by making the expression inside the derivative a constant, which yields

B_l, and B_φ,

$$B = [B_r, B_\varphi, B_l] = \left[0, \frac{B_0\, br}{1+b^2r^2}, \frac{B_0}{1+b^2r^2}\right]$$

With the definition of the force-free α-parameter (Eq. 7.2) it can now verify that the α-parameter for a uniformly twisted flux tube is,

$$\alpha(r) = \frac{2b}{(1+b^2r^2)}, \qquad b = \frac{2\pi}{\lambda}$$

Making use of the Eq. 7.6 leads to

$$\alpha(r) = \frac{4\pi}{\lambda(1+tg^2\vartheta)} \tag{7.7}$$

For instance, for the twisted flux tubes studied in the previous Chapter with $\lambda \sim 2.5 \times 10^9$ cm and pitch angle $tg\vartheta \sim 3\pi$, a force-free parameter of $\alpha = 5.6 \times 10^{-11}$ cm^{-1} is obtained. This way, the geometric pitch angle ϑ, which can observationally be measured from twisted coronal loops, can be used to estimate the force-free α-parameter.

7.2.3 Reconstruction of the Magnetic Field

The constant α is commonly referred to as the "twist" parameter for magnetic fields. It is a plausible helicity proxy to characterize the twist in active region magnetic fields. It can be determined from either the vector magnetograms or the twisted fine thread structure of coronal loops. However, in most cases, observation cannot provide much information about the fine structure of the filament, and vector magnetograms observed only at a single height are often inadequate in representing coronal structures. So, numerical methods for linear force-free magnetic field extrapolation have been developed. For a given α, coronal magnetic field can be extrapolated from the boundary (i.e., photospheric magnetic field) by using either Fourier transform (Nakagawa & Raadu 1972; Alissandrakis 1981; Démoulin et al.1997; Gary 1989), Green's function (Chiu & Hilton 1977; Seehafer 1978; Semel 1988)

or a superposition of discrete flux sources (Lothian & Browning, 1995). The comparison of theoretical field extrapolations with the illuminated field lines as it can be observed in EUV can be performed. The best-fit value of α is chosen so that the computation best reproduce the observation.

Here we adopt a method for the reconstruction of the linear force-free (LFFF) magnetic field in a bounded domain which was described in Abramenko and Yurchishin (1996). If α is constant everywhere, for each field line in a given volume, the curl of the current density $(\nabla \times \mathbf{B})$,

$$\nabla \times (\nabla \times \mathbf{B}) = \nabla \times \alpha\mathbf{B} = \alpha(\nabla \times \mathbf{B}) = \alpha^2\mathbf{B}$$

On the other hand,

$$\nabla \times (\nabla \times \mathbf{B}) = \nabla(\nabla \cdot \mathbf{B}) - \nabla^2\mathbf{B}$$

Comparing these two expressions and $\nabla \cdot \mathbf{B} = 0$ lead to the Helmholtz equation,

$$\nabla^2\mathbf{B} + \alpha^2\mathbf{B} = 0$$

The algorithm is based on the solution of the Dirichlet bounary value problem to the Helmholtz equation.

7.3 Data Set

The line-of-sight photospheric magnetic field is provided by Michelson Doppler Imager (MDI) magnetograms, with the spatial resolution of 2 arcsec. At the chromospheric level, magnetic fields are revealed by the Hα chromospheric fibril patterns. At coronal level, magnetic structure is conspicuously illuminated by a pattern of coronal loops that may be observed by TRACE or YOHKOH images.

From the sample of flares studied in Chapter 2, those which originate from active regions are selected. MDI magnetograms, taken 30 min prior to the flare onset, are used as

the magnetic boundary value and progressively specify the value of α. The criteria of time is required because the helicity change rate may vary impulsively around the flare peaking time (Moon et al. 2002). For each value of α, the magnetic field on the basis of force-free field assumption are deduced, and compared the computed magnetic field lines to the observations. The best-fit value of α is selected to give the closest match to the pattern of coronal loops observe by TRACE or SXT.

This is illustrated by one example in which an X5.3 flare occurred in active region NOAA 9591 on 2001 August 25 and was accompanied by a halo CME. Figure 7.1 shows the magnetogram and the characteristics of this active region at different atmospheric levels. Specifically, the upper left panel shows the photospheric distribution of the line-of-sight magnetic field obtained by MDI magnetogram at 16:03 UT. The upper right and lower left panels show corresponding field of view BBSO Hα image at 16:04 UT and TRACE image at 195 Å at 15:35 UT. The lower right panel shows the deduced magnetic field lines, calculated with $\alpha = +0.01$, overlaid on the MDI image.

7.4 Data Analysis

Previously, we developed an image segmentation technique to derive the expansion speed of two-ribbon flares V_r and the newly brightened areas swept by flare ribbons da, automatically (for more details, see Qu et al. 2003 and 2004). From V_r and da, one may derive two forms of the magnetic reconnection rate: the electric field inside RCS, $E_{rec} = V_r B_n$, and the rate of magnetic flux participating in the reconnection, $\varphi_{rec} = \frac{\partial}{\partial t} \int B_n da$. Form a sample of thirteen well observed two-ribbon flares that are associated with filament eruptions or CMEs, the magnetic reconnection rate were derived. In addition, the velocity and acceleration of the erupted filaments and CMEs were also derived numerically as the first and second derivative of corresponding height with respect to time. Methods and results are discussed in detailed by Jing et al (2004).

On the other hand, we adopt a method for the reconstruction of the linear force-

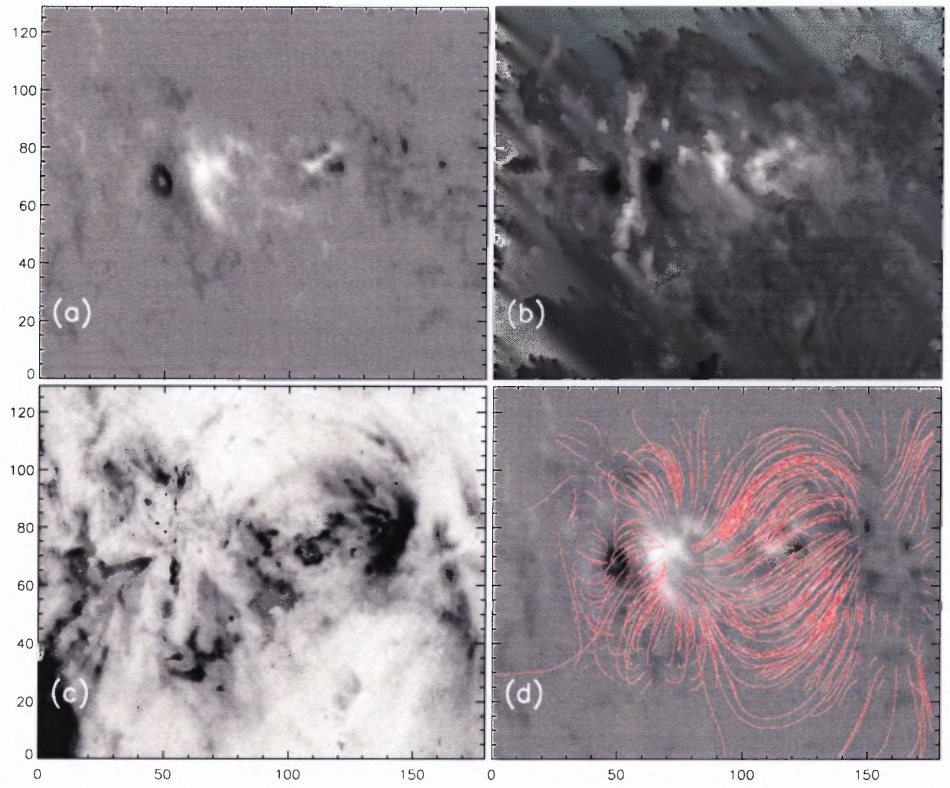

Figure 7.1 The characteristics of AR 9591 at different atmospheric levels. Upper left panel: The photospheric distribution of the line-of-sight magnetic field obtained by MDI magnetogram at 16:03 UT; Upper right panel: BBSO Hα image at 16:04 UT; Lower left panel: inversion of TRACE image at 195 Å at 15:35 UT; and Lower right panel: the deduced magnetic field lines, calculated with $\alpha = +0.01$, overlaid on the MDI image. The spatial resolution is $2''$ pixel^{-1}. The field-of-view is $360'' \times 260''$.

free (LFFF) magnetic field in a bounded domain which was described in Abramenko and Yurchishin (1996). This method allows us to specify boundary conditions not only on the "photospheric" level but also on lateral parts of the volume. The method is based on a Dirichlet boundary value problem for the Helmholtz equation with the B_z component specified at the Ω boundary. Chebyshev's iteration method with the optimal rearrangement of the iteration parameters sequence was used. The solution is obtained for positive-definite as well as non-sign-definite difference analogue of the differential operator $\nabla^2 u + \alpha^2 u$. By specifying two scalar functions B_x and B_y at the intersection of the vertical boundaries of

the Ω with one selected plane, $z = const$ and by using B_z inside the Ω, we can calculate B_x and B_y inside the Ω. The algorithm was tested with the numerical procedure, which produces an analytical solution B for a LFFF. The r.m.s. deviation of the analytical solution B from the calculated B' does not exceed 1.0%.

7.5 Preliminary Results

Currently only four events have been studied. The results are listed in Table 7.1.

The correlation between the twist and some parameters of the solar eruption, e.g., magnetic reconnection rate and flux-rope acceleration, is of special interest in this study. As twisted flux loop model suggests that the buildup of the twist may result in the loss of the stability of magnetic fields, and therefore the eruption of the filament. If it is true, it is natural to expect that the eruptive filaments with higher twist might show higher flux-rope acceleration and magnetic reconnection rate. The first event consists of a M2.5 flare with rising filament and without CME. The second and third events are composed of a X5.3 and a X5.7 flares respectively and halo CMEs but without apparent filament motion. The forth event consists of a X1.3 flares with both eruptive filament and a halo CME. Figure 7.2 displays scatter diagrams of the reconnection rate (E_{rec} and φ_{rec}) versus the twist parameter α. Based on our limited cases studied so far, there appears to be such a tendency that a flux-rope with higher twist is more likely associated with a stronger magnetic reconnection rate.

Certainly, in order to provide a statistical support of this view, a large number of events should be analyzed in the future.

Table 7.1 Data of Three Observed Eruptive Events for Best-Fit α and Solar Eruption Correlation

Date yy/mm/dd	Best-Fit α $[arcsec^{-1}]$	Max. V_n $[kms^{-1}]$	Max. E_{rec} $[Vcm^{-1}]$	Max. φ_{rec} $[10^{18}Mxs^{-1}]$	Max. $Accel_{fila.}$ $[kms^{-2}]$	Max. $Accel_{CME}$ $[kms^{-2}]$
00/02/17	+0.0075	13.0	1.4	2.3	0.3	...
00/07/14	-0.019	40.1	51.	54	...	-0.096
01/08/25	+0.01	25.8	8.9	4.9	...	0.4
03/05/27	+0.015	65.3	14.4	8.7	1.8	0.02

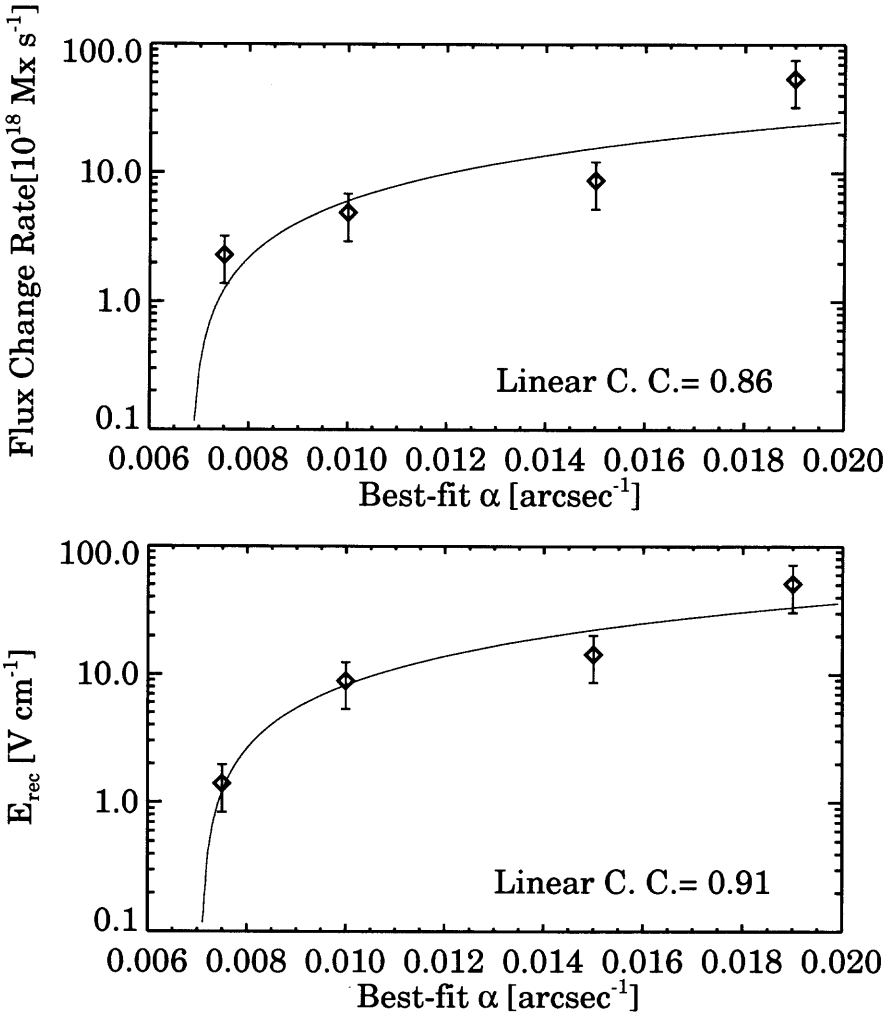

Figure 7.2 Top: Scatter diagram of maximum φ_{rec} versus best-fit α in a logarithmic scale. The solid line is a fit of data points of φ_{rec} and α in the linear form with the correlation coefficient of 0.86; Bottom: Scatter diagram of maximum E_{rec} versus best-fit α in a logarithmic scale. The solid line is a fit of data points of E_{rec} and α in the linear form with the correlation coefficient of 0.91; Error bars attached to each sign indicate the uncertainty of the measurements (see Chapter 2).

CHAPTER 8

SUMMARY

This dissertation puts together what we have learned about various phenomena of solar activities, including, in particular, erupting filaments, flares and CMEs, to synthesize the relationship linking acceleration of erupting flux rope, flare nonthermal emission, magnetic reconnection rate and magnetic twist. There are three major advances, summarized below, that are considered major breakthroughs in understanding solar eruptive events.

The first advance is the study of magnetic field change before and during the filament eruption. A filament eruption may be initiated by external events, for example the new emergence of the magnetic flux nearby; or by the loss of equilibrium in the filament itself, for example the helical instability inherent in the filament structure (Filippov 1998). We find from study of 106 filament eruptions observed from 1999 to 2003 that the majority of events are associated with new flux emergence within or adjacent to the eruptive filament. On the other hand, the filament and CME can be considered as twisted flux rope. The global magnetic helicity is expected to be conserved in the corona but the helicity locally in a arcade can be transformed into the helicity of a twisted filament through reconnection. The stability of a filament may be correlated with its helicity, or twist. In a case study, we see a rapid increase in pitch angle of the filament structure at the pre-eruption phase whereas the integral twist changes little during this course. In the statistical work we attempt to relate the magnitude of the magnetic twist to some properties of the solar eruption, i.e, CME acceleration and magnetic reconnection rate. Based on our limited cases studied so far, there appears to be such a tendency that a flux-rope with higher twist tends to relate to greater mass acceleration and magnetic reconnection rate.

The second advance is the flux rope eruption–magnetic reconnection relationship in flares. Many authors have outlined a theoretical scenario in which flares, in particular,

two-ribbon flares can be interpreted as the result of reconnection process. Erupting flux rope (filament or CME) plays the role of opening up the initially closed magnetic field. In general, the observations verify the temporal correlation between the filament acceleration and the flare nonthermal emission. Moreover, increasing reconnection rate is usually associated with an increasing filament acceleration. The correlation can fit in a linear model with high values of correlation coefficient, indicating a very strong correlation and dependable relationship between the magnetic reconnection rate and the acceleration of erupting filament. This verifies that both phenomena should be different manifestations of a single process involving magnetic reconnection.

The third advance is the relationship among magnetic structures in eruptive filaments, CMEs and interplanetary magnetic flux rope. The sign of the magnetic helicity, when combined with the one-to-one correspondence to the filament chirality, can be determined by the chirality, or handedness, of filament shown in chromosphere Hα images. Our statistics of filament chirality support earlier reports that both solar hemisphere has a predominantly distinct chirality and, therefore, sign of magnetic helicity. The sign of magnetic helicity contains important information of the surrounding magnetic field. Rust and Kumar (1994) further conjecture that the magnetic cloud field is simply the filament field which is transported through space by the eruption with magnetic helicity being conserved. If this view is correct, the helicity sign of the filament can be used to predict the orientation of the magnetic field associated with a CME, and furthermore, the likelihood of a geomagnetic storm (Yurchyshyn et al. 2000). Our investigations of the geoeffectiveness of seven eruptive filaments confirm this view. This enable us to conclude the geomagnetic storm can be forecasted on the basis of the orientation of the magnetic field of eruptive filaments and sign of magnetic helicity.

REFERENCES

Avignon, Y., Martres, M J., and Pick, M., 1964, Ann. Astrophysics, 27, 23.

Akasofu, S. I. 1981, Space Sci. Rev., 28, 121.

Amari, T., Luciani, J. F., Aly, J. J., and Tagger, M., 1996, Astrophys. J., 466, L39.

Amari, T., Luciani, J. F., Aly, J. J., Mikic, Z., and Linker, J. L., 2003, Astrophys. J., 585, 1073.

Amari, T., Luciani, J. F., Aly, J. J., Mikic, Z., and Linker, J. L., 2003, Astrophys. J., 595, 1231.

Antiochos, S. K., DeVore, C. R., and Klimchuk, J. A., 1999, Astrophys. J., 510, 485.

Antiochos, S. K., MacNeice, P. J., and Spicer, D. S. 2000, Astrophys. J., 536, 494.

Arnold, R. J. 1971, J. Geophys. Res., 76, 5189.

Aschwanden, M. J., 2004, Astrophys. J., 608, 554.

Athay, R. G., and Illing, R. M. E., 1986, J. Geophys. Res., 91, 10961.

Aulanier, G., and D'emonlin, P., 1998, A&A, 329, 1125.

Babcock, H. W. and Babcock, H. D, 1955, Astrophys. J., 121, 349.

Berger, M. A., and Field, G. B., 1984, Fluid mech., 147, 133.

Bothmer, V. and Schwenn, R. 1994, Space Sci. Rev., 70, 215.

Browing, P. K., and Priest, E. R., 1983, Astrophys. J., 266, 848.

Brueckner, G. E., and 14 co-authors, 1995, Sol. Phys., 162, 357.

Burlaga, L. F., Sittler, E., Mariani, F., and Schwenn, R. 1981, J. Geophys. Res., 86, 6673.

Cargill, P. J., 2004, Sol. Phys., 221, 135.

Cane, H. V., Richardson, I. G., and St. Cyr, O. C. 2000, Geophys. Res. Lett., 27, 3591.

Canfield, R. C., Beaujardiere, L. F., Fan, Y., Leka, K. D., et al., 1993, Astrophys. J., 411, 362.

Chae, J., Moon, Y. J., and Park, S. Y., Journal of the Korean Astronomical Society, 36, 13.

Chen,J., 1996, J. Geophys. Res., 101, 27499.

Cheng, C. Z., Ren, Y., Choe, G. S., and Moon, Y. J., 2003, Astrophys. J., 596, 1341.

Choe, G. S., and Cheng, C. Z., 2000, Astrophys. J., 541,449.

Choudhary, D. P., and Gary, G., 1999, Sol. Phys., 188, 345.

Choudhary, D. P., and Moore, R. L, 2003, Geophys. Res. Lett., 30(21), 2107.

Delaboudinière, J.-P., and 27 co-authors, 1995, Sol. Phys., 162, 291.

Denker, C., Johannesson, A., Goode, P. R., Marquette, W., Wang, H., and Zirin, H. 1998, Sol. Phys., 184, 87.

DesJardins, A. C., and Canfield, R. C., 2003, Astrophys. J., 598, 678.

Ding, M. D. et al., 2003, Astrophys. J., 598, 683.

Engvold, O. 2001, Solar Prominence Fine Structure, Encyclopedia of Astronomy and Astrophysics, Nature Publishing Group.

Falchi, A., Qiu, J., and Cauzzi, G., 1997, A&A, 328, 371.

Feynman, J. and Martin, S. F. 1995, J. Geophys. Res., 100, 3355.

Filippov, B. P, 1998, ASP Conference Series, Vol. 150, 342.

Finn, J. M., and Chen, J., 1990,Astrophys. J., 349, 345.

Fletcher,L., and Hudson, H. S., 2001, Sol. Phys., 204, 69.

Forbes, T. G., and Isenberg, P. A., 1991, Astrophys. J.,373, 294.

Forbes, T. G., 2000, J. Geophys. Res., 105, 23153.

Forbes, T. G., & Lin, J., 2000, Journal of Atmospheric and Solar-Terrestrial Physics, 62, 1499.

Forbes, T. G., and Priest, E. R., 1984, Reconnection in solar flares. In: Butler, D.M., Papadopoulus, K.(Eds), Solar Terrestrial Physics: Present and Future. NASA,pp.1-35.

Forbes, T. G., and Priest, E. R., 1986, J. Geophys. Res., 91,5579.

Forbes,T. G., and Priest,E. R., 1995, Astrophys. J., 446,337.

aizauskas, V. 1998, ASP Conference Series, 150, 257.

Gao, J., Wang, H., and Zhou, M. 2002, Sol. Phys., 205, 93.

Gary, G. A., and Moore, R. L., 2004, Astrophys. J., 611, 545.

Gilbert, H. R., Holzer, T. E., Burkepile, J. T., and Hundhausen, A. J. 2000, Astrophys. J., 537, 503.

Gonzalez, R. C., and Woods, R. E., 2002, Digital Image Processing, Prentice Hall.

Gopalswamy, N., Shimojo, M., Lu, W., Yashiro, S., Shibasaki, K., and Howard, R. A. 2003, Astrophys. J., 586, 562.

Gosling, J. T., Hildner, E., MacQueen, R. M., Munro, R. H., Poland, A. I., and Ross, C. L., 1976, Sol. Phys.48, 389.

Gosling, J. T., McComas, D. J., Phillips, J. L., and Bame, S. J. 1991, J. Geophys. Res., 96, 7831.

Hagenarr, H. J., 2001, Astrophys. J., 555, 448.

Hagyard, M. J., Moore, R. L., and Emslie, A. G. 1984, Adv. Space Res., 4, 71.

Hagyard, M. J., Teuber, D., West, E. A., and Smith, J. B. 1984, Sol. Phys., 91, 115.

Harvey, k. L., 1996, Bulletin of the American Astronomical Society, 28, 873.

Haudhausen, A. J., Coronal diagnostics, in Solar Systen Plasma Physics, edited by F.Mariani and N.F. Ness, 1997, 21-42.

Haudhausen, A. J., 1999, The many faces of the sun : A summary of the results from NASA's Solar Maximum Mission. Edited by Keith T. Strong, Julia L. R. Saba, Bernhard M. Haisch, and Joan T. Schmelz. New York : Springer, 1999., p.143

Hermans,L., and Martin, S. F., Coronal and Prominence Plasma, NASA Conference Publ. 3224, 369.

Hood, A. W., and Priest, E. R., 1981, Geophysical and Astrophysical Fluid Dynamics, vol. 17, no. 3-4, 297-318.

House, L. L., and Berger, M. A., 1987, Astrophys. J., 323, 406.

Howard, R. F., 1959, Astrophys. J., 130, 193.

Howard, R. A., Sheeley, N. R., Michels, D. J., Koomen, M. J., 1895, J. Geophys. Res., 90, 8173.

Hyder, C. L. 1966, Zeitschrift für Astrophysik, 63, 78.

Innes, D. E., et al. 2003, Sol. Phys., 217, 267.

Jahne, B., 1997, Digital Image Processing, Springer.

Ji,H., Wang, H.; Spirock, T. J., Qiu, J., Yang, G., and Goode, P. R., 2002,Sol. Phys., 211,221.

Joarder, P. S., Nakariakov, V. M., and Roberts, B. 1997, Sol. Phys., 173, 81.

Kaastra, J. S., 1985, Solar flares: An electrodynamics model. Ph.D. thesis, Astron. Dept., Rijksuniversiteit, Utrecht, Netherlands.

Karovska, M., Blundell, S. F., and Habbal, S. R., 1994, Astrophys. J., 428, 854.

Karpen, J. T., Antiochos, S. K., Hohensee, M., Klimchuk, J. A., and MacNeice, P. J. 2001, Astrophys. J., 553, L85.

Kleczek, J. and Kuperus, M. 1969, Sol. Phys., 6, 72.

Kopp, R. A., and Pneuman, G. W.,1976, Sol. Phys., 50, 85.

Kopp, R. A., and Poletto, G., 1984, Sol. Phys., 93,351.

Krall, J., Chen, J., and Santoro, R., 2000, Astrophys. J., 539, 964.

Kundu, M. R., et al. 2004, Astrophys. J., 607, 530.

Leamon, R. J., Canfield, R. C., and Pevtsov, A. A., 2002,J. Geophys. Res., 107, DOI 10.1029/2001JA000313.

Leroy, J. L., 1989, Dynamics and structure of quiescent solar prominences; Proceedings of the Workshop, Palma de Mallorca, Spain, Nov. 1987 (A89-51201 22-92). Dordrecht, Kluwer Academic Publishers, 1989, p. 77-113.

Liggett, M. and Zirin, H. 1985, Sol. Phys., 97, 51.

Lin, J., and Forbes, T. G., 2000, J. Geophys. Res., 105, 2375.

Lin, J., 2001, Ph.D. thesis, Univ. New Hampshire.

Lin, J., Forbes, T. G., and Isenberg, P. A., 2001, J. Geophys. Res., 106, 25053.

Lin, J., 2002, Chinese Journal of Astronomy and Astrophysics, 2, 539.

Lin, J., 2003, New Astronomy Reviews, 47, 53.

Lin, J., Raymond, J. C., and Van Ballegooijen A. A., 2004, Astrophys. J., 602, 422.

Lin, Y., and Gaizauskas, V., 1987, Sol. Phys., 109, 81.

Linker, J., and Mikić, Z., 1994, ASPC 68, 251.

Livi, S. H. B., Martin, S. F., Wang, H., and Ai. G., 1989, Sol. Phys., 121, 197.

Low, B. C., & Smith, D. F., 1993, Astrophys. J., 410, 412L.

Low, B. C., 1994, Plasma Phys. 1, 1648.

Low, B. C., 1996, Sol. Phys.167, 217.

Low, B. C., 2001, J. Geophys. Res., 106, 25141.

Mackay, d. H., Gaizauskas, U., Richard, G. J., and Priest, E. R., 1997, Astrophys. J., 486,534.

Mackay, D. H., Longbottom, A. W., and Priest, E. R. 1999, Sol. Phys., 185, 87.

MacQueen, R. M., 1980, Philosophical Transcations Series A, vol.297, no.1433, p.605.

MacQueen, R. M., and Fisher, R. R., 1983, Sol. Phys., 89, 89.

Margenau, H., and Murphy, G. M., 1956, The Mathematics of Physics and Chemistry, D.VanNostrand, Princeton, NJ, 208.

Martin, S. F., livi, S. H. B., and Wang, J., 1985, Australian J. Phys. 38, 929.

Martin, S. F., 1986, Coronal and Prominence Plasma, NASA Conference Publ. 3224, 73.

Martin, S. F., 1989, Sol. Phys., 121, 215.

Martin, S. F. 1990, Dynamics of Quiescent prominences, 363, 1.

Martin, S. F., Bilimoria, R., and Tracadas, P. W. 1993, SPD.,24, 1907.

Martin, S. F., Bilimoria, R., and Tracadas, P. W. 1994, *Solar Surface Magnetism*, Kluwer Academic Publishers, Dordrecht, Holland, p. 303.

Martin, S. F. 1998, Sol. Phys., 182, 107.

Martens, P. C. H., and Kuin, N. P. M., 1989, Sol. Phys.122, 263.

McAllister, H. and Martin, S. F. 2000, Adv. Space Res., 26, 469.

Mikic, Z., Barnes, D. C., and Schnack, D. D., 1988, Astrophys. J., 328, 830.

Moffatt, H. K., and Ricca, R. L., 1992, Proc.R. Soc.Lond. A439, 411.

Moon, Y. J., et al. 2004, J. Korean Astron. Soc. 37, 41.

Moore, R. L., 1988, Astrophys. J., 324, 1132.

Moreton, G. F., 1961, S&T, 21, 145.

Mouradian, Z., Sour-Escaut, I., and Pojoga, S. 1995, Sol. Phys., 158, 269.

Mouschovias, T. C., and Poland, A. I., 1978, Sol. Phys., 220, 675.

Neupert, W. M., 1968, Astrophys. J., 153, L59.

Oliver, R., 1999 in Prominence Oscillations: Observations and Theory, 9th European Solar Physics Meeting, ESA SP-448, 425-434.

Oliver, R., and Ballester, J. L., 2002, Sol. Phys., 206, 45.

Pevtsov, A. A., Canfield, R. C., and Metcalf, T. R., 1994, Astrophys. J., 425L, 117.

Pevtsov, A. A., Canfield, R. C., and Zirin, H., 1996, Astrophys. J., 473, 533.

Pevtsov, A. A. and Canfield, R. C. 2001, J. Geophys. Res., 106, 25191.

Pikel'ner, S. B., 1971, Sol. Phys., 17, 44.

Poletto, G., and Kopp, R. A., 1986, in The Lower Atmosphere of Solar Flares, ed. D. F.Neidig(Sunspot: NSO/Sacramento Peak), 453.

Priest, E. R., and Forbes, T. G., 1986, J. Geophys. Res., 91, 1289.

Priest, E. R., Van Ballegooijen, A. A., and MacKay, D. H. 1996, Astrophys. J., 460, 530.

Qiu, J., Wang, H., Yruchyshyn, V. B., and Goode, P. R., 2000, SPD Meeting, 31, 0258.

Qiu, J., Lee, J., Gary, D. E., and Wang, H., 2002, Astrophys. J., 565, 1335.

Qiu, J., Wang, H., Cheng, C. Z., and Gary, D. E., 2004, Astrophys. J., 604, 900.

Qu, M., Shih, F., Jing, J., and Wang, H., 2003, Sol. Phys., 217, 157.

Qu, M., Shih, F., Jing, J., and Wang, H., 2004, Sol. Phys., 222, 137.

Ramsey, H., and Smith, S. F., 1966, Astron. J., 71, 197.

Ricca, R. L., and Berger, M., 1992, Phys. Today 12, 28.

Rompolt, B., 1975, Sol. Phys., 41, 329.

Rompolt, B., 1990, Hvar Obs. Bull. 14, 37.

Rust, D. H., 1994, Geophys. Res. Lett., 21,241.

Rust, D. H., and Kumar, A., 1994, Sol. Phys., 155, 69.

Rust, D. H. and Martin, S. F. 1994, ASP Conf. Ser., 68, 337.

Sakao, T., Kosugi, T., and Masuda, S., 1998, Prod-1998-Watanabe, 273.

Scherrer, P. H., and 11 co-authors, 1995, Sol. Phys., 162, 129.

Schmieder, B., Forbes, T. G., Malherbe, J. M., and Machado, M. E., 1987, Astrophys. J., 317, 956.

Schmieder, B. 1989, in Dynamics and structure of quiescent solar prominences; Proceedings of the workshop, Palma de Mallorca, Spain, Nov. 1987, Dordrecht, Kluwer Academic Publishers, p.15.

Seehafer, N., 1990, Sol. Phys., 125, 219.

Shibata, K., Tajima, T., and Steinolfson, R. S., et al., 1989, Astrophys. J., 345, 584.

Shanmugaraju, A., Moon, Y. J., Dryer, M., and Umapathy, S., 2003, Sol. Phys., 215, 185.

Sheeley, N. R., Walters, J. H., Wang, Y. M., et al., 1999, J. Geophys. Res., 104, 24739.

St. Cyr, O. C., Burkepile, J. Y., Hundhausen, A. J., and Lecinske, A. R., 1999, J. Geophys. Res., 104, 12493.

St. Cyr, O. C. et al., 2000, J. Geophys. Res., 105, 18169.

Steinegger, M., Denker, C., Goode, P. R., Marquette, W. H., Varsik, J., Wang, H., Otruba, W., Freislich, H., Hanslmeier, A., Luo, G., Chen, D., and Zhang, W. 2000, ESA SP-463, 617.

Terradas, J., Oliver, R., and Ballester, J. L. 2001, Astron. Astrophys., 378, 635.

Tsubaki 1988, PASJ, 40, 121T.

Vankatakrishnan, P., and Ravindra, B., 2003, GRL, vol.30, issue 23, SSC2-1.

an Tend, W., and Kuperus, M., 1978, Sol. Phys., 59, 115.

Vrsnak, B., 1990, Sol. Phys., 127, 129.

Vrsnak, B., and Rompolt, B., 1991, Sol. Phys., 136, 151

Vrsnak, B., 2004, A&A, 423, 717.

Vrsnak, B., 2004, A&A, 413, 753.

Wang, H., Ewell, M. W., Zirin, H., and Ai, G., 1994, Astrophys. J., 424, 436.

Wang, Y. M. and Sheeley, N. R., Jr. 1999, Astrophys. J., 510, 157.

Wang, H., Qiu, J., Jing, J., and Zhang, H., 2003,Astrophys. J., 593, 564.

Wang, H., Qiu, J., Jing, J., Spirock, T. J., and Yurchyshyn, V., 2004, Astrophys. J., 605, 931.

Wang, H., 2004, Astrophys. J., 601, L95.

Webb, D. F. and Hundhausen, A. J. 1987, Sol. Phys., 108, 383.

Webb, D. F., Cliver, E. W., Crooker, N. U., St. Cyr, O. C., and Thompson, B. J. 2000, J. Geophys. Res., 105, 7491.

Wilson, R. M. and Hildner, E. 1984, Sol. Phys., 91, 169.

Xu, Y., Cao, W., Liu, C., Yang, G., Qiu, J., Jing, J., Denker, C., and Wang, H., 2004, Astrophys. Lett., 607, L131.

Yang, G. and Wang, H. 2002, COSPAR Coll. Ser., 14, 113.

Yi, Z., and Engvold, O. 1991, Sol. Phys., 134, 275.

Yurchyshyn, V. B., Wang, H., Goode, P. R., and Deng, Y. 2000, Astrophys. J., 563, 381.

Zhang, H., and Bao, S., 1999, Astrophys. J., 519, 876.

Zhang, J., Dere, K. P., Howard, R. A., Kundu, M. R., and White, S. M., 2001, Astrophys. J., 559, 452.

Zhang, J., et al. 2004, Astrophys. J., 604, 420.

Zhang,M., and Golub, L., 2003, Astrophys. J., 595, 1251.

Zirker, J. B., Engvold, O., and Martin, S. F. 1998, Nature, 396, 440.

Zirker, J. B., 2001, *Solar Prominence Chirality*, in Murdin 2000.